Optical Properties of Lithiated Graphite In Relation to a Lithium Ion Battery Fiber Optic Sensor

by

AbdulRahman Ghannoum

A thesis

presented to the University of Waterloo

in fulfillment of the

thesis requirement for the degree of

Doctor of Philosophy

in

Chemical Engineering

(Nanotechnology)

Waterloo, Ontario, Canada, 2018

Examining Committee Membership

The following served on the Examining Committee for this thesis. The decision of the Examining Committee is by majority vote.

External Examiner	NAME Title	Dr. Igor Zhitomirsky Professor
Co-Supervisor	NAME Title	Dr. Aiping Yu Associate Professor
Co-Supervisor	NAME Title	Dr. Patricia Nieva Associate Professor
Internal Member	NAME Title	Dr. Mark Pritzker Professor
Internal Member	NAME Title	Dr. Michael Fowler Professor
Internal-external Member	NAME Title	Dr. Hamed Majedi Professor

Author's Declaration

This thesis consists of material all of which I authored or co-authored: see "Statement of Contributions" included in the thesis. This is a true copy of the thesis, including any required final revisions, as accepted by my examiners.

I understand that my thesis may be made electronically available to the public.

Statement of Contributions

This thesis is based on a combination of published work. Chapters are adapted from the following list of published work, with specific reference to the published work provided within the chapters.

A. Ghannoum, R. C. Norris, K. Iyer, L. Zdravkova, A. Yu, and P. Nieva, "Optical Characterization of Commercial Lithiated Graphite Battery Electrodes and in Situ Fiber Optic Evanescent Wave Spectroscopy," *ACS Applied Materials & Interfaces*, vol. 8, no. 29, pp. 18763–18769, Jul. 2016.

- A. Ghannoum wrote this manuscript with support from R. C. Norris on the colorimetry and reflectance study, and support from K. Iyer on the fiber evanescent wave spectroscopy section. A. Ghannoum processed experimental data and performed the analysis for the reflectance measurements and in-situ fiber optic evanescent wave spectroscopy. A. Ghannoum designed and carried out the experiment to determine the effect of salt concentration in the electrolyte on the optical fiber. A. Ghannoum designed the TOC and figures 1-6, 8 and 9. K. Iyer designed figure 7. R. C. Norris contributed to the development of Figure 4b and 5. L. Zdravkova and K. Iyer worked together in etching optical fibers and performing in-situ fiber evanescent wave spectroscopy. L. Zdravkova designed the swagelok cell to hold an optical fiber with assistance from Victor Chabot. K. Iyer proposed the initial use of an optical fiber to monitor the battery. Victor Chabot

extracted commercial graphite electrodes and assembled the swagelok cell. Mahdi performed reflectance measurements of the commercial graphite electrodes. P. Nieva supervised the project. A. Yu was a collaborator in the project.

Contributions:

- Determined that graphite particles govern the colour and reflectance of commercial graphite electrodes.
- Determined that a direct correlation exists between state of charge and reflectance of commercial graphite electrodes in near-infrared wavelengths (750 to 900 nm).
- Presented a method to monitor state of charge using an optical fiber within a swagelok cell.
- Determined that the largest change in the optical fiber transmittance with state of charge occurs in near-infrared wavelengths (750 to 900 nm)

A. Ghannoum, K. Iyer, P. Nieva, and A. Khajepour, "Fiber Optic Monitoring of Lithium-Ion Batteries," in *IEEE SENSORS 2016 Proceedings*, Orlando, FL, USA, 2016, pp. 868–870.

- A. Ghannoum wrote this manuscript with support from K. Iyer on the sensor system fabrication section. A. Ghannoum designed, fabricated, tested and analyzed results for the pouch cell with an optical fiber sensor. K. Iyer designed and assembled the optical sensor interrogator. A. Ghannoum designed all figures. P. Nieva supervised the project. A. Khajepour was a collaborator in the project.

Contributions:

- Designed and tested a commercially viable pouch cell with an optical fiber sensor.
- Presented direct correlation between graphite lithiation and optical sensor signal over multiple partial cycles.

- The use of a narrow-band LED concentrated at 850 nm as a light source for the optical fiber sensor and a silicon photodetector to measure the intensity of the transmitted light.

A. Ghannoum, P. Nieva, A. Yu, and A. Khajepour, "Development of Embedded Fiber-Optic Evanescent Wave Sensors for Optical Characterization of Graphite Anodes in Lithium-Ion Batteries," *ACS Appl. Mater. Interfaces*, vol. 9, no. 47, pp. 41284–41290, Nov. 2017.

- A. Ghannoum wrote this manuscript, designed, fabricated, tested and analyzed all pouch cell configurations. A. Ghannoum prepared battery materials and assembled all swagelok cells. A. Ghannoum analyzed all swagelok cell results and formed the correlation with the glycerol test. A. Ghannoum captured scanning electron micrographs of the etched fibers, graphite electrodes and dried graphite slurry. A. Ghannoum designed all figures. L. Zdravkova and K. Iyer both etched and characterized optical fibers. P. Nieva supervised the project. A. Khajepour and A. Yu were collaborators in the project.

Contributions:

- Presented a method to fabricate a lithium-ion pouch cell with an embedded optical fiber sensor using a graphite slurry to increase interaction and maximize sensitivity.
- Determined that an optical fiber sensor with 92 % transmittance loss in glycerol has the highest change in transmittance within a lithium-ion battery when charged from 0 to 100% SOC (i.e. highest sensitivity).
- Presented the superiority of buffered hydrofluoric acid in etching durable optical fiber sensors.

A. Ghannoum, J. R. Godin, and P. Nieva, “Modeling the Photonic interaction of Graphite with a Fiber Optic Sensor within a Lithium-ion Battery.” Unpublished manuscript

- A. Ghannoum wrote this manuscript. J.R. Godin only developed the fiber optic model used in this manuscript. P. Nieva supervised this project.

Contributions:

- A method to model the transmittance of an embedded optical fiber sensor.
- A graphite optical model to determine the refractive index and extinction coefficient of lithiated graphite.
- Designed a modified glycerol test to determine the cladding thickness of the etched optical fiber sensors with the use of J. R. Godin’s fiber optic sensor model.
- Slope analysis of the optical fiber sensor transmittance to determine the extent of lithiation or state of charge and detect significant capacity fade.
- Full battery charge signal amplitude analysis to determine the state of health of a battery.
- Designed a cycling protocol to observe the relaxation of lithiated graphite through the transmittance of the optical fiber sensor.
- Changing applied current to observe its effect on lithium-ion diffusion within a battery.
- Determined that the surface concentration of lithium-ions within the graphite electrode is the contributing factor to the optical change observed by the fiber optic sensor.

Abstract

As the demand for lithium-ion batteries (LIBs) has increased, research to increase their life and reliability has also continued. To further advance the ability of determining the material status of a battery during operation, this research work has stepped into a new direction that may pave the way for future developments in sensors that monitor battery material changes during operation.

Graphite is the most commonly used anode material and its phenomenal optical changes, which has fascinated many researchers, has inspired this research work and supported the development of a new type of electric battery cell sensor that utilizes an optical fiber to monitor the degree of lithiation within the battery cell. The ability to characterize the material within the battery during operation through optical data may allow the production of a smarter battery pack with the ability to perform in various environments and enable a higher level of understanding of its state-of-charge and state-of-health.

In this work, the implementation of a fiber optic evanescent wave sensor for LIBs is optimized and analyzed using a newly developed model. The reflectance of commercial graphite electrodes charged to 30, 35, 40, 45, 50, 60, 65, 70, 75 and 80 % SOC was measured to determine the role of graphite particles in governing the colour of commercial graphite electrodes in the visible and infrared range (500 – 900 nm). The reflectance of commercial graphite electrodes was found to be most sensitive to lithiation in wavelengths ranging from 750 to 900 nm, which is the near-infrared band. Using a modified Swagelok cell, in-situ fiber optic

evanescent wave spectroscopy (FEWS) was performed on a graphite electrode during electrochemical lithiation and found to closely follow the reflectance of commercial graphite electrodes. The FEWS study also demonstrated a direct correlation between transmittance through the optical fiber and the SOC of the LIB. The most sensitive wavelengths ranged from 750 to 900 nm. The transmittance through the fabricated optical fiber was found to be unaffected when in contact with LIB electrolytes (i.e., 3:7 (vol %) ethylene carbonate and dimethyl carbonate) at salt ($LiPF_6$) concentrations ranging from 0.25 to 1.50 M.

The fiber optic evanescent wave sensing system was optimized for ultimate commercialization by focusing on three aspects. The first is the etching of the fiber optic evanescent wave sensor (FOEWS). Experimental results demonstrated that a buffered hydrofluoric solution consisting of 40 wt % ammonium fluoride (NH_4F) solution and 49 wt % hydrofluoric acid solution in a ratio of 6:1 was superior to a solution of 49 wt % hydrofluoric acid in producing durable sensors. Maximum sensitivity of the FOEWS within a LIB was achieved when the etched sensor produced about 92 % transmittance loss in 100 % glycerol. The second aspect of optimization was aimed at reducing capacity fade and maximizing the contact between the sensor and the graphite electrode. This was achieved by shifting from a Swagelok test cell to a pouch cell designed to permit an optical fiber to pass through it while maintaining a hermetic seal and embedding the FOEWS within the graphite electrode. The final pouch cell configuration constituted a more commercially viable setup with reduced weight and increased capacity. The third major development was the use of an in-house narrow band optical sensor

interrogator, which replaced the spectrometer and reduced the cost of the sensing system significantly.

The theoretical basis for the developed LIB sensing system was investigated to allow for deeper understanding of its abilities. A linear optical model for graphite was developed. The model assumes a linear change from the normal dielectric constants of graphite to LiC_6 (fully lithiated graphite). This optical model was used to estimate the reflectance, refractive index and extinction coefficient of graphite as the concentration of intercalated lithium changes. The measured reflectance of graphite electrodes was compared with calculated values, based on the developed graphite optical model, and found to display similar trends. The optical model was then coupled with a lithium-ion battery transport model and a previously developed analytical optical model for the FOEWS to simulate the transmittance (signal) of the fiber optic sensor, with an estimated cladding thickness of 1.28 μm. Simulations produced trends comparable to experimental results and suggested that the lithiation rate around the FOEWS may occur at a higher rate than the rest of the graphite electrode. The effect of lithium diffusion at the surface of graphite particles on the FOEWS transmittance was observed by implementing two hours of rest at one hour intervals during the charging and discharging process of a LIB. The effect of lithium diffusion on the FOEWS was observed to be most significant during the initial discharge of a fully charged LIB, when the lithium concentration within the graphite particles is the greatest. The FOEWS was then tested using three distinct applied currents (i.e., C/5, C/8 and C/16) and found to deviate at the extremities (i.e., near 0 and 100 % SOC). The slope of the FOEWS transmittance over 33 cycles was observed to have three distinct peaks during a charge from 0 to

100 % SOC. Deviation from the “three peak” trend in the slope during a charge was found to be correlated to capacity fade. This demonstrated the ability of the sensor to predict significant capacity fade during a charge prior to observing the faded capacity during a full discharge. Finally, a method to estimate the cladding thickness of the FOEWS was presented, which utilizes the “comprehensive glycerol test” and FOEWS analytical model.

The presented work provides a direction for future work that would further promote the commercialization of the developed sensing system. Based on the deeper understanding of the factors contributing to the optical signal gained during this research, a battery state-of-charge and-health estimation algorithm can be developed and tested for its accuracy. Comparing the cost of this sensing system to conventional methods would demonstrate its competitiveness and support its use in various applications.

Acknowledgements

All praise is due to the Lord of the universe for the strength and blessing that he has given me in completing this thesis. I would like to thank Dr. Patricia Nieva for her fruitful guidance and continued support and Dr. Aiping Yu for providing the environment needed to complete the many challenging experiments within this thesis. Additionally, I would like to thank the thesis examining committee Dr. Mark Pritzker, Dr. Michael Fowler, Dr. Hamed Majedi and Dr. Igor Zhitomirsky for their contributions and support through this valuable process.

I would like to thank the University of Waterloo for attracting the many outstanding colleagues that provided me with a healthy working environment within the SimsLab, Applied Carbon Nanotechnology Laboratory, Applied Nanomaterials & Clean Energy Laboratory and Giga-to-Nanoelectronics Centre, which included Dr. Fathy Hassan, Dr. Hay Woong Park, Victor Chabot, Jason Wu, Dr. Dong Un Lee, Kun Feng, Jing Fu, Dr. Jingde Li, Matthew Li, Ja-Yeon Choi, Victor Chabot, Gregory Lui, Dr. Zhiyu Mao, Krishna Iyer, Dr. Jeremy R. Godin, Dr. Ali Najafi Sohi, Liliana Zdravkova, Dr. Ryan C. Norris, Mahdi, Eric Brace, and many others. I would also like to thank my friends for their support and wish them all a bright future.

Finally, I would like to thank my parents Ahmad & Iman Ghannoum for their support and love that they have given me since my birth. I would also like to thank my uncle Dr. Mahmoud A. Ghannoum for his valuable advice and love. Lastly, I would like to thank my love, Marwa Messaykeh for the beautiful days that we had since we met.

This work was financially supported by the “Green Intelligent Transportation Systems (GITS)” – Ontario Research Fund, Canada, the “Next Generation Electric Vehicles: Development of Key Technologies and Full Vehicle Testing” – Natural Sciences and Engineering Research Council of Canada (NSERC) – Automotive Partnership Canada, and General Motors.

Table of Contents

List of Figures

List of Tables

List of Abbreviations

ADC	–	Analog to Digital Convertor
BHF	–	Buffered Hydrofluoric Acid
DEC	–	Diethyl Carbonate
DMC	–	Dimethyl Carbonate
EC	–	Ethylene Carbonate
FCE	–	First Cycle Efficiency
FEWS	–	Fiber Optic Evanescent Wave Spectroscopy
FOEWS	–	Fiber Optic Evanescent Wave Sensor
HF	–	Hydrofluoric Acid
Li	–	Lithium
Li^+	–	Lithium Ion
LIB	–	Lithium Ion Battery
LiC_{12}	–	Stage 2 Lithiated Graphite
LiC_{18}	–	Stage 3 Lithiated Graphite
LiC_6	–	Stage 1 Lithiated Graphite or Fully Lithiated Graphite
$LiClO_4$	–	Lithium Perchlorate

$LiCoO_2$	–	Lithium Cobalt Oxide
$LiFePO_4$	–	Lithium Iron Phosphate
Li-GIC	–	Lithium Graphite Intercalation Compounds
$LiMn_2O_4$	–	Lithium Manganese Oxide
NH_4F	–	Ammonium Fluoride
OCV	–	Open Circuit Voltage
OSI	–	Optical Sensor Interrogator
PC	–	Propylene Carbonate
SEI	–	Solid Electrolyte Interphase
SEM	–	Scanning Electron Microscopy
SOC	–	State of Charge
SOH	–	State of Health

List of Symbols

$c_{s,i}$	Lithium concentration in electrode i	[mol m^{-3}]
$c_{s,0,i}$	Initial lithium concentration in electrode i	[mol m^{-3}]
$c_{s,max,i}$	Maximum Lithium concentration in electrode i	[mol m^{-3}]
D	Diffusion coefficient of the electrolyte	[m^2 s^{-1}]
$D_{s,i}$	Solid phase diffusion coefficient in electrode i	[m^2 s^{-1}]
e	Charge of an electron ($1.6022 \times 10^{-19} C$)	[C]
$f_{\pm}$	Mean molar salt activity coefficient	
F	Faraday's constant ($96{,}487\ C\ mol^{-1}$)	[C mol^{-1}]
i_0	exchange current density	[A m^{-2}]
i_f	Faradaic current density	[A m^{-2}]
I_{app}	Applied current	[A]
k	Extinction coefficient	
$k_{a,i}$	Anodic reaction rate constant	[m s^{-1}]
$k_{c,i}$	Cathodic reaction rate constant	[m s^{-1}]
L_i	Thickness of component i	[m]
m^*	Effective mass of electrons	[kg]
n	Refractive index	
n_e	Number density of electrons	[m^{-3}]
r	Radial distance in a spherical electrode particle	[m]
r_i	Particle radius in electrode i	[m]
R	Universal gas constant ($8.3145\ J\ mol^{-1}\ K^{-1}$)	[J mol^{-1} K^{-1}]
R_ω	Reflectivity	
SOC	Stage of charge	
t	Time	[s]
t_+	Cationic transport number	
T	Temperature	[K]
α_i	Charge transfer coefficient of electrode i	
ϵ	Volume fraction of electrolyte in the separator region	
$\epsilon_{s,i}$	Volume fraction of electrode i	
$\epsilon_{l,i}$	Volume fraction of electrolyte in electrode region i	
ε	Dielectric constant	
ε_0	Electric constant/permittivity in free space ($8.8542 \times 10^{-12} F\ m^{-2}$)	[F m^{-2}]
ε_1	Real part of the dielectric constant	
ε_2	Imaginary part of the dielectric constant	
ε^b	Bound electrons contribution to the dielectric constant	
ε^f	Free electrons contribution to the dielectric constant	

$\eta_{act,i}$	Activation overpotential	[V]
σ	Conductivity of the electrolyte	[S m^{-1}]
σ_i	Conductivity of electrode i	[S m^{-1}]
ϕ	Potential in the electrolyte	[V]
ϕ_i	Electrical potential of electrode i	[V]
$\Delta\phi_{eq}$	Equilibrium potentials (SOC)	[V]
ω	Angular frequency of the photons	[rad s^{-1}]
ω_p	Plasma frequency	[rad s^{-1}]

Subscripts

c	Lithium Iron Phosphate, cathode
g	Graphite, anode
i	Refers to electrode i; g or c
l	Electrolyte, liquid
Li	Lithium
s	Solid phase
sep	separator

1. Introduction

Parts of this chapter are reprinted in adapted form with permission from [1]

A. Ghannoum *et al.*, "Optical Characterization of Commercial Lithiated Graphite Battery Electrodes and in Situ Fiber Optic Evanescent Wave Spectroscopy," *ACS Applied Materials & Interfaces*, vol. 8, no. 29, pp. 18763–18769, Jul. 2016. Copyright (2016) American Chemical Society.

Energy diversification and the rise in zero-emission vehicles have promoted research in energy storage systems. Zero-emission vehicles include battery-powered electric vehicles and hydrogen fuel cell vehicles. The current automotive industry has focused on batteries as a source of alternative energy due to the challenges that still remain for fuel cells, which include improvements to its reliability, reducing its cost and development of the required hydrogen infrastructure [2]. Lithium-ion batteries (LIBs) have been targeted for use in electric and hybrid vehicles due to their high energy density [3]. A wide selection of electrode chemistries can be used in LIBs, but it is essential that the cost, durability, environmental effects, safety and specific energy density are taken into account when designing a battery for a specific application. LIBs consist of two electrodes, graphite is the most common negative electrode (anode) material used in LIBs as it has relatively high capacity (372 mAh g^{-1}), highly reversible lithium ion intercalation (insertion), good electrical conductivity, and can be simply and inexpensively produced [4]. Figure 1 demonstrates the market demand of graphite in comparison to other anode materials over the past several years.

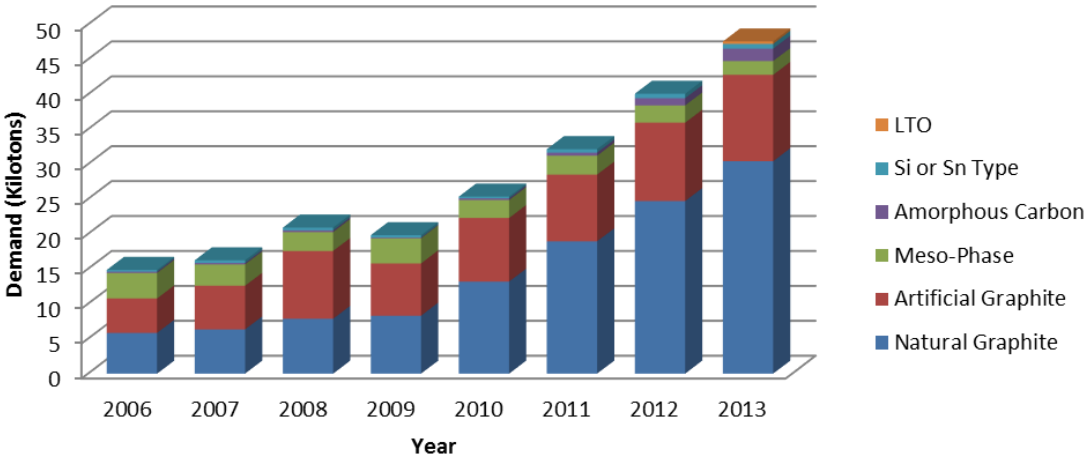

Figure 1: Lithium-ion battery anode material market; plotted using data extracted from ref. [5].

Electric vehicles are powered by a large number of cells connected in series, managed by a control system referred to as a battery management system (BMS) that manipulates the charging and discharging processes. The BMS is required to estimate the state of charge (SOC), state-of-health (SOH) and identify cell failures to successfully and safely control a large number of cells. To perform all these estimates , a system may utilize sensors to measure temperature, voltage, current, running time and combustible gas concentration [6]. Then through the use of algorithms a BMS estimates the status of the battery cells based on a point of reference or battery model, which differs with chemistry, battery shape and battery size [6]–[8]. The accuracy of the estimation algorithms is affected by the complexity and the accuracy of the sensors, which both significantly affect the cost of the BMS. This significant cost factor has spawned research on

acoustic [9], [10], strain[11]–[14], and optical [1], [15]–[18] based characterization methods that aim to reduce the cost, but still accurately estimate SOC and SOH for LIBs.

1.1 Lithium-Ion Batteries

Lithium-ion batteries consist of positive and negative electrode materials capable of storing lithium, respectively, known as cathode and anode. The two electrodes are separated by insulating material to avoid internal electron transfer between the two electrodes. Lithium ions (Li^+) are transported across an electrolyte between the two electrodes as the battery is charged and discharged. Current LIBs utilize cathode materials composed of either a metal oxide (e.g., $LiCoO_2$) or metal phosphate (e.g., $LiFePO_4$). Figure 2 illustrates the three identified cathode material structures, layered (e.g., $LiCoO_2$), spinel (e.g., $LiMn_2O_4$) and olivine (e.g., $LiFePO_4$).

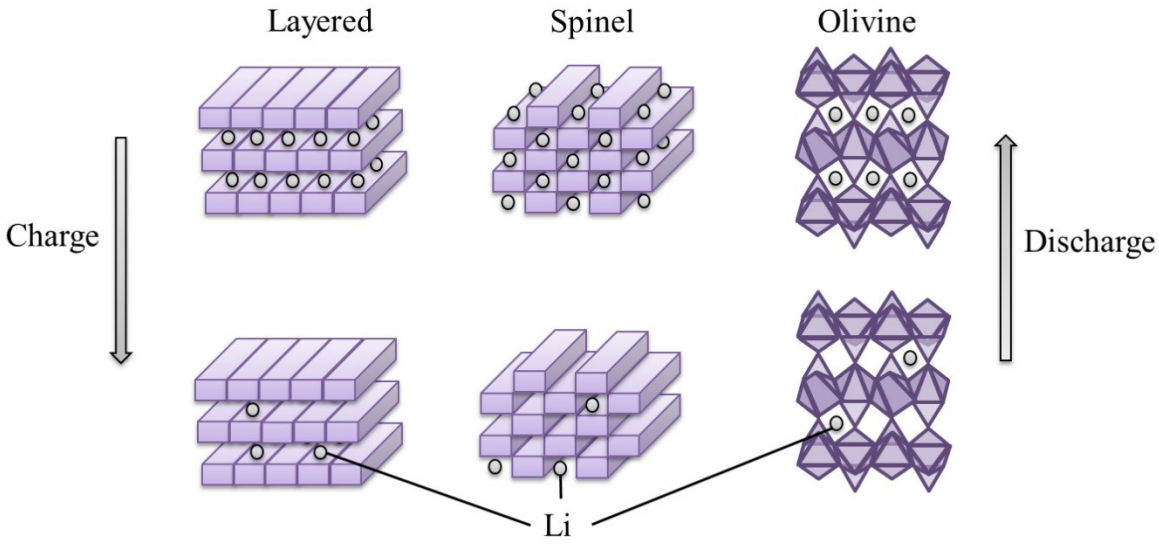

Figure 2: Lithium-ion battery cathode material structures.

When the battery is fully charged, the lithium content in the cathode is at its minimum. During discharge, lithium undergoes oxidation at the anode forming Li-ions that are transported through the electrolyte to the cathode where a reduction reaction inserts Li-ions into the cathode. Figure 3 illustrates the process of lithium ion insertion into graphite; this process is referred to as lithiation, while delithiation refers to the removal of lithium.

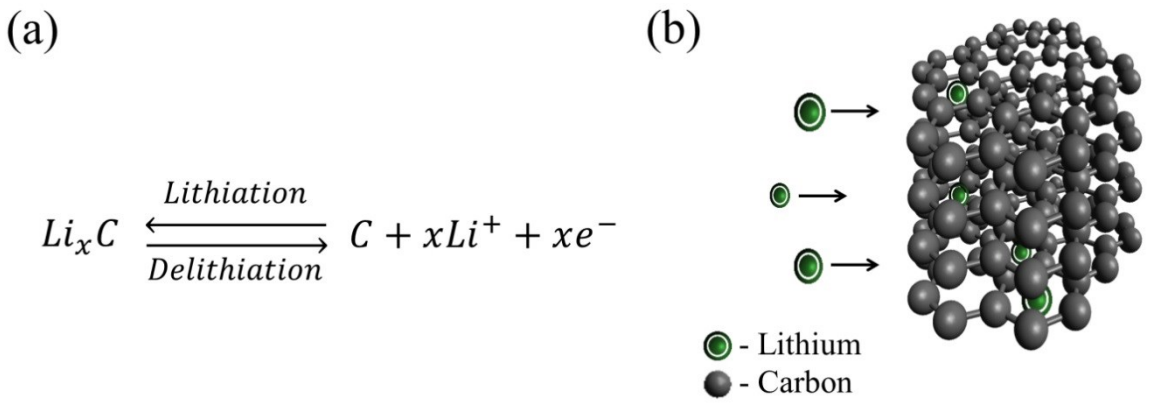

Figure 3: (a) Graphite's lithiation/delithiation reaction (b) Schematic of the lithiation process.

LIBs are advantageous due to their ability to undergo many charging/discharging cycles, but over time capacity loss limits its life. LIB capacity degradation occurs due to several factors. One major factor controlled by a BMS is voltage [19]. When the voltage of a LIB falls below 2V vs. Li/Li^+ (over discharge), reduction of the electrolyte occurs at the anode, consuming electrolyte and Li-ions, as a result reducing its overall capacity [20]. Conversely when a LIB is over-charged, the increase in the voltage causes oxidation of the electrolyte at the cathode, which also

reduces the battery's capacity [21]. Hence, it is essential to control the charging and discharging process of a LIB to avoid capacity loss through irreversible reactions.

1.2 Graphite as a Lithium Ion Battery Anode

Graphite is a layered carbon material that can be classified by the fraction of its structurally disordered content. The basic building block of graphite is graphene, a planar sheet of carbon atoms that stacks to form a layered structure [19]. A variation between the intraplanar and interplanar bonding forces in graphite allows for the intercalation of lithium into its layered structure, forming lithium graphite intercalation compounds (Li-GIC) [22]. The stacking configuration has a significant effect on the maximum amount of lithium that can be inserted (capacity), as the fraction of layers with turbostratic misalignment increases, the maximum capacity decreases [23]. The stacking of graphene in relation to intercalated lithium layers is described by a stage number based on a periodic sequence, where the stage number represents the number of graphite layers between the intercalated lithium layers (Figure 4). Through analysis of the potential of graphite during electrochemical lithiation and graphite's colour changes, stages 1, 2 and 3 (diluted stage 2 [24]) have been identified to be golden yellow, red and dark blue, respectively [25]. Stage 3 is identified as diluted stage 2, since x-ray diffraction measurements have shown that a phase change does not occur and the reaction is assumed to cause in-plane lithium ordering between LiC_6 and LiC_9 [22].

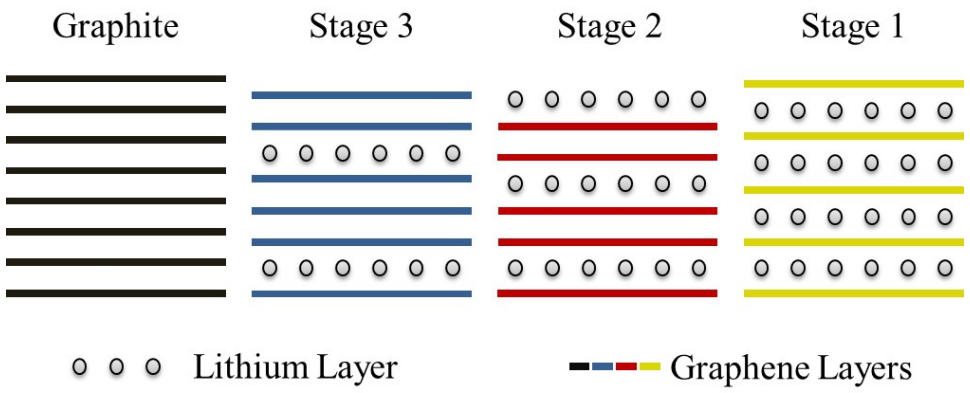

Figure 4: Schematic diagram of stages 1, 2 and 3 (diluted stage 2 [24]) lithiated graphite based on the Rudorff model [26] with their recognized visible colours of golden yellow, red and dark blue, respectively.

As graphite transitions from one stage to another, its potential vs. Li/Li^+ changes. In regions where more than one stage exists, a plateau in the voltage is observed [23]. This observation has been reproduced through the fabrication of a half-cell consisting of a graphite cathode and a lithium metal anode (see Figure 5). The transition for lithiated graphite from stage 1 (LiC_6) to stage 2 (LiC_{12}) has the largest voltage plateau, which makes it easy to identify in the voltage profile (i.e. between 150 to 300 mAh/g capacity in Figure 5). The reactions and stage transitions within Figure 5 are further described in Table 1.

As the voltage of lithiated graphite vs. Li/Li^+ decreases, its chemical reactivity increases. Reactions involving the electrolyte arise, consuming Li-ions and producing a solid interface between the graphite surface and the electrolyte, known as the solid electrolyte interface (SEI) [21].

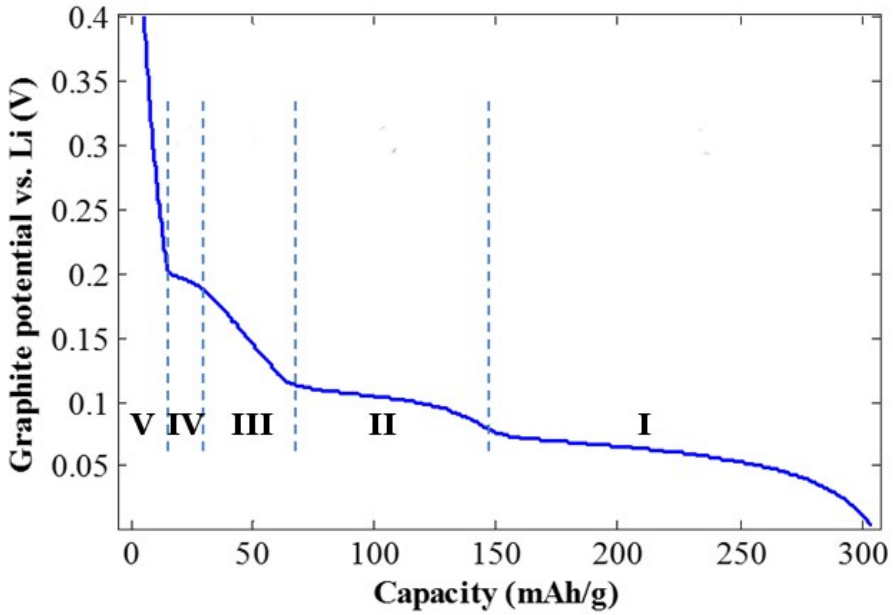

Figure 5: MTI Graphite voltage profile during discharge in a coin cell, with the regions of phase transitions labeled I, II, III, IV and V at the observed plateaus described in Table 1.

Table 1: Regions in graphite's potential vs. lithium during lithiation (Figure 5) and the corresponding reactions and stage numbers [22], [27]. 2D denotes dilute stage 2.

Regions in Figure 5	Graphite's lithiation stage transition	Reaction
I	Stage 2 ↔ Stage 1	$LiC_{12}+Li \leftrightarrow 2LiC_6$
II	Stage 2D ↔ Stage 2	$2LiC_{18}+Li \leftrightarrow 3LiC_{12}$
III	Stage 3 ↔ Stage 2D Stage 4 ↔ Stage 3	$2LiC_{27}+Li \leftrightarrow 3LiC_{18}$ $3LiC_{36}+Li \leftrightarrow 4LiC_{27}$
IV	Stage 8 ↔ Stage 4	$LiC_{72}+Li \leftrightarrow 2LiC_{36}$
V	Graphite ↔ Stage 8	$12C_6+Li \leftrightarrow LiC_{72}$

The reduction of the electrolyte and consumption of Li-ions to produce the SEI results in capacity loss since the reactions are irreversible. The formation of a stable SEI layer though is essential since it ensures that no further irreversible reactions occur. The ideal SEI would electrically insulate the electrolyte, preventing its further decomposition, while allowing uniform Li-ion migration into and out of the graphene layers [21]. For the long term stability of the SEI, its resistance to dissolution into the electrolyte is crucial and structural flexibility is integral to sustain its position on the graphite particles as it undergoes stress [28] during lithiation/delithiation [21].

Stress is induced by lithiation, which causes the spacing between the graphene layers to increase by about 0.351 Å (10.5 %), when comparing graphite to LiC_6 [29]. The graphite surface area is thought to have a direct relationship with the amount of SEI, since larger surface areas caused higher initial irreversible capacity loss [30]. Many developments have been made to optimize the SEI formation through the use of electrolyte blends and additives, which will be discussed in the coming sections. Understanding the intercalation process and surface modification is essential in studying its optical properties and how it would affect the response of a fiber optic sensor.

1.2.1 Graphite Solid Electrolyte Interface (SEI)

Lithium insertion into graphite decreases its potential to values near 0 V vs. Li/Li^+, requiring a change in the system to allow for the stabilization of the known electrolytes and avoid their continuous reduction [19]. Exposure of electrolyte to lithiated graphite initiates its reduction at the surface of graphite forming a layer, which is made up of lithium and decomposed electrolyte.

The formed layer prevents further reduction of the electrolyte and consumption of lithium ions if it insulates the electrolyte from charge transfer electrons. However, for the functionality of the system, the formed layer should still allow lithium ion transfer to allow for Li-ion insertion/de-insertion into graphite. This layer has been given the name solid electrolyte interface (SEI). The amount of SEI that forms is mainly affected by the surface area of the graphite as this increases the observed irreversible capacity losses [11]. Since the SEI is made up of decomposed electrolyte, many studies have been conducted on various electrolytes to understand the formation mechanism to advance the performance of LIB. Early studies on liquid electrolytes were initiated with propylene carbonate (PC), a polar organic molecule, that has a high dielectric constant and is known for its ability to allow lithium electro-deposition using lithium perchlorate ($LiClO_4$) as a salt [31]. When PC was used as an electrolyte with graphite, it decomposed reductively at a potential of 0.80 V vs. Li/Li^+, causing graphite to disintegrate (exfoliate) and prohibit lithium ion intercalation [21]. It has been shown that PC does not form a stable SEI and instead co-intercalates into graphite and forms decomposition products that cause its exfoliation [33]. Ethylene carbonate (EC), which is essentially PC without the methyl group, has a higher dielectric constant and melting point (~36^{o}C) [21]. Although EC may increase the ionic conductivity of the electrolyte if used as a co-solvent, its main contribution is the formation of a stable SEI on graphite that allows for the reversible intercalation/de-intercalation of lithium [21]. The differences in the SEI produced in the presence of EC and PC has been attributed to the effect of the methyl group from PC, which prevents good adhesion and cohesion of the decomposed products onto graphite. The methyl group favors gas evolution over SEI formation

[21]. Mixing EC with other solvents such as dimethyl carbonate (DMC) and diethyl carbonate (DEC) reduces its melting point and allows for its use as a liquid electrolyte [33].

Through tuning of the mixing ratios it is possible to optimize the stability of the solvated lithium ions in the electrolyte to maximize cation/anion diffusion and minimize their interaction to achieve better mobility [34]. Minor changes in the components of the electrolyte can significantly affect the formation of the SEI layer as well as the kinetics of the system, as diffusion of the cations and anions vary. Since performance of certain systems exceeds that of others, then understanding the effects of the various components of such systems is critical. Studies have shown that the thickness of the SEI layer can vary between ~0.2 to 10 nm [35][36][37] and has been reported to vary with the stage of lithiation [38]. The optical absorbance of lithiated graphite in the infrared region (5–20 μm) is also influenced by the chemical components of the SEI layer [20].

In the design of an optical sensor it would be favourable to exclude these wavelengths to avoid the effects of a dynamic SEI. The next section will introduce the optical properties of graphite, which will be seen to significantly change during the cycling process of a LIB.

1.3 Optical Properties of Lithiated Graphite

Graphite intercalation compounds exhibit metallic reflectivity spectra which have been analyzed on the basis of the classical Drude model for unbound electrons [39]. The Drude model is derived by equating the restoring force in the Lorentz model to zero; the Lorentz model is the classical model for insulators, which considers electrons to be a small mass bound by a spring to

a larger mass representing the atomic nucleus [40]. Pristine graphite has a relatively low free carrier concentration, i.e., $\sim 2 \times 10^{-4}$ carrier atom^{-1} ($\sim 2 \times 10^{19}$ cm^{-3}) at room temperature [41]. As lithium insertion into graphite occurs via a charge transfer reaction, graphite fully ionizes due to the transfer/delocalization of the Li 2s electron into the graphite π-band [39][42]. Lithiation increases the carrier density in graphite by a factor of ~800 when fully lithiated (LiC_6) altering its electrical, thermal, magnetic and optical properties [41].

Electron transitions can occur in two ways (interband/intraband) within graphite. These transitions and the energy required to initiate them contribute to the optical properties of graphite. Interband electron transitions dominate in the infrared and visible regions of pristine graphite's spectrum [41], which are transitions of electrons from one band to another [40]. As lithium intercalates into graphite and the carrier density increases, interband transitions decrease while intraband transitions increase at low frequencies [41]; intraband transitions caused by optical excitation of electrons from below the Fermi energy to above the Fermi energy within the same band are characteristic of metals and semi-conductors [40]. Intraband transitions of a material can be described by the Drude model for unbound electrons [40]. The reflectance of LiC_6 when compared with graphite at low frequencies (low energy) demonstrates how the increase in carrier density affects the optical properties of graphite.

The plasma frequency (ω_p) of LiC_6 can also be used to explain the observed increase in reflectance, which is associated with free carrier plasma oscillations [43]. If the frequency of the photon is below that of the ω_p, then reflectance is high, when the photon frequency exceeds the ω_p, reflectance decreases [43]. As graphite anodes transform from pristine graphite to LiC_6, the

ω_p shifts and the specific frequency at which reflectance decreases changes and causes an observable colour change in graphite [41],[25].

Earlier reflectance studies on lithiated graphite synthesized LiC_6 and LiC_{12} through vapour phase reactions, which produced single-crystal flakes that were used for characterization [39]. A clear shift in the normal incident reflectivity of LiC_{12} to LiC_6 was observed, whereby the ω_p increased from about 1.75 to 2.75 eV, demonstrating the effect of lithiation on the electron transitions [39].

It is critical to note that graphite is in powder form within a LIB and is not composed of single-crystal flakes of graphite. Using an integrating sphere the diffuse reflectance of an amorphous carbon electrode (petroleum coke) was studied during its delithiation process in a prototype half-cell with a pure lithium anode [44]. The diffuse spectra of petroleum coke ranged from 200 to 800 nm (6.20 to 1.55 eV) [44]. At about 230 nm (5.4 eV) a peak is observed, which seems to not be affected by the lithiation process. This peak has been attributed to the π–π^* interband transition [44], which is also observed in pristine graphite [43]. LiC_6 also exhibits a similar peak but is slightly shifted to a lower frequency. The petroleum coke energy band structure seems to not be significantly affected by the lithiation process, which may be related to the microscopic orderliness of petroleum coke in comparison to graphite [44]. The diffuse reflectance signal at higher wavelengths (> 350 nm) was attributed to intraband transitions of free carriers. The intraband transitions increased as the amount of lithium in petroleum coke increased [44]. These studies demonstrate that the optical properties of carbon electrodes vary as

the lithium content changes, but it is also important to understand how the optical properties change as electrodes age.

A colorimetric study on a graphite electrode lithiated using a pure lithium anode demonstrated that the colour change was stable over 20 cycles [25]. It is important to note that this study was done on a small custom windowed cell with only 20 cycles [25], which does not represent the life of a graphite electrode within a commercial cell. Images of an aged graphite electrode extracted from a high power commercial cell, which was cycled 1400 cycles and had a 60 % reduction in capacity, showed a significant non-uniformity in the colour distribution, which was translated to lithium content [25]. This demonstrates that if the intensity of the reflectance can be monitored then the aging of a cell could be observed as the intensity in reflectance varies over time.

A simple empirical correlation can be made using specific wavelengths and the extent of lithiation of a graphite electrode based on the observed phenomena but it would be of higher fundamental value to model the variation in the carrier density in relation to reflectance within a lithium ion battery. To model the change in carrier density a lithium ion transport model is required. In a lithium ion battery, several properties affect lithium ion transport, which affect the lithium content in graphite; the next section will cover one of the methods that can be employed to model lithium transport within a battery system.

1.4 Modeling of lithium ion transport

Lithium ion batteries consist of two insertion electrodes that allow the shuttling of lithium ions. The degree of lithium insertion controls the cell potential. When an anode such as graphite

is fully lithiated within a battery cell, then the battery is considered fully charged. If a circuit connects the anode to the cathode in a fully charged battery then the battery would discharge. The discharge of a battery is the process where electrons would spontaneously flow from the anode to the cathode through the outer circuit while lithium ions de-intercalate from the anode and diffuse/migrate into the electrolyte while lithium ions intercalate into the cathode. During the charging of the battery, external work needs to be applied to reverse the discharging process, since the system deviates from the thermodynamically favoured state [45]. The development of mathematical models derived from the thermodynamics that revolve around the charging/discharging process [45][46][47][48][49] has been of interest to design and optimize lithium-ion batteries [50][51]. This resulted in the formation of general full cell models that required specific physical properties and system parameters to simulate particular materials [52]. This section outlines the governing equations and boundary conditions [45], [51], [53], [54] used in modeling the transport of lithium ions between a lithium iron phosphate ($LiFePO_4$) cathode and a graphite anode as seen in Figure 6 within a multi-physics software (COMSOL Inc.).

The equations governing the transport of Li in the electrode region are divided into two, the solid phase ($c_{s,i}$) and electrolyte phase (c). In the solid phase Li diffusion within the assumed spherical electrode particles is based on Fick's law, i.e.,

$$\frac{\partial c_{s,i}}{\partial t} = D_{s,i}\frac{1}{r^2}\frac{\partial}{\partial r}\left(r^2\frac{\partial c_{s,i}}{\partial r}\right) \tag{1}$$

At the center of the electrode particles, a boundary condition of no flux is set:

$$D_{s,i}\frac{\partial c_{s,i}}{\partial r} = 0 \text{ at } r = 0 \tag{2}$$

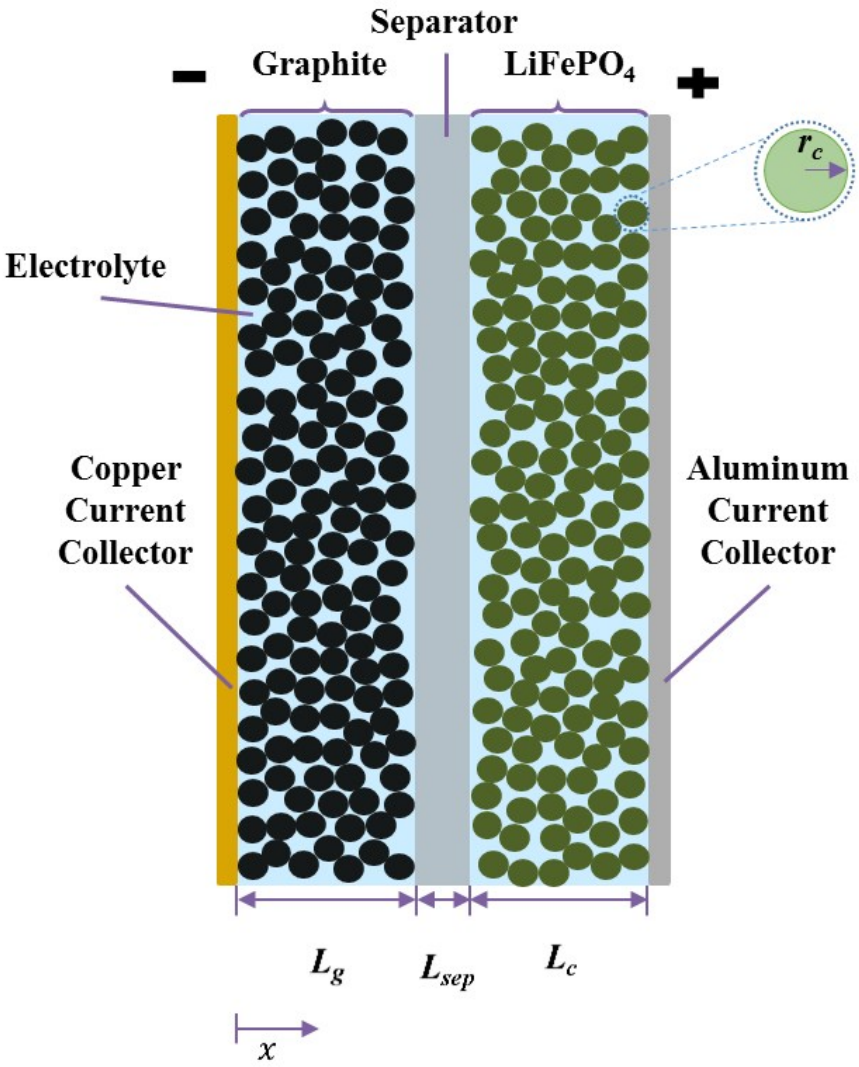

Figure 6: Schematic of a lithium ion battery with a graphite anode and a $LiFePO_4$ cathode, outlining the components of a transport model.

At the surface of the electrode particles, the flux of Li is based on the Faradaic current (Eq.(3)), which is calculated based on the Butler-Volmer equation (Eq. (4)),

$$-D_{s,i}\frac{\partial c_{s,i}}{\partial r} = \frac{i_f}{F} \text{ at } r = r_i \tag{3}$$

$$i_f = i_{0,i}\left(exp\left(\frac{\alpha_i F}{RT}\eta_{act,i}\right) - exp\left(-\frac{(1-\alpha_i)F}{RT}\eta_{act,i}\right)\right) \tag{4}$$

where the exchange current density ($i_{0,i}$) is a function of the anodic/cathodic reaction rate constants ($k_{a,i}, k_{c,i}$) and Li concentration in both the electrolyte (c) and solid phase ($c_{s,i}$),

$$i_{0,i} = F\left(k_{a,i}\right)^{(1-\alpha_i)}\left(k_{c,i}\right)^{\alpha_i}(c)^{\alpha_i}\left(c_{s,max,i} - c_{s,i}\right)^{\alpha_i}\left(c_{s,i}\right)^{(1-\alpha_i)} \tag{5}$$

The current in the solid phase is based on ohms law,

$$i_{s,i} = -\sigma_i \nabla \phi_i \tag{6}$$

The applied current density (I_{app}) controls the charge flux between cathode/current collector, while electrode/separator boundaries insulate against electronic current,

$$-\sigma_g \frac{\partial \phi_g}{\partial x} = I_{app} \text{ at } x = 0 \quad (7)$$

$$\sigma_g \frac{\partial \phi_g}{\partial x} = 0 \text{ at } x = L_g \quad (8)$$

$$\sigma_c \frac{\partial \phi_c}{\partial x} = 0 \text{ at } x = L_g + L_s \quad (9)$$

$$\sigma_c \frac{\partial \phi_c}{\partial x} = I_{app} \text{ at } x = L_g + L_s + L_c \quad (10)$$

Graphite's current collector is set as the electric ground, $\phi_g(x = 0) = 0$. In the electrolyte phase around the solid electrodes the Li ion concentration is balanced by the following equation,

$$\epsilon_{l,i} \frac{\partial c}{\partial t} = \nabla \cdot (D \nabla c) - \frac{i \cdot \nabla t_+}{F} + \frac{\nabla \cdot i}{F}(1 - t_+) \quad (11)$$

where,

$$i = -\sigma \nabla \phi + \frac{2\sigma RT}{F}\left(1 + \frac{\partial \ln f_\pm}{\partial \ln c}\right)(1 - t_+)\nabla \ln c \quad (12)$$

and $f_\pm$ is the mean molar activity coefficient. At the outer boundaries no charge or Li flux exists in the electrolyte,

$$\sigma \frac{\partial \phi}{\partial x} = 0 \text{ at } x = 0 \text{ and } x = L_g + L_s + L_c \quad (13)$$

$$D \frac{\partial c}{\partial x} = 0 \text{ at } x = 0 \text{ and } x = L_g + L_s + L_c \quad (14)$$

The Li ion concentration within the separator region (i.e. between $x = L_g$ and $x = L_g + L_s$) does not include pore wall flux and the electrolyte is assumed to have a volume fraction of one, hence in the separator region Eq.(11) becomes,

$$\frac{\partial c}{\partial t} = \nabla \cdot (D \nabla c) - \frac{i \cdot \nabla t_+}{F} \tag{15}$$

These equations are solved simultaneously to obtain $c_{s,\mathrm{g}}$ as function of time, which can be divided by $c_{s,\mathrm{max,g}}$ to obtain the state of charge of a graphite particle as a function time.

2. Thesis Objectives and Approach

The objectives of this thesis are to optimize the implementation of fiber optic evanescent wave sensors (FOEWS) inside LIBs and develop a coupled model to simulate and enhance our understanding of the sensor output as the optical properties of graphite change within a LIB. This allows for deeper analysis of the sensor signal (transmittance) to allow further optimization and support its implementation in commercial LIBs for state-of-charge and state-of-health estimation.

The lithiation of a graphite anode is a dynamic process that depends on several factors, which include its capacity, electrode thickness and applied electrical current. This necessitates the use of a transport model to simulate the concentration changes at the surface of the graphite particles and their effect on the FOEWS. As for the optical properties of a graphite anode, the non-pristine surface of the anode makes it challenging to experimentally determine its refractive index and extinction coefficient, and hence the development a linear optical model based on the known dielectric constants of graphite and fully lithiated graphite. This approach is the basis for the developed coupled model to investigate the sensor signal in relation to the optical changes of graphite within a LIB.

The breakdown of the overall approach is summarized in Figure 7 where each step is designated with a number, which will be referred to in the following list of specific objectives.

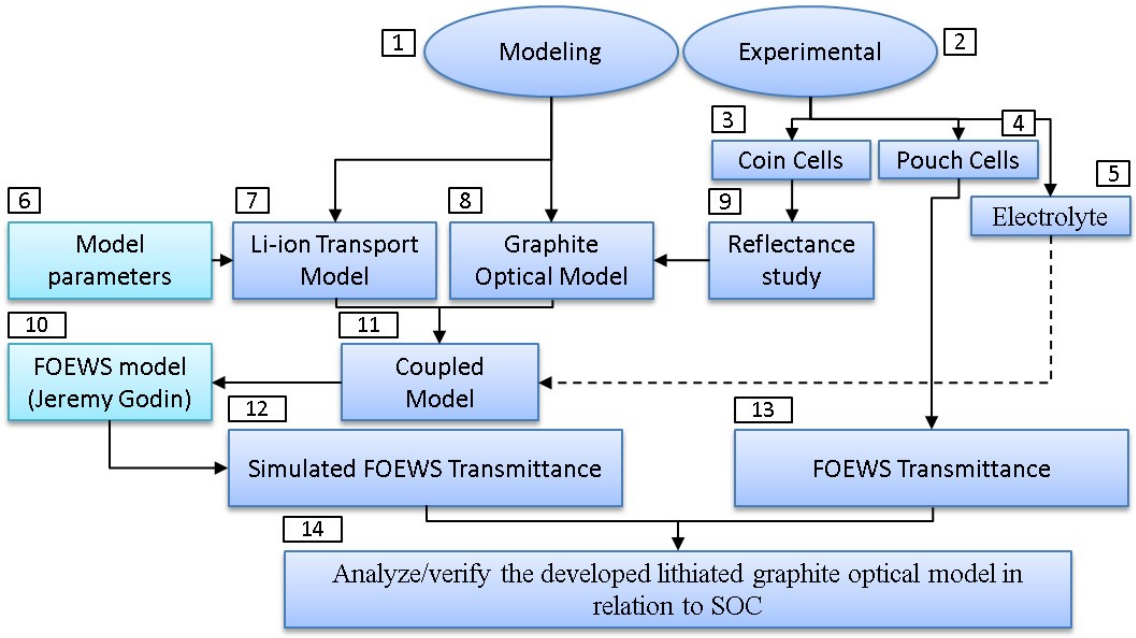

Figure 7: Schematic outlining the modeling and experimental work completed to compare simulated FOEWS transmittance to actual transmittance

The thesis objectives are divided into two sections, modeling {1} and experimental {2}. The specific objectives include:

i. optimization of the fabrication and characterization process for FOEWS to enhance sensitivity and durability of the sensor {4}.

ii. design of a process to embed a FOEWS in a graphite anode within a pouch cell {4} to study the sensor signal {13,14}.

iii. investigation of the potential effects of the electrolyte on the FOEWS {5}.

iv. examination of the durability of the sensor within a LIB {4}.

v. development of an optical model for graphite {8} and verify it through a reflectance study on commercial graphite anodes {3,9}. The optical model coupled with a transport

model {6,7} and an analytical model {10} of the FOEWS yields a simulated sensor signal (transmittance) {12} to correlate the optical changes with a battery's SOC {14}.

2.1 Thesis Outline

Chapter 1 covers background information relevant to the thesis work with focus on the components and dynamics of a LIB and optical properties of graphite, while Chapter 2 summarizes the overall objectives and tasks. Chapters 3 to 5 provides details on the specific experimental work conducted and discussion of the results. The work presented in chapters 3 and 4 are reprinted from three published peer-reviewed journal articles [1], [17], [18]. Chapter 3 introduces the initial characterization of commercial graphite electrodes through reflectance spectroscopy and initial development of lithium ion battery in-situ fiber optic evanescent wave sensing with spectroscopic measurements. Chapter 4 is dedicated to the optimization of the fiber optic evanescent wave sensing system with focus on three aspects. i) Fabrication of the sensor to maximize durability and sensitivity, ii) development of a method to embed the sensor within a commercially viable pouch cell instead of a Swagelok cell to reduce capacity fade, allow for long term testing and maximize the interaction between the sensor and the graphite electrode, and iii) use of an in-house narrow band optical sensor interrogator that replaces the spectrometer and reduces the cost of the sensing system significantly. Chapter 5 focuses on the theoretical output signal of the fiber optic sensor, which required the development of a lithiated graphite optical model and coupling it with a transport model for the lithium ion battery and an analytical model for the fiber optic sensor. The model predictions are compared to experimental results. An analysis of the effects of applied current on lithium ion diffusion and the ability of the sensor to

predict capacity fade are also presented in Chapter 5. Finally, Chapter 6 provides a summary and conclusions of this thesis and also presents future work that would promote the commercialization of the presented lithium ion battery sensing system.

3. Characterization of Commercial Graphite Electrodes and in Situ Fiber Optic Evanescent Wave Spectroscopy

This chapter is reprinted in adapted form with permission from [1]

A. Ghannoum, R. C. Norris, K. Iyer, L. Zdravkova, A. Yu, and P. Nieva, "Optical Characterization of Commercial Lithiated Graphite Battery Electrodes and in Situ Fiber Optic Evanescent Wave Spectroscopy," *ACS Applied Materials & Interfaces*, vol. 8, no. 29, pp. 18763–18769, Jul. 2016.

3.1 Introduction

A wide array of electrode chemistries can be used in LIBs [55]. The benefits of a given configuration depends on several parameters, which include the cost, durability, environmental effects, operational safety and specific energy density. In this chapter we focus on a commercial battery fabricated by former A123 Systems Inc. containing $LiFePO_4$ as a cathode and graphite as an anode. $LiFePO_4$ is inexpensive, environmentally benign and abundant cathode material used for rechargeable LIBs, which has a theoretical capacity of 170 mAh g^{-1} [56]. Graphite has a higher capacity (372 mAh g^{-1}) and is commonly used in LIBs due to its highly reversible lithium (Li) ion intercalation, good electrical conductivity, simple preparation process and low production cost [4].

Electric vehicles are powered by battery packs consisting of battery cells connected in series. Based on estimates of the state-of-charge (SOC), state-of-health (SOH), failure status and life expectancy of individual cells, a control system is used to manipulate the charging and

discharging processes. The existing SOC estimation methods are based on algorithms (e.g., Kalman filters) that depend on externally measured parameters (i.e., current, voltage and temperature). The required accuracy in SOC estimation depends on the application since the sensors employed to measure the voltage of individual cells and collect electric current data significantly affect the cost [57]. Implementation of real-time in-line voltage measurements of cells connected in series with varying voltage reference levels is complex [58]. Real-time measurements are also affected by uncertain drive cycles [59]. Additionally, SOC is correlated to the open circuit voltage (OCV) of the battery cell; however, the direct measurement of OCV is not possible during battery operation. Some SOC estimation methods rely on electric current integration, which is highly dependent on the accuracy of electric flow measurements. An error in the measurement can accumulate in an open-loop calculation and SOC estimation without a corrective step eventually becomes inaccurate [59]. Investigating other variables that may assist or replace voltage and current measurements to estimate SOC is of great interest. It is suggested that a non-electronic in-situ optical measurement may contribute to the estimation of SOC. Compared to electronic sensors, optical-based sensors are less sensitive to electromagnetic interference. Additionally, since they can be composed of dielectric materials such as silica, optical sensors may tolerate the internal chemical environment of a LIB.

Graphite-based anodes are comprised of graphite micro-particles covered with a solid electrolyte interphase (SEI) layer composed of organic and inorganic compounds, which forms during the charging of the battery as the electrolyte undergoes reduction reactions at the electrode surface [36], [37]. The SEI layer acts as a screen that permits the flow of Li ions, and

prevents further reduction of electrolyte and co-intercalation of solvent molecules into the electrode [60]. The optical reflectivity of a graphite anode in the infrared region (5–20 μm) is influenced by the chemical components of the SEI layer [20], however graphite is known to dominate absorption in the infrared region [41], [61]. An optical sensor that functions at wavelengths lower than the infrared region would avoid the effect of the dynamic SEI. Studying the reflectance of graphite electrodes as a function of wavelength at various lithiation stages is essential in the development of an in-situ optical waveguide sensor, which can be embedded in a LIB for real-time estimation of SOC. Additionally, this in-situ optical measurement technique, which relies on direct interaction between optical waves and the cell electrochemistry, may reveal other dynamic changes inside the cell which are not observable through voltage and current measurements. Direct measurement data may also be used as a comparative benchmarking real-time characterization tool during battery production and used to better understand the long-term internal evolution that may affect the stability and life of a battery.

This chapter reports a study on the reflectance of commercial graphite anodes charged to specific states of charge to investigate the dominance of graphite in governing the optical properties of a commercial graphite electrode in relation to SOC. Real-time fiber evanescent wave spectroscopy (FEWS) was also performed to determine the potential wavelengths that can be used to track the lithiation process of a graphite electrode. The optical fiber is tested with electrolyte solutions with varying salt concentrations to affirm that the electrolyte does not affect its transmittance.

3.2 Experimental

3.2.1 Materials

Commercial cylindrical $LiFePO_4$-graphite cells APR18650M1-B (1.1 Ah) were acquired from former A123 Systems Inc. The lithium-ion battery cells were charged to various states of charge and then disassembled in an inert environment to obtain the commercial graphite electrode samples for reflectance measurements, as described in detail elsewhere [62]. A multi-mode optical fiber (AFS105/125Y, Thorlabs) etched using a buffered oxide (JT5569-3, VWR) was used for in situ fiber evanescent-wave spectroscopy. The optical fiber was embedded in batteries fabricated using graphite and $LiFePO_4$ electrodes (MTI Corp.) separated by a 25 μm trilayer polypropylene-polyethylene-polypropylene membrane (Celgard®). The battery electrolyte consisted of a 3:7 (vol %) mixture of ethylene carbonate (BASF) and dimethyl carbonate (BASF) with 1 M lithium hexafluorophosphate ($LiPF_6$) (Purolyte®, Novolyte Technologies). Solution of electrolyte with varying $LiPF_6$ concentrations (0.25, 0.50, 0.75, 1.00, 1.25 and 1.75 M) were prepared to test their possible effects on the embedded optical fiber.

3.2.2 Reflectance Spectroscopy

The reflectance of the extracted commercial graphite anode samples was measured using a fiber optic spectrometer (OceanOptics USB4000) connected to a reflection probe (QR200-7-VIS-NIR, Ocean Optics) setup at 45^o in a customized apparatus with a tungsten halogen light source (OceanOptics LS-1). The 45^o mount is necessary in order to minimize the effect of

specular reflection. The wavelengths measured ranged from 500 to 900 nm. A summary of the procedure is described in Figure 8.

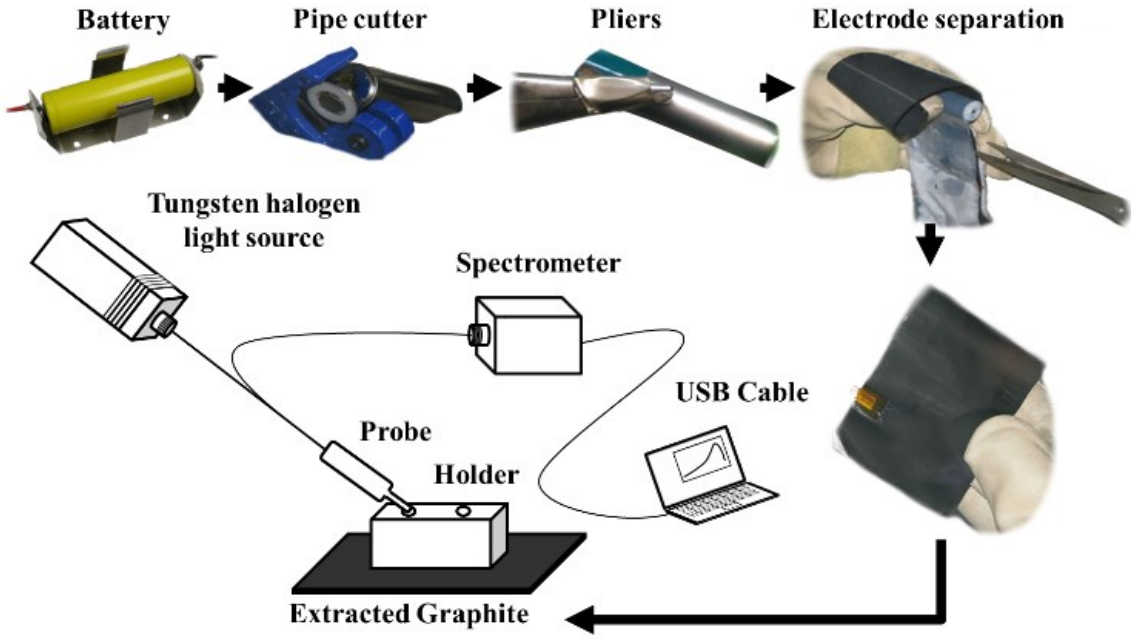

Figure 8: 10 Cylindrical $LiFePO_4$-graphite cells were charged to 30, 35, 40, 45, 50, 60, 65, 70, 75 and 80 % SOC. Disassembled using a pipe cutter and pliers; the graphite (anode) was extracted and rinsed using dimethyl carbonate. Images were taken of each graphite sample using a conventional camera and reflectance spectroscopy was performed as seen in the schematic. Reproduced in adapted form with permission from [1]. Copyright (2016) American Chemical Society.

3.2.3 In-situ Fiber Evanescent-wave Spectroscopy

The jacket (polymeric buffer) of a multi-mode optical fiber (AFS105/125Y, Thorlabs) was removed mechanically and the cladding was partially etched using a buffered hydrofluoric acid

(BHF) solution to a diameter of about ~105 μm (see Figure 9); the etched region is the sensing region. The etched fiber was embedded inside a custom designed Swagelok cell between the graphite electrode and separator (see Figure 10). This configuration allowed the graphite anode to act as an "optical cladding" that can absorb from the transmitted spectrum through the interaction between the evanescent wave and the graphite layer [63]. The same light source and spectrometer as in the reflectance spectroscopy setup were used to produce optical transmittance measurements. To study the electrolyte's influence on the optical fiber, three etched fibers were tested using the same setup seen in Figure 10 but instead of a Swagelok cell electrolyte solutions with varying $LiPF_6$ (salt) concentrations were used. In addition, to investigate the possible effects of the presence of the optical fiber on the graphite anode, six coin cells were fabricated using the same materials used in the Swagelok cell assembly, three of which contained multi-mode optical fibers (AFS105/125Y, Thorlabs).

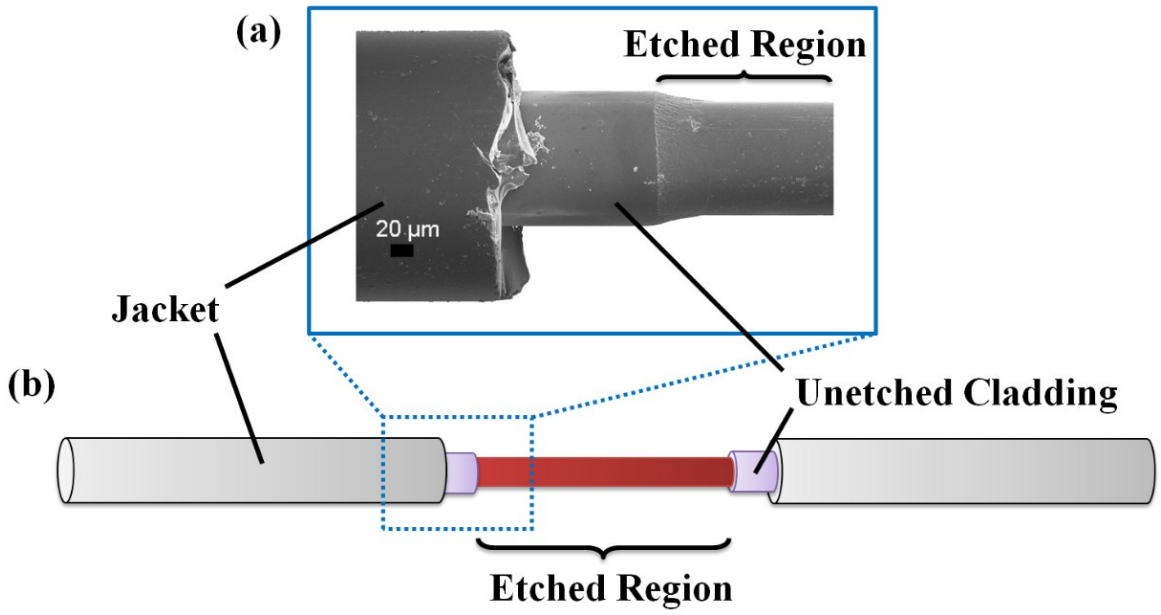

Figure 9: Scanning electron micrograph of an etched multi-mode optical fiber (AFS105/125Y, Thorlabs) and (b) a schematic of the optical fiber with the etched region highlighted in red.

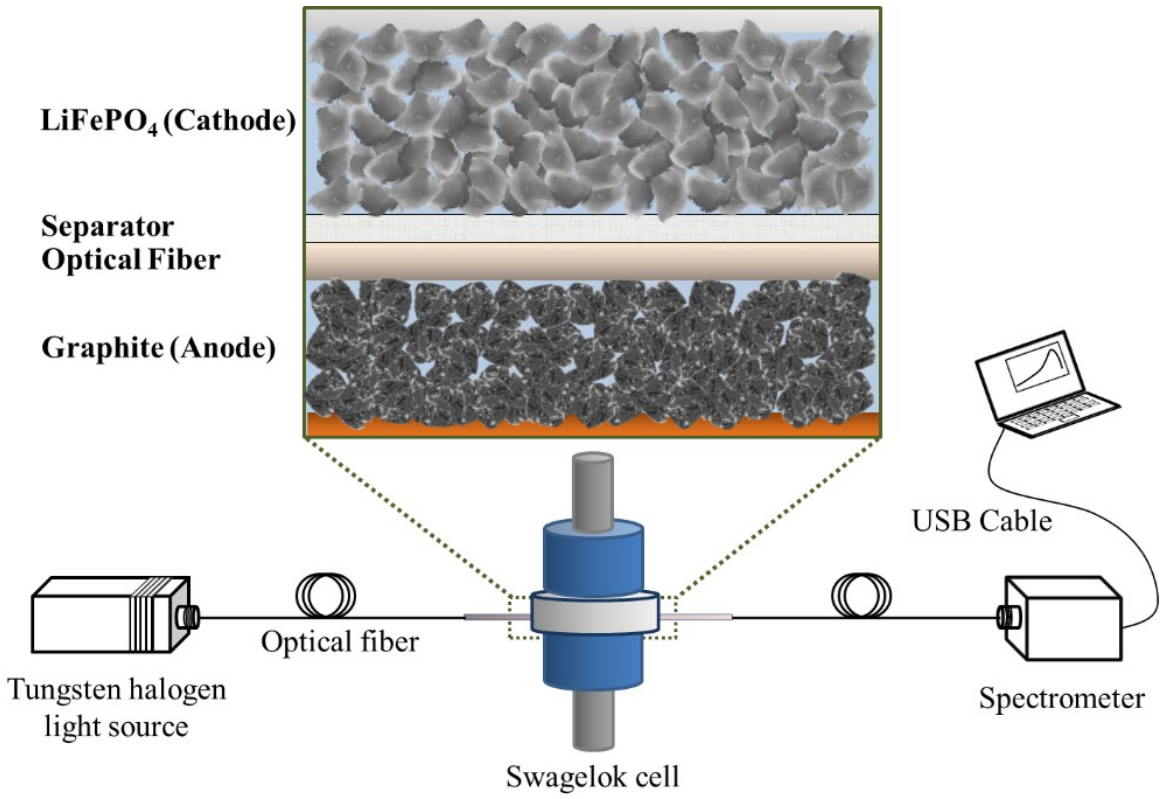

Figure 10: Schematic of the experimental setup for fiber evanescent wave spectroscopy with a detailed illustration of the modified Swagelok cell. Reproduced in adapted form with permission from [1]. Copyright (2016) American Chemical Society.

3.3 Results and Discussion

Pristine graphite has a relatively low free carrier concentration (~10^{-4} free carriers/atom) at room temperature [41]. As Li-ions intercalate and transfer/delocalize their 2s electron into graphite's π-band (see Figure 11), the carrier density in the graphite layers adjacent to the lithium layers increases [42]. The increase in the free carrier concentration changes the electrical, chemical, thermal, magnetic and optical properties of graphite [41].

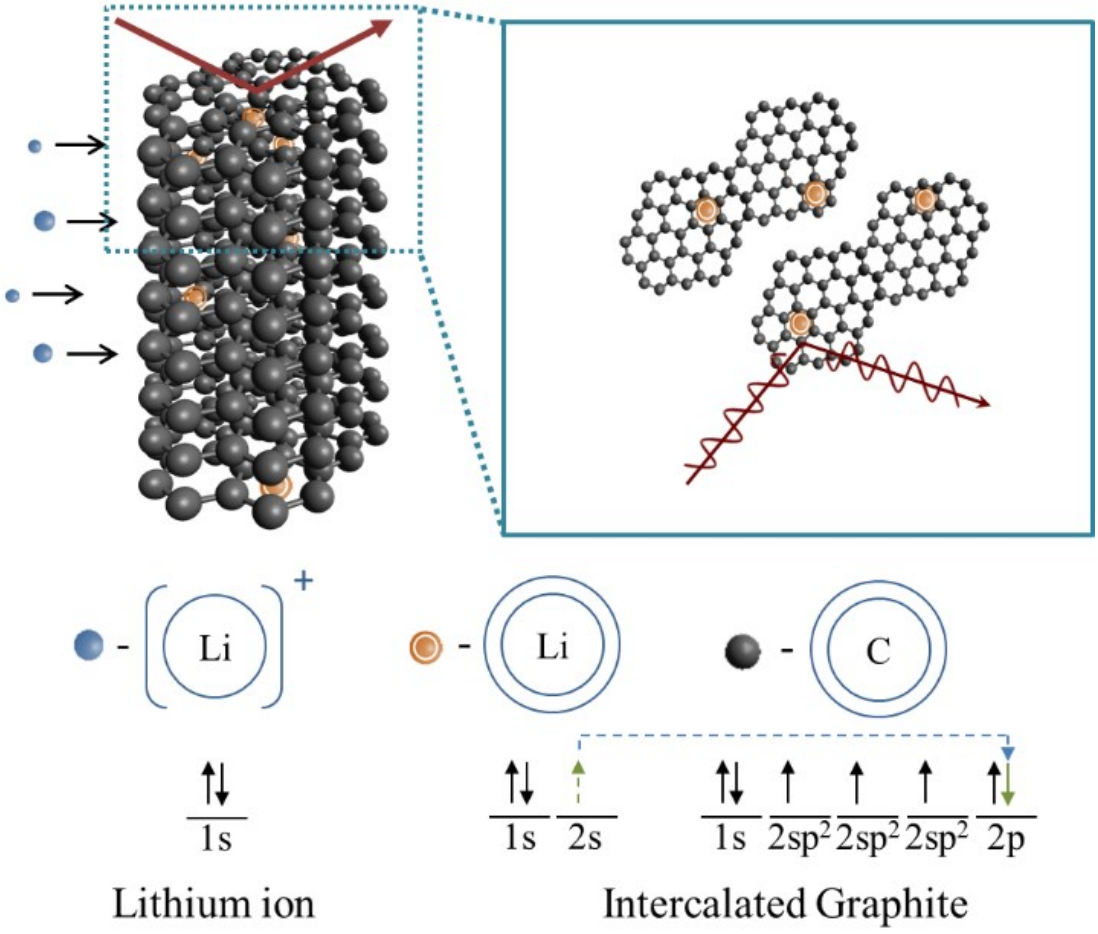

Figure 11: Schematic diagram of graphite's lithiation process with electron configurations for lithium ions and lithiated graphite; presumed photon scattering mechanism is shown with red arrows. Reproduced in adapted form with permission from [1]. Copyright (2016) American Chemical Society.

Optical reflectivity of pure stage phases of lithiated graphite have been studied in the literature using highly ordered pyrolytic graphite (HOPG) [39], [41], [43], [64], [65]. The reflectance of an amorphous carbon electrode (petroleum coke) has also been investigated during

its delithiation process in a prototype half-cell with a pure lithium anode positioned within an integrating sphere [44]. These studies form a basis for understanding the results obtained from the reflectance spectroscopy of commercial grade graphite anodes that are composed of various substructures (i.e., graphite micro-particles covered by an SEI layer, carbon nano-particles known as carbon black and carbon fibers) as seen in the scanning electron micrograph in Figure 12. Considering the sizes of the various substructures, graphite particles are significantly larger and dominate the surface of the electrode, while other components such as the carbon fibers may dominate other micro-sized regions. This is of significance since it demonstrates that while graphite may be in contact with an optical fiber positioned within a battery, the distribution of graphite particles near the optical fiber may vary, giving each battery its own interaction intensity fingerprint.

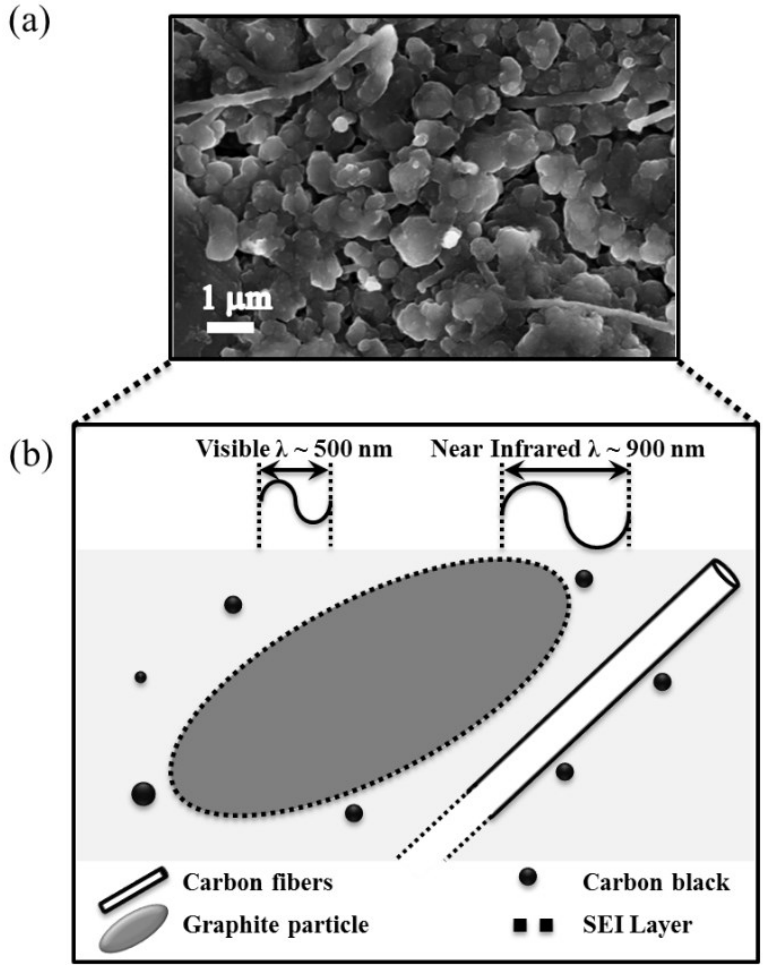

Figure 12: (a) Scanning electron micrograph of a graphite anode extracted from an APR18650M1-B type cell and (b) a schematic illustrating the various substructures present on a graphite electrode and their relative size in relation to the investigated range of wavelengths. Reproduced in adapted form with permission from [1]. Copyright (2016) American Chemical Society.

3.3.1 Colorimetry of commercial lithiated graphite.

The extent of the lithiation of graphite is characterized by the periodic arrangement of intercalated Li-ion layers. The number of graphite layers between adjacent layers of Li-ions defines the stage numbers based on the Rudorff model [26]. Stage I, II, and III lithiated graphite may be identified by their colours, which have been observed to be bright-yellow (golden), red and blue respectively. Stage IV and higher are identified with a colour that approaches the black colour of pristine graphite [66]. We conducted an initial colorimetry study on the extracted commercial graphite anodes to observe the extent of lithiation as SOC varies. Figure 13 shows digital images of extracted graphite anodes taken, using a conventional camera, immediately after disassembly.

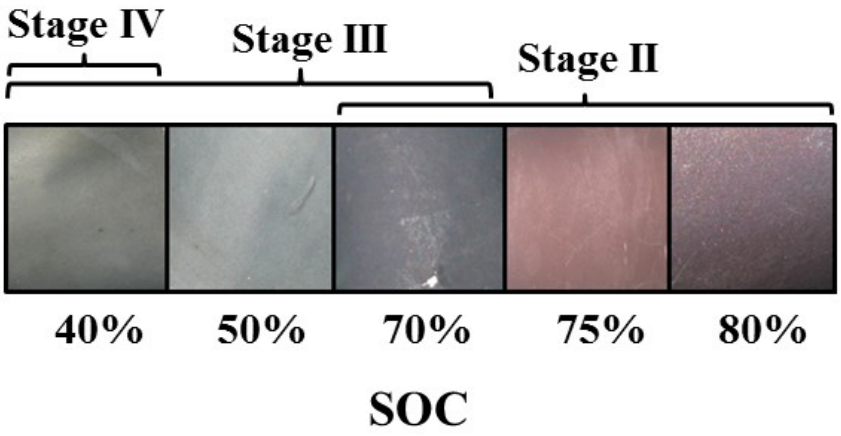

Figure 13: Images of the extracted graphite anodes at different SOC levels. Reproduced in adapted form with permission from [1]. Copyright (2016) American Chemical Society.

As SOC increases from 30 to 80 %, the colour of the anode progresses from grey-black to red-black. At 40 % SOC, grey is the dominant colour with the occasional blue striation along the

length, whereas light-grey is dominant at 50 % SOC, and variations of red and black are observed in the extracted graphite anodes at 70 % to 80 % SOC. The light-grey (50 % SOC) tone may indicate a gradual progression toward the black colour of pure-graphite associated with lithiation Stage IV, also observed by Marie et al. [25]. The presence of grey tones and blue striations (40 %) may be indicative of lithiation Stage III. Red tones (70 to 80 %) may suggest the attainment of lithiation Stage II. The results support the correlations between the colour of the extracted electrodes with their state within the LIB and the dominance of graphite in governing the anode optical properties. The absence of bright-yellow colours in the electrode samples shown in Figure 13 indicates that the capacity of the graphite anode was designed to be greater than that of the cathode in order to prevent full-lithiation (lithiation Stage I) of the graphite anode. This design approach can mitigate capacity degradation and fade that would occur if graphite is over-lithiated and Li metal is deposited [67]. Some of the extracted graphite electrodes deviated slightly from the observed colour trend. Graphite electrode samples were obtained from different sections of the disassembled batteries and showed that the electrochemical composition varied with position, as reported by Maire el al. [25].

While the colorimetry results display the various colours of the electrode at various SOC with an observed trend but positional dependency, reflectance spectroscopy provides a more accurate measurement of the specific wavelengths reflected from the electrode surface. The qualitative colour description of graphite described here is quantitatively characterized utilizing reflectance spectroscopy in the next section.

3.3.2 Reflectance Spectroscopy: Visible and Near Infrared Wavelengths.

The optical reflectivity of lithiated graphite has been observed to resemble that of metals, where a drop in reflectivity is observed at a specific frequency (plasma frequency ω_p) known as the Drude edge [41]. The Drude edge occurs when photons are absorbed by free electrons, which then oscillate causing a significant drop in reflectivity, as described by the Drude model. Reflectivity increases as the frequency of the photons decreases below the ω_p. The process of Li intercalation increases the carrier density in graphite and shifts the ω_p to higher frequencies (i.e., smaller wavelengths) [41]. The results of reflectance spectroscopy performed on the graphite anode using the system described in Figure 8 for wavelengths ranging from 500 nm to 900 nm are shown in Figure 14.

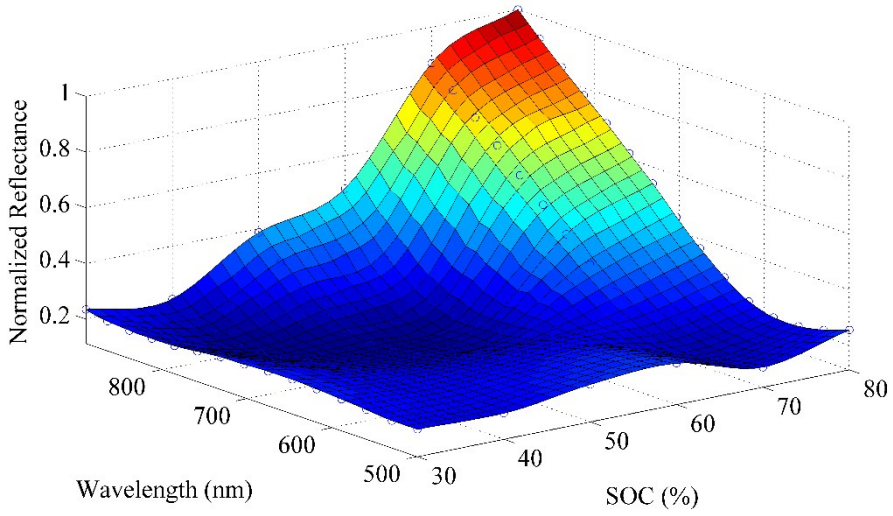

Figure 14: Reflectance spectroscopy measurements of commercial graphite anodes. Reproduced in adapted form with permission from [1]. Copyright (2016) American Chemical Society.

These results were obtained from a macro sized area on the order of 5 millimeters. This area is much larger than that of the individual sub-structures found in a graphite electrode seen in Figure 12. Hence, the measured reflectance is a macro-measurement. Positional dependency was observed in colorimetry, which may have arose due non-homogeneities on the electrode surface caused by the fabrication process [25]. As a result, the single spot reflectance spectroscopy measurements presented here represents a local macro reflectance that is characteristic of the composition, sub-structures and local state of lithiation. The optical properties are also known to be highly anisotropic, where the outcome of a light wave propagating parallel to the graphite sheets would be different than one propagating perpendicularly [41]. Thus the local bulk reflectance may be distinguished from an ideal homogenous electrode and a pure-phase lithiated graphite such as the ones synthesized by Basu et al. [39].

The reflectance spectrum for the commercial graphite anode at 30–60 % SOC in Figure 14 displays more prominent reflectance of green (500 nm), yellow (590 nm) and near infrared (NIR) (885 nm). From 60 – 80 % SOC, NIR and red (750 nm) reflectance increases significantly while yellow and green decrease. At 70 – 80 % SOC, reflectance of red dominates relative to the other visible colours. This reaffirms the observed red colour of the colorimetry images obtained from the graphite anode charged to 75 and 80 % SOC (see Figure 13). The results therefore indicate that higher wavelengths toward NIR are more sensitive to SOC.

Over the range of wavelengths investigated, a shift in the reflectance minima λ_{min}, is observed. As SOC increased the density of free electrons increase and cause the λ_{min} to occur at higher frequencies, as specified by the Drude model that relates the λ_{min} to the free electron

density [41]. The general reflectance spectrum of the extracted graphite anodes obtained in this work show notable differences compared to the in-situ diffuse reflectance spectrum of the less ordered lithiated petroleum coke powder reported by Xie et al. [44]. It is critical to note that the extracted graphite anodes theoretically could only be charged to about 170 mAh g^{-1}, which is the theoretical capacity of the cathode ($LiFePO_4$). To draw a comparison between the results reported for the in-situ diffuse reflectance study by Xie et al. we assume that 30 to 80 % SOC is equivalent to about 50 to 140 mAh g^{-1}. At 800 nm between 30 – 60 % SOC (50 – 104 mAh g^{-1}) the extracted graphite anode exhibited a minor decrease in reflectance followed by a steady increase with varying slopes, while petroleum coke showed a gradual decrease in reflectance. At higher states of charge (>60 %) graphite displayed a significant increase in reflectance at 800 nm. Petroleum coke also displayed a significant increase in reflectance at higher SOC, which has been attributed to the increase in free carrier concentration [44]. The reflectivity studies done on pure-phase LiC_6 and LiC_{12} by Basu et al. also show an increase in reflectance but comparing the results of highly lithiated pristine surfaces would be an extrapolation. These results support the conclusion that graphite in a commercial graphite anode has a large impact on the reflectance of the anode for wavelengths ranging from 500 to 900 nm, even with the existence of sub-structures, with the highest change observed at higher wavelengths.

3.3.3 Fiber Evanescent-Wave Spectroscopy.

In order to enable in-situ optical characterization of the graphite anode, fiber evanescent wave spectroscopy (FEWS) was chosen. FEWS provides a cost-effective, real-time, non-destructive and robust method to optically interrogate a harsh environment such as the anode of a

cell. Considering that the lithiation of graphite has been observed to change the degree of absorption and scattering of light as shown in Figure 14, FEWS allows for sensing changes at the interface between the fiber and the active material that undergoes a shift in optical properties [63]. Thus, changes in the optical properties of a graphite anode due to lithium intercalation can be measured and externally interrogated.

As shown in Figure 15, the FEWS sensor used in this work is a multimode fiber with an etched region where the cladding is thinned out to allow the evanescent wave to escape. This evanescent wave interacts with the material surrounding it. Depending on the refractive index and absorbance of the material, it modulates the intensity of the light coupled back into the carrier fiber. The intensity of the evanescent wave from a waveguide is a function of the refractive index of the cladding material and the distance from the core-cladding interface. Thus, the intensity of the evanescent wave incident on the electrode can be controlled by controlling the thickness of the remaining cladding. A thinner cladding allows a higher degree of evanescent wave coupling with the surrounding material while a thicker cladding reduces the evanescent wave coupling. In our case, the thickness of the cladding is engineered so that we can obtain a representative readout from a relatively long sensing length. Owing to the high absorptivity and scattering properties of the graphite electrode, a thinner cladding would increase the absorbance of the FEWS, thus decaying the intensity of the emitted light. Thicker cladding would reduce the interaction of the evanescent wave with the material being sensed (i.e., the graphite anode). Hence, this engineered cladding thickness allows for a sensor to sense changes in the graphite over the entire length of the anode electrode of 0.8 cm without complete attenuation of the

optical signal due to absorption by graphite. As a battery charges the electrodes undergo volume change [68] that produce a strain [69] within a battery. The graphite electrode expands during charging, which could decrease the optical fiber signal if significant micro-bending [70] occurs.

Hydrofluoric acid (HF) forms in a battery when the common salt $LiPF_6$ decomposes into LiF and PF_5, which can react with water to produce PF_3O and HF [71]. Since this reaction degrades the battery, it is therefore essential to avoid water during the battery fabrication process to prevent HF formation. The cladding thickness of an optical fiber could potentially be altered through etching if sufficient amount of HF forms within the battery during operation. Although measures have been taken to avoid HF formation, higher loss in the transmittance signal might be observed if HF does form during the long term operation of a battery and etches some of the cladding. Further development of the FEWS optical fiber system implemented as a sensor should consider variations in the transmittance due to possible deterioration of the cladding in the presence of HF during long term cycling of a battery.

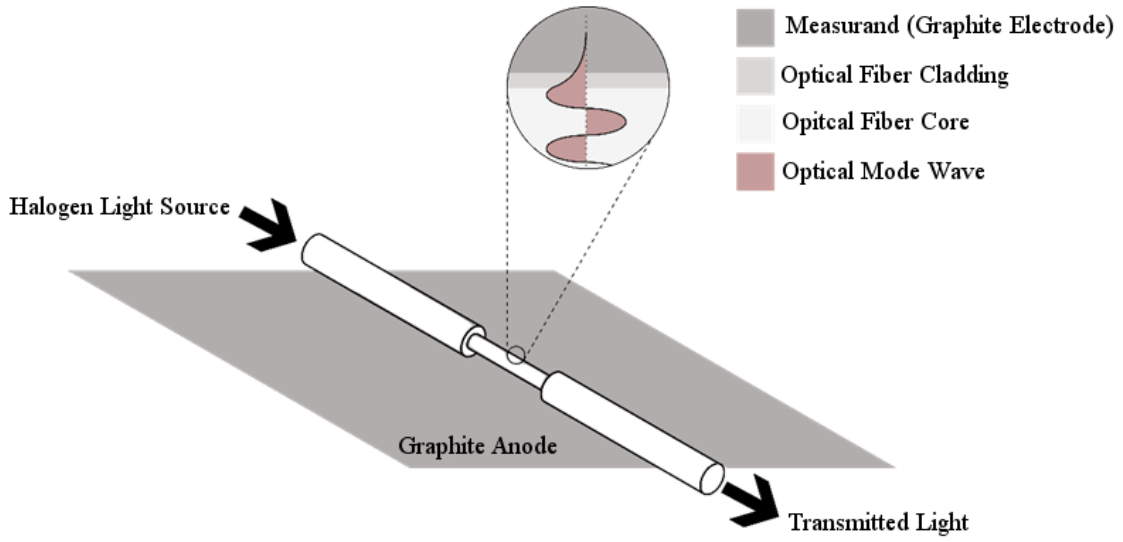

Figure 15: Illustration of a FEWS sensor and illustration of standing wave pattern and exponentially decaying evanescent wave. Reproduced in adapted form with permission from [1]. Copyright (2016) American Chemical Society.

In the modified Swagelok cell, the optical fiber covers a region of about 1.7 % of the graphite electrode. This region can be considered negligible in relation to the total graphite electrode size to produce an observable effect on the overall capacity of the cell. However, the optical fiber does apply a slight increased pressure on the graphite immediately beneath it as the outer current collectors apply a pressure on both sides of the optical fiber (see Figure 10). Depending on the extent of the applied pressure, the electrodes kinetics may be affected due to the reduction in the space between particles, which reduces the interaction between the graphite particles and the electrolyte [72, p. 2]. To overcome and minimize any possible effects on the kinetics of the graphite electrode, a low applied current of 0.1C was used. Further development in the implementation of an optical fiber sensor within a commercial battery will require

reconfiguration of the optical fiber within the battery to eliminate/minimize variations in pressure. It should be also noted that for the purpose of this work, the magnitude of the electric field produced by the amount of light transmitting through the optical fiber was not considered to significantly affect the lithiation of the battery when compared to the electric field generated by the battery's electrodes.

The battery electrolyte present at the interface between the optical fiber and the graphite electrode may interfere with the FEWS measurements in two possible ways. The first one is a possible constant loss (i.e. baseline shift) in the transmittance due to its presence. The second one might be related to the change in salt concentration during battery operation and its effect on the electrolyte optical properties. During charging and discharging, the electrolyte salt concentration deviates near the graphite particles from the initial 1 M as lithiation occurs, the degree of deviation depends on the magnitude of applied current [53]. To determine the effect of the electrolyte, FEWS optical fibers were positioned in an electrolyte solution with a salt concentration of 1 M $LiPF_6$ and also in air using the same setup found in Figure 10. For wavelengths ranging from 500 to 893 nm, the average transmittance loss was 0.20 % in the presence of electrolyte when compared to air. These results indicate that the electrolyte does not cause a significant loss in the transmittance when the battery is at equilibrium. To determine the effect of the electrolyte under non-equilibrium conditions, electrolyte solutions with salt concentrations ranging from 0.25 to 1.5 M $LiPF_6$ were also used. The resulting transmittance was measured for wavelengths ranging from 500 to 893 nm and plotted in Figure 16. The results show that the electrolyte does not significantly affect the transmittance of the optical fiber, with a

maximum observed transmittance change not exceeding 1.0 %. They also indicate that the electrolyte acts in the same way as the fiber cladding by allowing evanescent waves to pass through and interact with the graphite electrode.

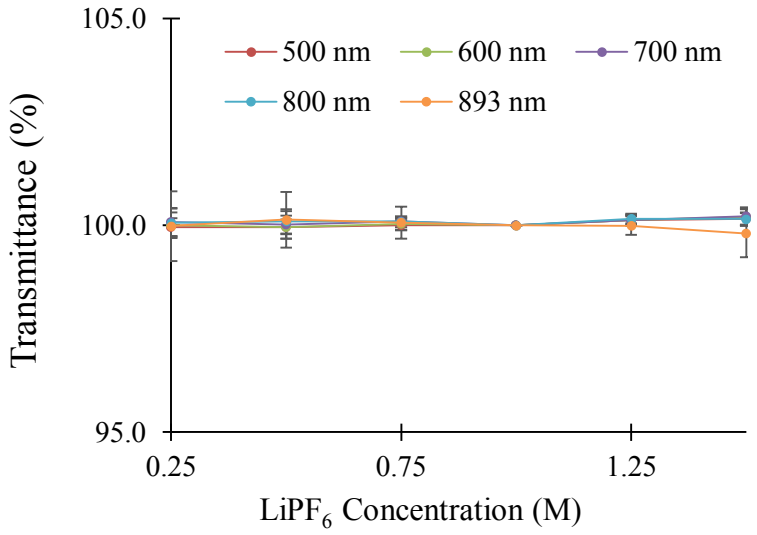

Figure 16: Percentage of transmittance of wavelengths ranging from 500 to 893 nm through etched optical fibers placed in electrolyte solutions (3:7 (vol %) ethylene carbonate and dimethyl carbonate) containing $LiPF_6$ concentrations ranging from 0.25 to 1.5 M. (Reference point was measured at 1 M $LiPF_6$). Reproduced in adapted form with permission from [1]. Copyright (2016) American Chemical Society.

FEWS transmittance measurements were made using a tungsten halogen light source setup as shown in Figure 10. The results were then normalized at every discrete wavelength using the equation $\Delta T\, T^{-1} = (T - T_{Final})\, T_{Final}^{-1}$, where T is the measured transmittance and T_{Final} is the

transmittance when the cell was fully discharged. This was completed for wavelengths ranging from 500 nm to 900 nm and plotted in Figure 17.

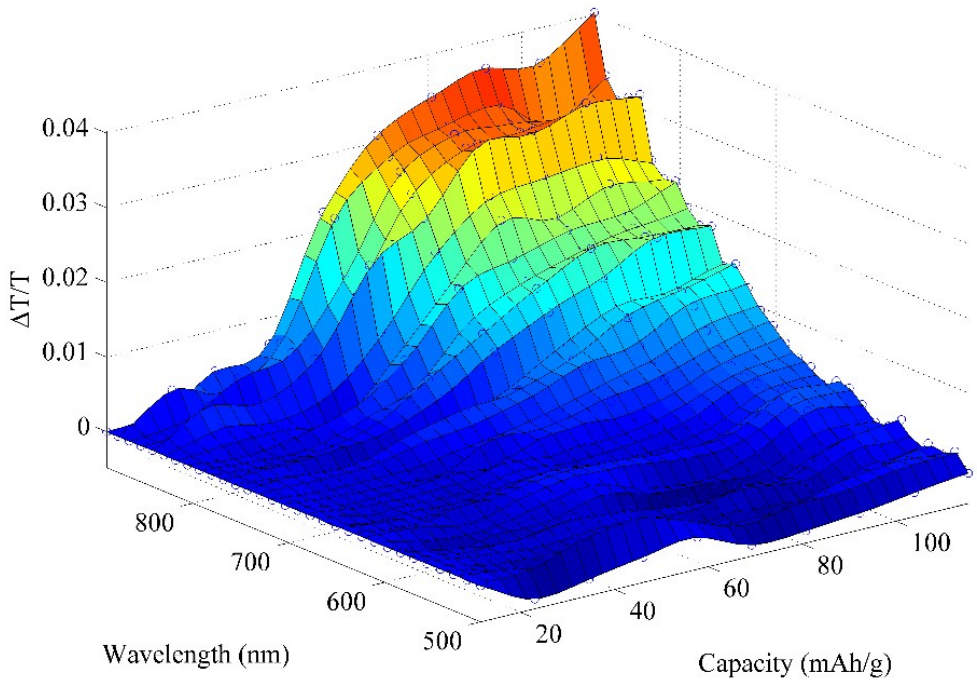

Figure 17: Embedded optical fiber normalized transmittance measured during graphite delithiation in a Swagelok cell as described in Figure 10. Reproduced in adapted form with permission from [1]. Copyright (2016) American Chemical Society.

The transmittance was measured using the above described FEWS sensor in direct contact with a coin-shaped graphite electrode with 0.8 cm diameter and a total capacity of 308 mAh g^{-1} measured based on parameters obtained from the manufacturer and half-cell testing. The Swagelok cell was assembled in-house in a full cell configuration in which the total capacity of the cell relied on the capacity of the limiting electrode ($LiFePO_4$). This resulted in a total first charge capacity of 160 mAh g^{-1} (cell potential, 3.7 V) when a current of 0.1C was applied. Since

an SEI formed during the first charge, some capacity was lost resulting in a discharge capacity of 115 mAh g^{-1} (cell potential, 2.5 V), which corresponds to a first cycle efficiency (FCE) of about 72 %. To verify that this loss is not just a phenomena observed in the modified Swagelok cell, the six coin cells fabricated with and without (reference cells) optical fibers of the same dimensions as the one used for the Swagelok were tested. The testing was performed by comparing the first cycle efficiency (FCE) of these two types of coin cell configurations. The reference coin cells showed FCEs of 74, 76 and 84 %. The coin cells containing the optical fibers had FCEs of 81, 83, and 84 %. These results were all within the range of expected variability in the FCE and can be mainly attributed to variations in the applied pressure used in the coin cells during fabrication since an increase in pressure is known to accelerate capacity fade [73]. The slightly lower FCE of 72 % measured in the Swagelok cell can be therefore attributed to the higher pressure conditions caused by the degree of turning of the Swagelok nut.

Considering that the discharge capacity was 115 mAh g^{-1} based on coulomb counting, it can be stated that the graphite anode was lithiated to about 40 % of its total capacity. Comparing this percentage to the general capacity of graphite vs. Li/Li^+, it is inferred that the graphite reached stage III (LiC_{18}) and approached stage II (LiC_{12}) when the cell was fully charged. Hence, the achieved lithiation stage in the in-house Swagelok cell is slightly lower than the lithiation stage attained by the commercial cylindrical cells.

The normalized transmittance plotted in Figure 17 corresponds to a delithiation (i.e. discharge) only, since noise was observed during the initial charge, which may be attributed to the formation of the SEI layer. As the Swagelok cell was discharged, a gradual decrease in

transmittance was observed with larger changes observed at the higher wavelengths. The transmitted wavelengths closely follows the trend observed in colorimetry as well as the reflectance measurements since the transmission of red shows the highest increase with SOC. Since transmittance increased with SOC, volume change of graphite particles does not seem to produce significant micro-bending to cause a decrease in the transmittance.

The direct correlation between the SOC and the transmitted signal in the red and near-IR region demonstrates the basis for a novel method to characterize the optical properties of the electrode in real-time as a function of the SOC. This allows for in-line monitoring of the optical properties of the battery electrodes which can then be correlated to the SOC. It should be noted that the transmittance of the FEWS is sensitive mainly to the outer surfaces of the graphite particles. Therefore the transmittance of the optical fiber is directly related to the lithium concentration at the surface of the electrode. The saturation/depletion of lithium at the surface of the graphite particles will produce the same transmittance measurements at any given rate. However, the limits to graphite lithiation and lithium migration would remain the same, as it is a material property [74]. Once the current stops, lithium may undergo migration within the particle and the transmittance measurement would change accordingly. The method of using an optical fiber is therefore adaptive to the applied current and might indicate the limitation of the actual material during cycling. Further studies are required to properly model the correlation between the optical properties of the electrodes and their electrochemical properties. Additionally, testing its reliability/feasibility when embedded within a battery system is required to determine its accuracy in estimating SOC over many cycles and varying rates of charge and discharge.

3.4 Conclusions

The optical changes of commercial graphite anodes were studied using lithium ion battery cells charged to 30, 35, 40, 45, 50, 60, 65, 70, 75 and 80 % SOC. The results through colorimetry support the dominance of graphite particles in governing the color of graphite anodes and that stage 2 lithiation (LiC_{12}) is the maximum lithiation stage achieved in this given battery configuration. The optical changes were also quantitatively studied by analyzing the reflectance of visible and infrared light (500 – 900 nm). The trends observed in the reflectance of the commercial anode in comparison to pure-phase lithiated graphite materials, also supports the dominance of graphite in governing the reflectance of graphite-based anodes. The results of the reflectance study of lithiated graphite demonstrate a direct correlation between the state of charge and the measured reflectance at wavelengths ranging from 750 – 900 nm (near-infrared band). In-situ fiber evanescent-wave spectroscopy, or FEWS, using wavelengths ranging from 500 – 900 nm was completed using a modified Swagelok cell. The FEWS results demonstrate a trend that closely follows the reflectance of the extracted commercial graphite anodes. They also demonstrate the ability to measure SOC with an optical fiber embedded in a graphite anode within a LIB. Further sensitivity and durability studies of the FEWS optical fiber system implemented as a sensor will be required to determine its accuracy in measuring SOC in LIBs in comparison to other conventional methods.

4. Optimization of Embedded Fiber Optic Evanescent Wave Sensors for Optical Characterization of Graphite Anodes in Lithium-Ion Batteries

This chapter is reprinted in adapted form with permission from [18]

A. Ghannoum, P. Nieva, A. Yu, and A. Khajepour, "Development of Embedded Fiber-Optic Evanescent Wave Sensors for Optical Characterization of Graphite Anodes in Lithium-Ion Batteries," *ACS Appl. Mater. Interfaces*, vol. 9, no. 47, pp. 41284–41290, Nov. 2017.

Parts of this chapter is reprinted in adapted form with permission from [17]

A. Ghannoum, K. Iyer, P. Nieva, and A. Khajepour, "Fiber Optic Monitoring of Lithium-Ion Batteries," in *IEEE SENSORS 2016 Proceedings*, Orlando, FL, USA, 2016, pp. 868–870. © 2016 IEEE.

4.1 Introduction

Optical fibers utilizing evanescent waves as a sensing mechanism have been used in various applications [75]–[79] due to their fast response, selectivity and durability [80]. In the previous chapter, a correlation between the degree of lithiation of commercial graphite anodes and the reflectance as measured by fiber-optic evanescent wave spectroscopy (FEWS) was demonstrated [1]. The spectroscopy results demonstrated significant increase in transmittance in the near-infrared band (i.e., 750–900 nm) when graphite was lithiated electrochemically. This illustrated that changes in the optical properties of graphite during lithiation can be observed using a FEWS [1]. This discovery allows for the simplification of the fiber-optic evanescent wave sensor's

(FOEWS) interrogation system, whereby a photodetector sensitive to near-infrared wavelengths can be utilized instead of a costly spectrometer to monitor a LIB [12]. The lithium content of a graphite anode is directly related to the SOC of LIB. The transmittance intensity of a FOEWS, which is affected by the lithium content in graphite, can hence be used to estimate the SOC of a battery. Capacity fade in a LIB results in a decrease in the range of lithiation/delithiation of graphite; this results in a decrease in the amplitude of the FOEWS's transmittance. This implies that the amplitude of the transmittance can be correlated to the state of health (SOH) of a battery.

The LIB environment can be considered a delicate but also a chemically harsh environment containing an anode, cathode, separator and electrolyte. Overcharging, excessive external stress, and contamination due to poor assembly can all lead to capacity fade by allowing lithium deposition, electrode detachment, electrolyte decomposition (side reactions) or separator pore size reduction[67], [73], [81], [82]. Consequently, it is essential that the assembly of a battery is studied and optimized when introducing a new component to the battery environment such as a fiber optic sensor. In this chapter, the development, embedding and performance characterization of the FOEWS are considered. Different etching solutions are studied in their ability to produce durable fiber optic sensors. The method of embedding the FOEWS into the LIB and its characterization have been developed to ensure maximum battery cell life and improved sensor sensitivity. The minimal capacity fade observed in all studied LIBs with embedded FOEWS, also demonstrates its commercial feasibility.

4.2 Experimental

4.2.1 Materials

The LIB sensor was fabricated using a step index multi-mode optical fiber (AFS105/125Y, Thorlabs) with a core and cladding diameter of 105 μm and 125 μm, respectively. The fiber was etched using both 49 % hydrofluoric acid (HF, JT9564-6, VWR) and buffered oxide etchant (JT5569-3, VWR). The ends of the FOEWSs were connectorized using universal bare fiber terminators (BFTU, THORLABS) with connectors (B10125A, THORLABS) attached. Glycerol (GX0185-2, EMD Millipore) was used to characterize the FOEWS's etched cladding prior to battery testing. Swagelok cells and pouch/prismatic cells were fabricated using graphite and $LiFePO_4$ electrodes (MTI Corp.) and a trilayer polypropylene-polyethylene-polypropylene membrane (Celgard) as a separator. The electrolyte consisted of a mixture of 1:1 (vol %) ethylene carbonate (BASF) and dimethyl carbonate (BASF), with 1 M lithium hexafluorophosphate (Purolyte®, Novolyte Technologies) as a salt. A graphite electrode slurry was prepared for embedding the sensors, which consisted of 26 % solids and 74 % liquid. The solid composition was 85 % graphite (43209, Alfa Aesar), 10 % poly(vinylidene fluoride) (182702, Sigma-Aldrich) and 5 % carbon black (Lib-SuperP, MTI Corp.), while the liquid composition was 100 % N-methyl-2-pyrolidone. An ethylene-vinyl acetate polymer-based hot melt adhesive (PLIB-HMA8, MTI Corp.) strip was attached to the sensors to ensure a proper seal during pouch cell fabrication.

4.2.2 Sensor/Battery System Preparation

The optical fibers were initially stripped to remove the polymer jacket surrounding the fiber using a mechanical and chemical process. A fiber stripper (ThorLabs T06S13) was first used to form a discontinuity on the fiber in the sensing region. This discontinuity was then immersed in acetone to allow the jacket to swell and delaminate from the underlying silica fiber. The polymer jacket was wiped away using lab wipes (VWR Spec-Wipe). This process ensured that the fiber experienced minimal amount of surface stress. When the jacket was removed exclusively by mechanical means, cracks and irregularities formed.

Once the polymer jacket was removed successfully, the unjacketed fibers were mounted in a custom fixture to hold them in place with the unjacketed portion left unexposed on the bottom. The fixture was then placed in a polypropylene beaker (1201-0250, NALGENE) (Figure 18a) containing buffered oxide etchant (J.T. Baker Buffered Oxide Etchant 5569). The fiber was allowed to etch in the buffered oxide. The etched fiber was then thoroughly rinsed using water and iso-propyl alcohol [1], [17]. The fiber was then observed under an optical microscope to obtain a rough estimate of the diameter and examine its surface for any defects such as cracks or undulations. Acceptable fibers obtained were then empirically characterized using glycerol. The primary performance metric used for this characterization method was the transmittance loss of the fiber immersed in glycerol compared to air. For this test, the fiber was temporarily connectorized (ThorLabs BFTU) and connected at one end to an LED light source (Vishay VSLY5850) driven at a constant current using a power supply (Agilent E3646A). The other end was connected to an InGaAs photodetector (Thorlabs DET10C) hooked up to an oscilloscope.

The voltage output read by the oscilloscope was correlated to the transmittance of the light sent through the optical fiber. The baseline transmittance of the fiber was measured in air. Low transmittance in air was indicative of cracks or gaps in the fiber. Fibers with low transmittance were discarded and fibers with high transmittance were immersed in glycerol. The reduction in transmittance due to glycerol was compared (as a percentage) to the transmittance in air and defined as the "fiber loss" [17].

The Swagelok assembly configuration was described in Section 3.2.3 [1]. Sensors used in pouch cells had two hot melt adhesive strips (MTI Corp.) attached about 3 cm from the center of the sensor to ensure a hermetic seal. The graphite/$LiFePO_4$ electrodes were cut into 3 cm by 2 cm rectangles and 1 cm by 2 cm of active material was removed to obtain square electrodes (2 cm by 2 cm). The region with the removed electrode material was reserved for current collecting tabs that were spot-welded (Figure 18b). Aluminum tabs (PLiB-ATC4, MTI Corp.) were used for the positive electrode ($LiFePO_4$) and nickel tabs (PLiB-NTA3, MTI Corp.) were used for the negative electrode (graphite). The separator was then placed between the electrodes and the sensor was positioned between the graphite electrode and separator. The stack was then sandwiched between two laminated aluminum sheets (alf-100-210, MTI Corp.) (Figure 18c). Three sides were sealed using a heat sealer (MSK-140, MTI Corp.). The open end was used to introduce electrolyte inside a glove box and then sealed using a Compact Vacuum Sealer (MSK-155A, MTI Corp.). The pouch was then placed on a 3D printed case to be held for testing (Figure 18d). A pouch cell with an embedded sensor was prepared by placing the sensor on the graphite electrode, pouring a slurry of graphite on top to envelop the sensor and then leaving it to air-dry

in a fume hood. The batteries were then cycled using an eight-channel battery analyzer (BST8-WA, MTI Corp.) and the optical signal recorded using a custom optical sensor interrogator (OSI).

The OSI consisted of a narrow band LED concentrated at 850 nm (Optek OPF370) that was driven at a constant current using a temperature-compensated low-dropout regulator. This LED was placed in a connector that allowed it to be mated to the sensor. The other end of the fiber sensor was also connected to the OSI. A silicon photodetector (Optek OPF480) was used to receive the intensity signal from the fiber sensor. The photodetector signal was then passed through a transimpedance amplifier (TI TLC2272) and the voltage output from this amplifier was fed into a 16 bit analog-to-digital convertor (ADC) (Microchip MCP 3427). The ADC passed the digital signal over I^2C to a microcontroller. This microcontroller then converted this I^2C signal into an actual voltage which could be read/recorded/plotted by a computer [17].

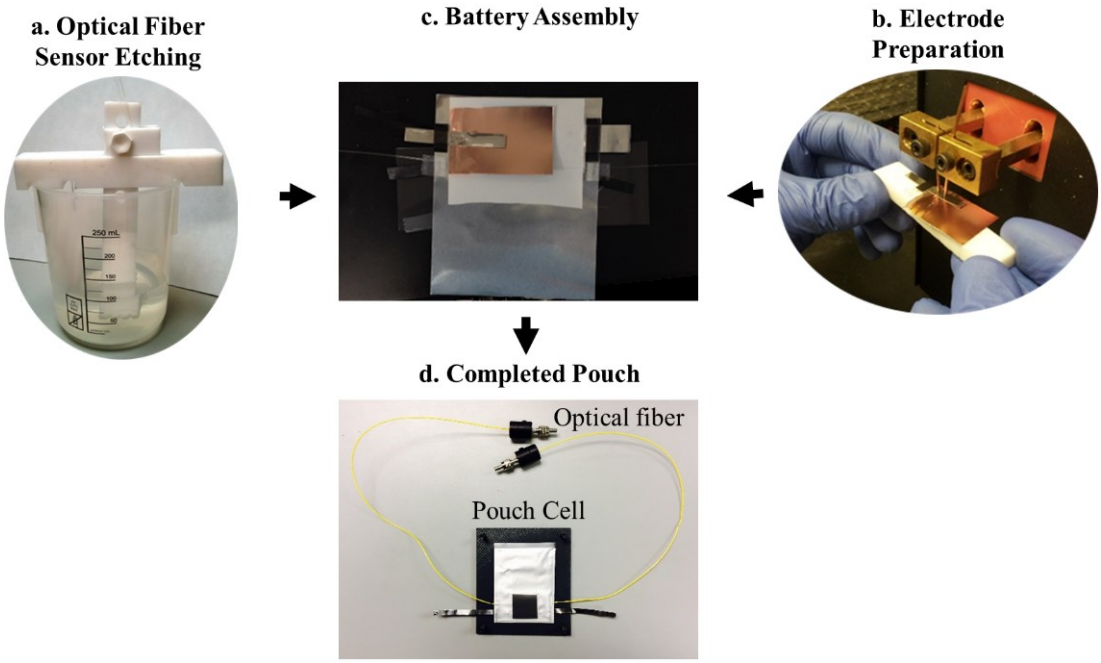

Figure 18: An overview of pouch cell with optical fiber sensor preparation process starting with a. optical fiber etching, b. spot welding of the current collectors to the electrodes and c. stacking the battery components (laminated aluminum, cathode, separator, anode and second laminated aluminum layer). d. Final assembled pouch cell with a connectorized FOEWS [18]. Copyright (2017) American Chemical Society.

4.3 Results and Discussion

4.3.1 Fabrication of Fiber Evanescent Wave Sensors

Etching of optical fibers using HF concentrations ranging from 48 to 52 wt % was done in the past to reduce the fiber diameter [83]. We first examined the use of a 49 wt % HF solution to etch the fluorine-doped silica cladding from the sensing region of the FOEWS. However, the

resulting sensor was fragile as it broke easily during handling and battery fabrication. In addition, the FOEWSs prepared using 49 wt % HF were found to have non-uniform surfaces as seen by scanning electron microscopy (SEM) (Figure 19a). Circular pits on the surface with diameters ranging from 3 to 25 μm were also observed.

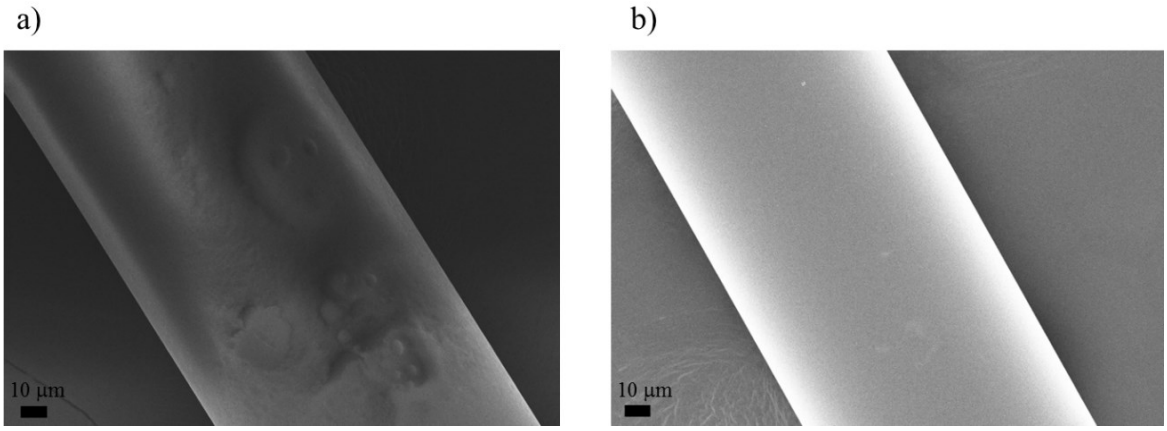

Figure 19: SEM micrograph of fiber optic evanescent wave sensors (FOEWS) etched using (a) concentrated HF (49 %) and (b) BHF (6:1 ratio of NH_4F to HF) [18]. Copyright (2017) American Chemical Society.

Etching solutions consisting of 6:1 to 10:1 mixtures of 40 wt % ammonium fluoride (NH_4F) and 49 wt % HF are utilized extensively to etch silica in the semiconductor industry and referred to as buffered HF (BHF) [84]. A 6:1 mixture (i.e. 34.3 wt % NH_4F and 7.0 wt % HF) was tested and found to produce FOEWS that could withstand the LIB fabrication process. As seen in Figure 19b, FOEWS prepared using BHF were observed to have smoother surfaces. The observed difference between the two fibers is believed to be due to the variation in the etching mechanism. The solution with higher concentration of HF etches more quickly [84] and favors

HF_2^- reactions with silica [85]. The second solution containing NH_4F however, had higher pH and favored HF reactions with silica over HF_2^- during the etching process [85]. The mechanism resulting in the non-uniformity in the fabricated FOEWSs is beyond the scope of this thesis, but the results indicate that using BHF solutions produces FOEWSs with higher durability, increasing the throughput of the sensor/battery fabrication process.

4.3.2 Fiber Optic Evanescent Wave Sensors in LIBs

Two LIB configurations were used with the developed FOEWS and tested: (1) Swagelok and (2) in-house pouch cell, as shown in Figure 20. The Swagelok configuration allows for repeated testing of the same FOEWS since the cell can be disassembled and the electrodes replaced. With careful handling, a sensor can be tested up to three times within one Swagelok cell. Theoretically, the FOEWS should not break but because the assembly takes place in a glove box, handling can be difficult.

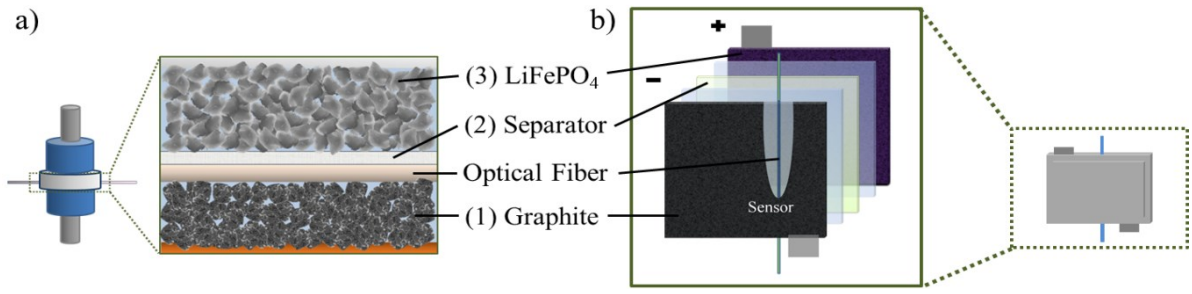

Figure 20: The FOEWS in two LIB configurations: (a) Swagelok and (b) pouch cell. Both cells contained three layers: 1. graphite electrode 2. separator 3. lithium iron phosphate ($LiFePO_4$), with a fiber optic sensor positioned on the graphite electrode [18]. Copyright (2017) American Chemical Society.

The Swagelok cell was reported to have a low first cycle efficiency (FCE) of 72 %, attributed to the higher pressure conditions within the cell when compared to those in other configurations such as coin cells [1]. It was difficult to precisely control the applied pressure because it depended on the tightness of the Swagelok nuts. However, decreasing the degree of turning would increase the risk of contamination by air. Hence, a second generation of Swagelok cells was fabricated by reducing the applied pressure and keeping them in an inert environment to avoid air contamination. With these precautions, a FCE of 83.2 ± 3.00 % was achieved, which is comparable to the reported FCE of coin cells tested with the same electrodes [1]. Graphite electrodes were extracted from the Swagelok cells after cycling and examined by SEM to observe the structural effect of the FOEWS on the graphite electrode. As seen in Figure 21Figure 8, a "trench" was formed on the graphite electrode in the region where the FOEWS was positioned covering about 1.7 % of the entire area. The increased strain in this trench was expected to cause a variation in the performance of the electrode in the region below the sensor compared to the bulk region [73]. This variation could cause the sensor signal to primarily reflect the local region, but could be correlated to the overall SOC as the local strain is constant (i.e. lithiation/delithiation dynamics are constant). For preliminary testing, the Swagelok configuration was considered ideal but not sufficient for long term testing due to observed capacity fade after several cycles.

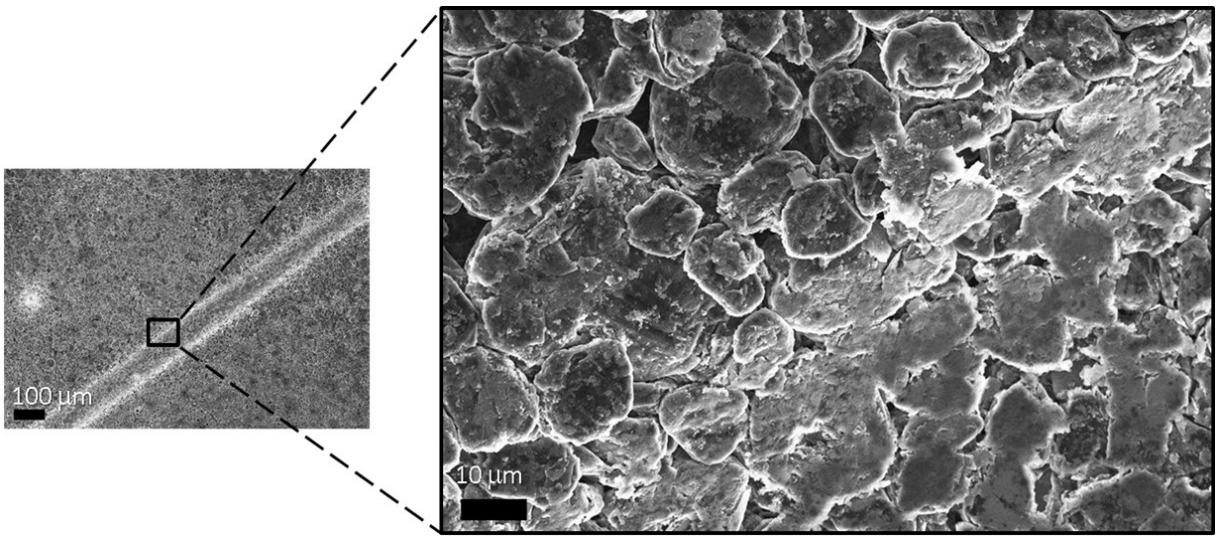

Figure 21: SEM of a graphite anode extracted from a Swagelok cell that has completed two cycles, demonstrating the trench formed by the presence of a FOEWS on the graphite electrode [18]. Copyright (2017) American Chemical Society.

For improved pressure control, reduced capacity fade and increased packing efficiency, the pouch cell configuration shown in Figure 20b was chosen over prismatic and cylindrical cells. The incorporation of a FOEWS requires the use of a polymer-based hot melt adhesive around the optical fiber exit points from the pouch cell to avoid air from seeping into the pouch [17]. Moisture in the air reacts with the salt $LiPF_6$ to form PF_3O and HF that would cause battery degradation [71]. As a battery cycles, the applied pressure on the electrodes increases during charge and decreases during discharge due to volume change [73]. The assembled pouch cells were hence placed in custom housings to apply an initial pressure of 4 psi promoting uniform current distribution and minimizing rippling of the electrodes resulting in lower capacity fade [73]. Using this in-house pouch cell configuration, a FCE of 87.2 ± 2.5 % was achieved, which

exceeded the performance of both the coin cells and second generation Swagelok cells with the same electrode material. Electrodes from the in-house pouch cells were also examined using an SEM to determine the degree of deformation caused by the presence of the FOEWS. As seen in Figure 22, the graphite electrode in the pouch cells did not undergo significant deformation as compared to the Swagelok cells, which demonstrates that the Swagelok cells were cycling at a larger applied pressure promoting an increase in the rate of capacity fade. However, the area of the FOEWS interfacing with the graphite anode in the pouch cell is smaller, since the deformation and indentation occurring in the electrode are smaller as seen in Figure 22.

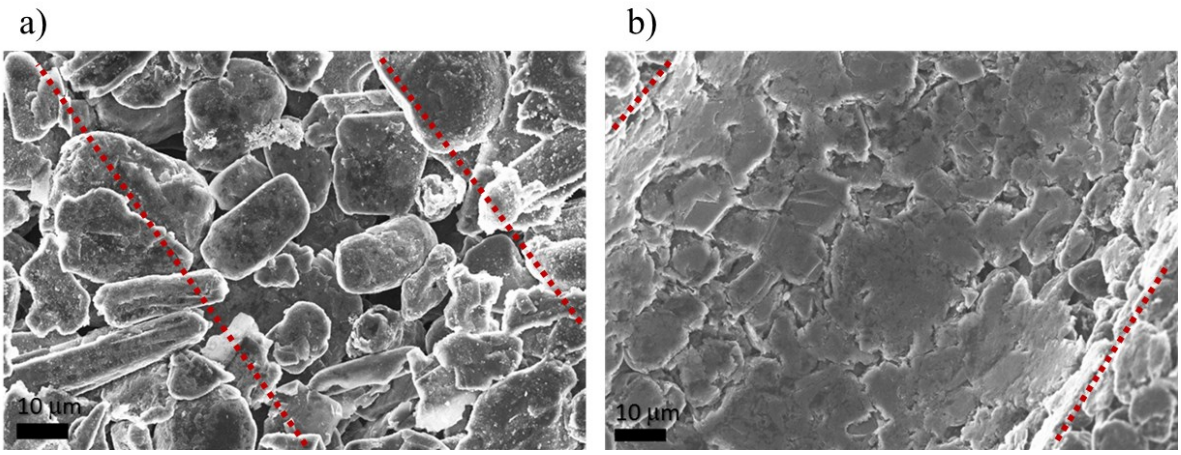

Figure 22: SEM micrographs of the region where the FOEWS was positioned (between the dotted lines) on the graphite anode extracted from (a) an in-house pouch cell and (b) a Swagelok cell [18]. Copyright (2017) American Chemical Society.

To maximize the interaction between the FOEWS and the graphite electrode a slurry of graphite was prepared to completely embed the FOEWS (see Figure 23). Embedding the sensor allowed for easier pouch cell assembly since the sensor was fastened to the graphite electrode. In

an industrial process, this would ensure higher throughput in a production line. The three tested configurations are illustrated in Figure 24, where the sensor in the Swagelok cell sits deeper into the graphite electrode when compared with the pouch cell, as observed by the larger trench in Figure 22. However, the embedded sensor is positioned on top of the original electrode with a layer of added slurry to encompass the sensor's diameter. The results from testing the three configurations are discussed in the next section.

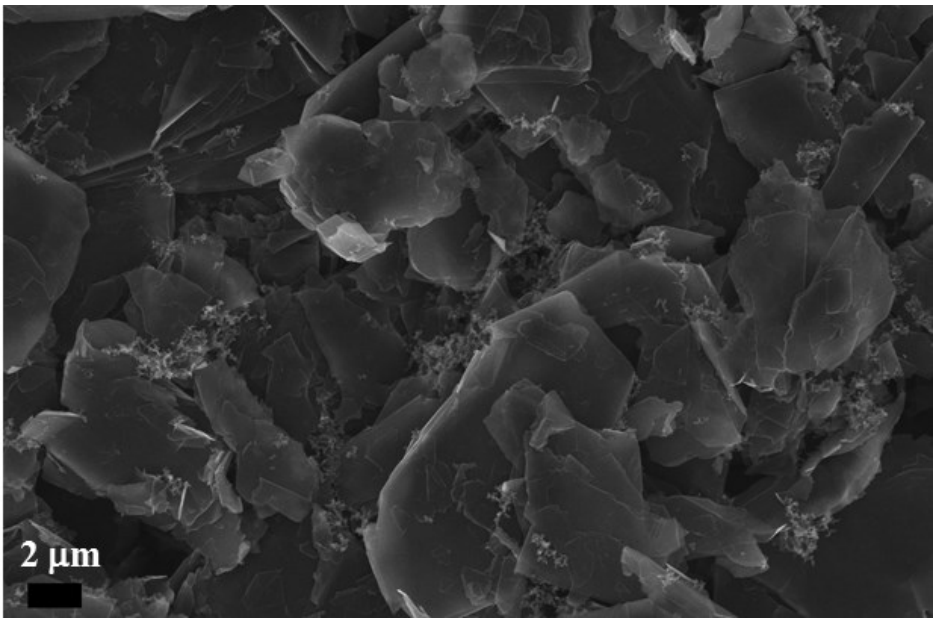

Figure 23: SEM micrograph of prepared graphite slurry for embedding the FOEWS sensor [18]. Copyright (2017) American Chemical Society.

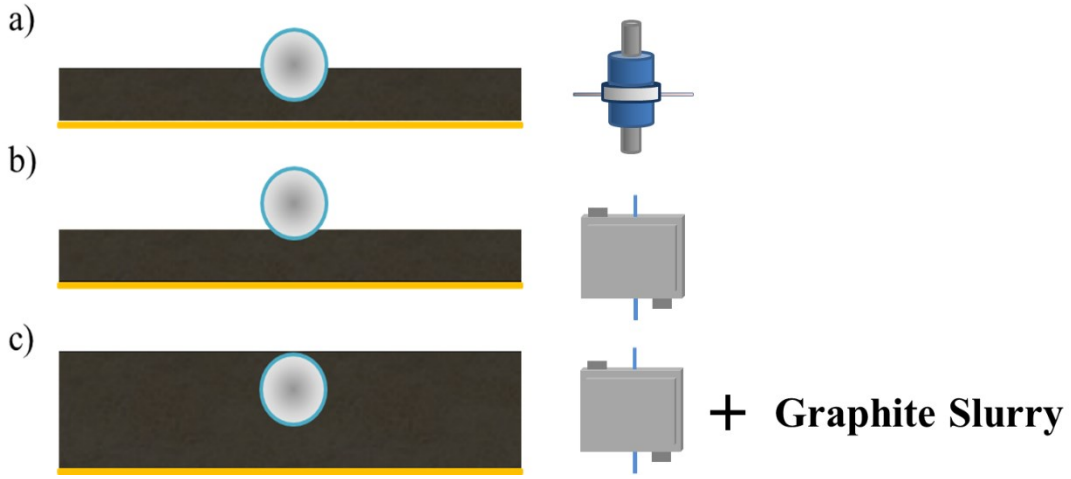

Figure 24: Schematic illustration of the cross-section of the FOEWS positioned within the graphite anode in (a) Swagelok cell (based on Figure 22b), (b) pouch cell (based on Figure 22a) and (c) pouch cell with added slurry (Figure 23) to embed the sensor [18]. Copyright (2017) American Chemical Society.

4.3.2 Fiber Optic Evanescent Wave Sensor Transmittance and Glycerol Testing

The fabrication of FOEWS for LIBs requires a validation step to ensure the etched optical fibers are functional and sensitive to changes within the battery. Many sensors were fabricated and tested with 100 % glycerol to ensure that the optical fibers are not over-/under-etched and to correlate the transmittance loss in glycerol to the sensor sensitivity in a LIB. Transmittance through an optical fiber relies on the refractive index difference between the core of the fiber and the cladding (i.e., the layer around the core); the core's refractive index must be higher than the cladding to allow total internal reflection to occur [86]. Adding a temporary layer of glycerol on the etched sensors would indicate if the cladding still exists on the fiber and the condition for total internal reflection still exists since the refractive index of glycerol (i.e., 1.4656 at 850 nm

[87]) is higher than the refractive index of the core (silica) (i.e., 1.4525 at 850 nm [88]). If a cladding does not exist 100 % loss in transmittance is observed when glycerol is placed on the etched fiber, which translates to a sensor with no signal in a battery. Etched FOEWS with about 85 to 96 % loss in glycerol were tested in LIBs. To compare the various cells, the LIBs were cycled from 0 to 100 % SOC based on the battery voltage limits (i.e., 2.5–3.7 V), while recording the optical transmittance through a FOEWS. The sensor's baseline (i.e., transmittance at 0 % SOC) differed between the various batteries due to variation in the contact area, optical fiber coupling and cladding thickness. To compare the results, the sensors' sensitivities were determined using the following expression, [transmittance at 100 % SOC – transmittance at 0 % SOC)/ transmittance at 0 % SOC] and were correlated to the FOEWSs' transmittance loss in glycerol (see Figure 25).

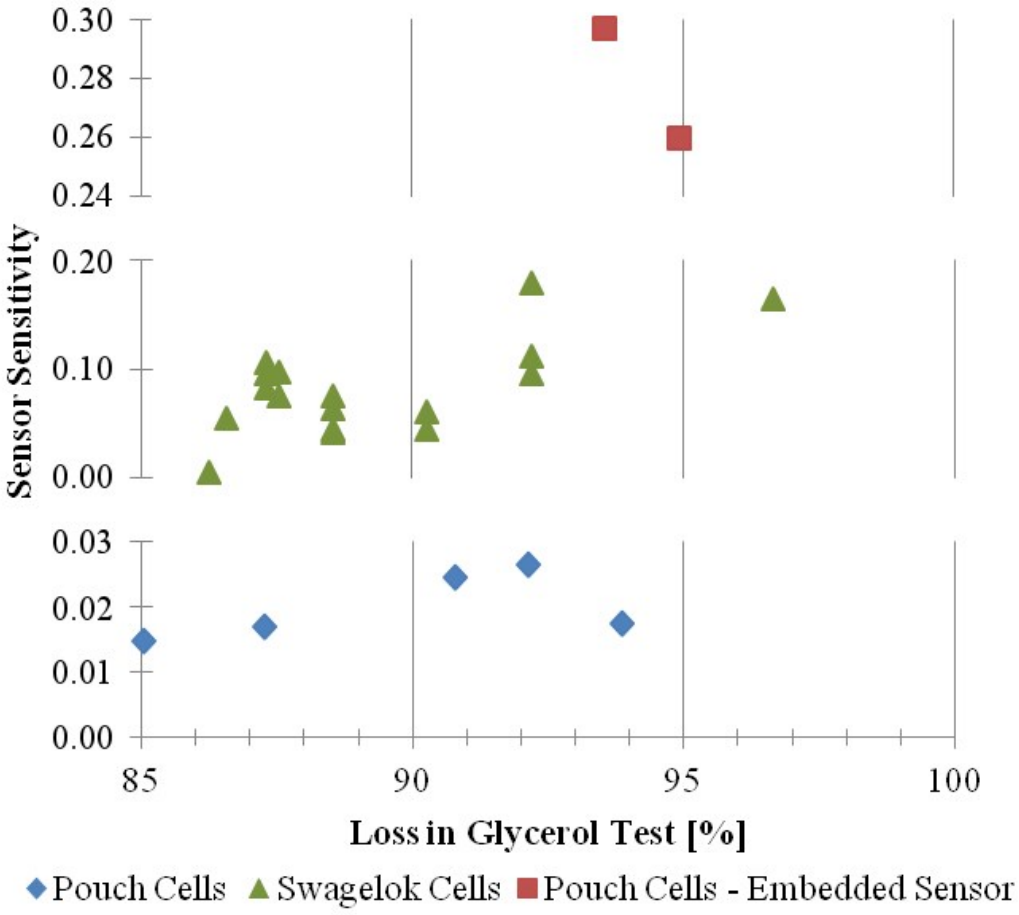

Figure 25: Fiber optic evanescent wave sensor sensitivity in relation to the loss in 100 % glycerol. The presented results include all three configurations (swagelok cells (Figure 24a), pouch cells (Figure 24b) and sensors embedded within the graphite electrode in a pouch cell (Figure 24c)) [18]. Copyright (2017) American Chemical Society.

Based on the results in Figure 25, the Swagelok and pouch cells with and without embedded sensors demonstrated the highest sensitivity when the sensor transmittance loss in glycerol was about 92.0, 93.5 and 92.0 %, respectively. However, since only two pouch cells with embedded sensors were tested, we conclude that FOEWS with about 92.0 % loss in glycerol achieve the

highest sensitivity in a LIB on the basis of the other two configurations. In the same figure a scatter was observed in the Swagelok cell results, which can be attributed to the variation in pressure between the cells, since the depth of the trench is dependent on the pressure applied during assembly. The deeper the trench, the larger the interaction between the FOEWS and the graphite electrode, increasing the sensitivity of the sensor. This also explains the reason why the sensors in the Swagelok cells had larger sensitivity than the pouch cells as seen by the trench size difference in Figure 22. Embedding the sensor completely within the graphite electrode as illustrated in Figure 24c within a pouch cell resulted in the highest sensitivity, which can also be seen when comparing the full cycle transmittance of all three configurations (swagelok cell, pouch cell and pouch cell with an embedded FOEWS) (see Figure 26). The relative sensor signal change was determined by shifting all transmittance measurements to start at 0 at 0 % SOC and dividing the transmittance measurements by the initial transmittance at 0 % SOC as a point of reference to permit comparison between all three configurations.

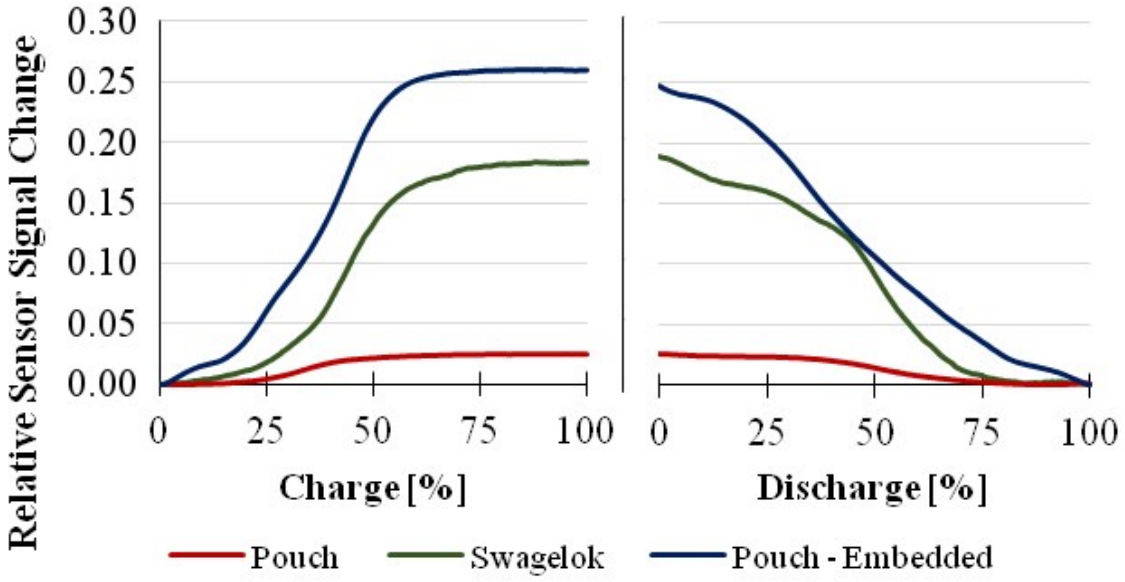

Figure 26: Full charge and discharge transmittance for all three configurations (swagelok, pouch and pouch with an embedded sensor). Relative sensor signal change is equal to $[(T-T_o)/T_o]$, where *T* is the transmittance and T_o is the transmittance at 0% SOC [18]. Copyright (2017) American Chemical Society.

The transmittance through the FOEWS was observed to increase when the battery is charged in all three configurations following a similar trend. The slope in the charging signal significantly decreased as the battery approached 62.5 % SOC. This may indicate the limit of interaction of the sensor with the graphite particles, due to the sensing depth [89] or the decrease in lithiation activity in the local region [25] of the FOEWS. During discharge, the transmittance was observed to decrease more steadily as lithium deintercalated, indicating a steady change in the graphite particles surrounding the FOEWS during discharge unlike charging. To investigate this further, a method to embed multiple fibers within one graphite electrode in different

locations/depths is required for complete characterization of the graphite anode. Nevertheless, the current observed trend in the signal from an embedded optical fiber within a pouch cell can be used to estimate SOC based on the optical changes within a LIB. Further development in the embedding process of FOEWS will allow the use of such sensors in cylindrical cells and further promote their commercial use in many more applications.

4.4 Conclusions

The process of fabricating fiber optic evanescent wave sensors and integration of the sensors into Swagelok and pouch battery cells has been presented. A method for characterization to achieve higher sensitivity and higher efficiency in the battery performance has been developed. The experimental results demonstrate that a buffered hydrofluoric solution of 40 wt % ammonium fluoride (NH_4F) and 49 wt % hydrofluoric solution (6:1) is superior to a solution of 49 wt % hydrofluoric acid for the cladding etching process during sensor fabrication. A qualitative analysis of the graphite electrodes used in both Swagelok and pouch cells demonstrate the significant reduction in applied pressure when using pouch cells allowing for batteries with longer life. The quantitative analysis of the first cycle efficiency of the two battery configurations demonstrate the superiority of using a pouch cell with an initial applied pressure of about 4 psi. The fiber optic sensor was tested within batteries and found to have highest sensitivity when the transmittance loss in 100 % glycerol approached 92 %. It was also demonstrated that increasing the area that the FOEWS contacts the graphite electrodes by embedding the sensor enhanced its sensitivity.

5. Modeling the Photonic Interaction of Graphite With a Fiber Optic Sensor Within a Lithium-ion Battery

This chapter is based on a manuscript pending submission

A. Ghannoum, J. R. Godin, and P. Nieva, "Modeling the Photonic interaction of Graphite with a Fiber Optic Sensor within a Lithium-ion Battery." Unpublished manuscript

5.1 Introduction

The developments in the implementation of fiber optic evanescent wave sensing within lithium ion batteries (LIBs) presented in the previous two chapters, define the baseline for comparison between experimental signals and theoretically simulated signals. This provides a fundamental approach to understanding the optical signal produced by the fiber optic evanescent wave sensor (FOEWS).

This chapter presents the development of a coupled model to simulate a FOEWS embedded into a graphite electrode within a LIB. The model couples a developed graphite optical model with a LIB transport model and a previously developed FOEWS analytical model to simulate the FOEWS optical signal during LIB operation. The developed graphite optical model is also used to estimate the reflectance of lithiated graphite electrodes extracted from coin cells. An enhanced glycerol test is also introduced in this chapter, and combined with the FOEWS's analytical optical model to approximate the sensor cladding thickness after etching. Finally, the relation

between applied current and the FOEWS signal is investigated and explained using the coupled model.

5.2 Experimental

5.2.1 Materials

Buffered oxide (JT5569-3, VWR) was used to etch the optical fiber cladding. Glycerol (GX0185-2, EMD Millipore) was used to test the fabricated sensors. The fabricated battery consisted of graphite and $LiFePO_4$ electrodes (MTI Corp.), trilayer polypropylene-polyethylene-polypropylene membrane (Celgard®) as a separator, mixture of ethylene carbonate and dimethyl carbonate 1:1 (vol %) 1 M lithium hexafluorophosphate (746711, Sigma-Aldrich) as an electrolyte. A graphite slurry was made using graphite (43209, Alfa Aesar), poly(vinylidene fluoride) (182702, Sigma-Aldrich), carbon black (Lib-SuperP, MTI Corp.) and N-methyl-2-pyrrolidone (328634, Sigma-Aldrich). To achieve a hermitic seal ethylene-vinyl acetate polymer based hot melt adhesive (PLIB-HMA8, MTI Corp.) was used around the fabricated FOEWS.

5.2.2 Preparation of Fiber Optic Sensor

A step index multi-mode optical fiber (AFS105/125Y, Thorlabs) was etched in a polypropylene beaker (1201-0250, NALGENE) containing buffered oxide etchant[1], [17]. The etched optical fiber was then connecterized using SMA-905 stainless alloy connectors (F193336, FIS) and the sensing region was then tested using glycerol. Hot melt adhesives were attached about 2.5 cm from the center of the sensing region to align with the pouch cell edges during the fabrication of the pouch cell described in the next section.

5.2.3 Preparation of Pouch Cell with an Embedded Fiber Optic Sensor

The pouch cell was prepared as in chapter 4 (section 4.2.2, [18]), graphite and $LiFePO_4$ electrodes were cut into 2 × 3 cm rectangles with the active material covering a 2 × 2 cm square area and the foil (copper for graphite and aluminum for $LiFePO_4$) exposed in a 1 × 2 cm area. Current collectors were attached by spot-welding to the remaining foil section on the electrodes, nickel tabs (PLiB-NTA3, MTI Corp.) were used with copper foil (i.e., for graphite electrodes) and aluminum tabs (PLiB-ATC4, MTI Corp.) were used with aluminum foil (i.e., for $LiFePO_4$ electrodes). A graphite slurry (74.0 % N-methyl-2-pyrolidone, 22.1 % graphite, 2.60 % poly(vinylidene fluoride) and 1.30 % carbon black) was prepared and used to embed the prepared fiber optic sensor onto the graphite electrode and left to dry in a fume hood. Laminated aluminum (alf-100-210, MTI Corp.) was shaped to fit the electrodes with a trilayer polypropylene-polyethylene-polypropylene separator between them. The laminated aluminum containing the battery's solid components was sealed along three edges using a heat sealer (MSK-140, MTI Corp.). After this partial seal, electrolyte was injected in a glove box prior to sealing the fourth edge using a Compact Vacuum Sealer (MSK-155A, MTI Corp.). The prepared pouch cell was placed in a 3-D printed casing (see Figure 18d) with an initial applied pressure of 4 psi and positioned for testing.

5.2.4 Battery Cycling and Fiber Optic Sensor Transmittance Acquisition

The pouch cell was connected to a programmable battery cycler (BST8-WA, MTI Corp.) while the fiber optic sensor was connected to a narrow band LED (850 nm) at one end and a photodiode at the other end specific to the same narrow band of the LED as described elsewhere

[17]. To ensure that the battery reached a state-of-charge (SOC) of 0 and 100 %, a two-step discharge and charge protocol was used derived from a method presented in [90]. During charging, a constant current was applied until the battery reached its upper voltage limit of 3.7 V; then a constant voltage of 3.7 V was applied until the current reached 10 % of the initial applied current. The battery was then allowed to rest for 20 min followed by a constant current discharge (first step in discharge) until it reached 2.5 V (lower limit) followed by a 30 min rest to allow the redistribution of the lithium ions within the electrode particles. The second step in the discharge was then initiated using 10% of the initial discharge current to ensure 0 % SOC was reached.

5.2.5 Lithiated Graphite Diffuse Reflectance Spectroscopy

The reflectance of extracted graphite electrode samples from coin cells was measured using a fiber-optic spectrometer (USB4000, Ocean Optics) and a tungsten halogen light source (LS-1, Ocean Optics). The reflectance probe (QR200-7-VIS-NIR, Ocean Optics) was set up at 45^{o} in a customized apparatus inside a glove box, as illustrated and described in Section 3.2.2 [1]. The coin cells consisted of a lithium metal anode, graphite as a cathode (same graphite electrode used in the pouch cells) and the same separator used in the pouch cells. The coin cells were discharged to attain graphite electrodes with 0, 20, 40, 60, 80 and 100 % SOC.

5.3 Modeling

5.3.1 Transport Model

The lithiation of graphite within a lithium ion battery was modeled in one-dimensional space using COMSOL. The transport model governing equations were based on the battery module in

COMSOL [51], [53], described in Chapter 1 (section 1.4). The schematic representation of all layers considered in this model is shown in Figure 27; it consists of two electrodes, graphite and $LiFePO_4$, separated by a separator in a medium of electrolyte.

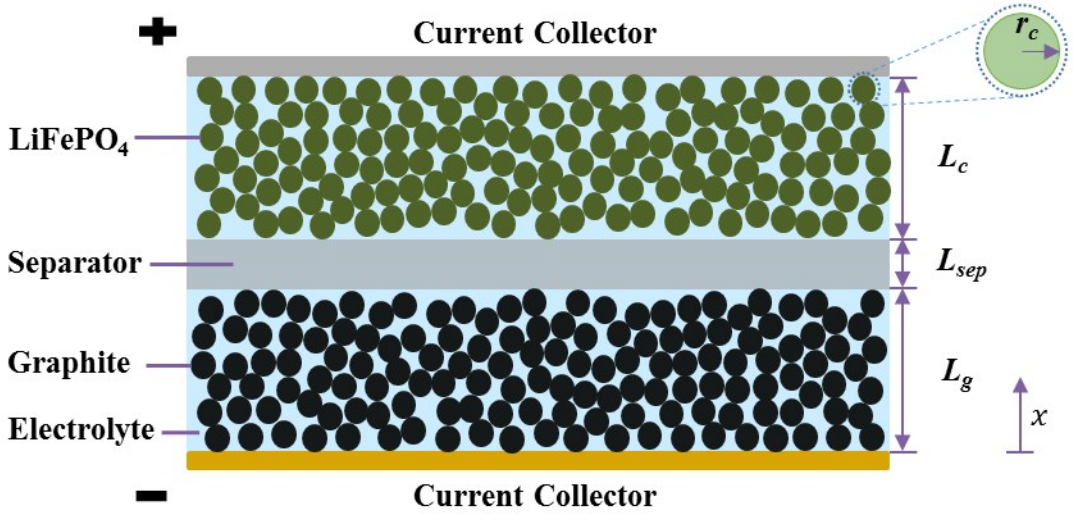

Figure 27: Schematic representation of the layers of the lithium ion battery modeled in the transport model. The current collectors are conductive material, while the electrodes consist of spherical particles representing the active material.

The model parameters were based on both experimental characterization of the battery components and literature values (Table 2, please refer to the abbreviation list for a complete description of the listed parameters). The maximum lithium concentration was measured using the maximum reversible capacity achieved in a half-cell for both electrodes. The equilibrium potential of graphite from 0 to 100 % SOC was based on open circuit voltage measurements taken within a charge at C/50 in a half-cell. The half-cell was rested for an hour before every open circuit voltage measurement. The equilibrium potential of $LiFePO_4$ was also measured in

the same way but an applied current of C/40 was used. The thickness of the separator and both the electrodes were measured using cross-sectional SEM micrographs. The spherical particle radius for the graphite electrode used in the transport model was derived using the average volume of the graphite particles. The volume of a graphite particle was calculated assuming an ellipsoidal shape, 2 of the axes were measured using SEM micrographs and the third axis (i.e. thickness) of the ellipsoid was assumed to be 5 μm based on cross-sectional SEM micrographs. The spherical radius of the $LiFePO_4$ particles used in the transport model was derived from the calculated average area of the $LiFePO_4$ particles. This area was calculated assuming an ellipse with dimensions measured using SEM micrographs. The volume fractions were estimated based on an analysis of the areas of voids versus solid materials found in SEM micrographs of graphite and $LiFePO_4$ electrodes. The diffusion coefficients and reaction rate constants of the electrodes were fitted to match the simulated voltage profiles with the experimental results. The remaining parameters were obtained from various literature references as indicated in Table 2. The solid phase parameters are separated from the electrolyte/separator parameters to distinguish between the volume fraction of the electrolyte and the solid electrodes. The model was used to estimate the average lithium concentration in the particles to model the optical properties of the graphite particles during battery cycling as discussed in the next section.

Table 2: Lithium transport model parameters with values extracted from experimental characterization of the battery and referenced literature. a: assumed e: estimated f: fitted m: measured

Solid phase parameters	Graphite (g)	$LiFePO_4$ (c)	Units
Maximum Li concentration	$c_{s,max,g}$ = 30944[m]	$c_{s,max,c}$ = 22820[m]	[mol m^{-3}]
Diffusion coefficient	$D_{s,g}$ = 3.9×10^{-14}[f]	$D_{s,c}$ = 3.2×10^{-13}[f]	[m^2 s^{-1}]
Anodic reaction rate constant	$k_{a,g}$= 2×10^{-11}[f]	$k_{a,c}$= 2×10^{-11}[f]	[m s^{-1}]
Cathodic reaction rate constant	$k_{c,g}$= 2×10^{-11}[f]	$k_{c,c}$= 2×10^{-11}[f]	[m s^{-1}]
Thickness	L_g= 89.7×10^{-6}[m]	L_c= 90.0×10^{-6}[m]	[m]
Particle radius	r_g= 10.75×10^{-6}[a]	r_c= 0.2165×10^{-6}[a]	[m]
Temperature	T = 298		[K]
Charge transfer coefficient	α_i = 0.5[a] [91]		
Volume fraction	$\epsilon_{s,g}$ = 0.433[e]	$\epsilon_{s,c}$ = 0.305[e]	
Conductivity	σ_g = 100 [78] [79]	σ_c = 11.8 [93]	[S m^{-1}]
Equilibrium potentials	$\Delta\phi_{eq,g}(SOC)$[m]	$\Delta\phi_{eq,c}(SOC)$[m]	[V]
Electrolyte/Separator parameters	1 M $LiPF_6$, 1:1 EC:DMC		Units
Diffusion coefficient	D = 1.38×10^{-9} [94]		[m^2 s^{-1}]
Thickness	L_{sep} = 28.63×10^{-6}[,m]		[m]
Cationic transport number	t_+ = 0.21 [95]		
Volume fraction (in electrode)	ϵ_g = 0.500[e]	ϵ_c = 0.593[e]	
Conductivity	$\sigma(c_{salt})$ [96]		[S m^{-1}]

5.3.2 Graphite Optical Model

Since graphite is anisotropic, its reflectance at 850 nm is much larger when photons are directed perpendicularly to its carbon layers [97]. The bulk diffuse reflectance of graphite electrodes increases as the amount of inserted lithium increases [16][41]. Chemically (not electrochemically) prepared lithiated graphite also exhibit a significant increase in reflectivity as the amount of lithium is increased [39]. The maximum ratio of lithium to carbon in lithiated graphite is one to six (LiC_6). The real (ε_1) and imaginary (ε_2) components of the dielectric constant that defines the optical properties of LiC_6 at 850 nm normal to the graphite layers, are derived to be -8.3723 and 5.7354, respectively [98]. The values of ε_1 and ε_2 for graphite under "near-normal" incidence at 850 nm have been derived to be 8.8212 and 4.5290 [97].

Using the two limits for the dielectric constants specified above at normal incidence, a simple model for the optical properties was developed. The model assumes a linear change in the dielectric constants as graphite transitions to LiC_6 and defined as,

$$\varepsilon_1 = -0.17193\ (SOL_g) + 8.8212 \tag{16}$$

$$\varepsilon_2 = 0.012065\ (SOL_g) + 4.5290 \tag{17}$$

Where SOL_g is the state of lithiation with values ranging from 0 (graphite) to 100 (LiC_6). Once ε_1 and ε_2 are known, the refractive index (n) and extinction coefficient (k) of lithiated graphite is obtained using the following relationships [99]:

$$n = \sqrt{\frac{\sqrt{{\varepsilon_1}^2 + {\varepsilon_2}^2} + \varepsilon_1}{2}} \tag{18}$$

$$k = \sqrt{\frac{\sqrt{{\varepsilon_1}^2 + {\varepsilon_2}^2} - \varepsilon_1}{2}} \tag{19}$$

The reflectivity (R) of a specular surface of graphite at normal incidence can be determined using the following expression with the calculated n and k values [99].

$$R = \frac{(n-1)^2 + k^2}{(n+1)^2 + k^2} \tag{20}$$

Using only the normal incidence values in this model is an approximation. The normal incidence reflectivity is about 19 times larger than reflectivity parallel to the graphite layers when calculated using dielectric constants obtained from [100] at 850 nm. This indicates that the developed optical model may be used to determine the theoretical maximum values that can be obtained from a graphite electrode sample.

The calculated refractive index and extinction coefficient were used in determining the fiber optic sensor transmittance using an analytical model developed by J. R. Godin [101]. The following section demonstrates the use of the analytical model to estimate the cladding thickness of the etched FOEWS and its use in simulating the transmittance of FOEWS embedded within a LIB.

5.3.3 Fiber Optic Sensor Model

The previously developed analytical model by J. R. Godin is based on the transfer matrix method and models the behaviour of the fiber optic sensor interacting with any material with known optical constants [101]. This model was utilized to both estimate the thickness of the cladding after etching the fiber optic sensor and to model the transmittance of the embedded FOEWS.

The sensing length was initially determined after etching, using a conventional microscope, and substituted into the fiber optic sensor model. The sensor was then connected to an optical interrogator to obtain an initial transmittance reading. A comprehensive glycerol test is performed, which entails applying glycerol on the sensing region, initially covering a small region with a measured length (i.e., 5 – 10 mm) and increasing the region covered by glycerol in intervals (i.e., 2.5 – 5 mm) while recording the change in transmittance (see Figure 28). The fiber optic sensor model was then used to estimate the optical fiber cladding thickness (see Figure 29). The specific comprehensive glycerol test presented in Figure 29, was used to approximate the cladding thickness to be 1.17 μm, which is relatively small considering a core diameter of 105 μm. The cladding thickness is an essential input parameter to the analytical model when simulating the embedded FOEWS.

The n and k values used in the analytical model to simulate the embedded FOEWS were obtained using equations 15 – 18. The graphite's state of lithiation (SOL_g) used in equations 15 and 16 was set to be equivalent to the average surface lithium concentration in the graphite particles within a LIB over the maximum possible concentration using the transport model

presented in section 5.3.1. The electrolyte was assumed to have no effect on the sensor [1] and the sensing region within the electrode was assumed to be in contact with graphite particles only. Figure 30 summarizes how the fiber optic model is combined with the graphite optical model and transport model to obtain simulated optical fiber transmittance as a function of SOL_g.

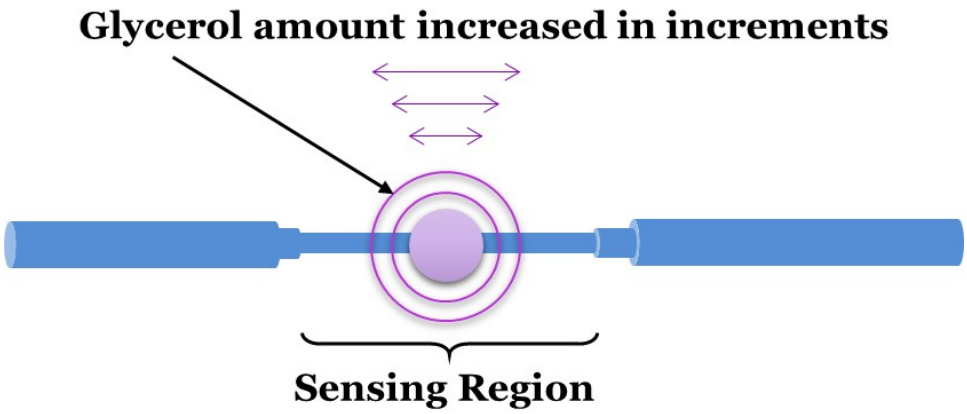

Figure 28: Schematic representation of the comprehensive glycerol test. Glycerol is injected onto the sensing region to cover 5 – 10 mm and then increased by 2.5 – 5 mm increments, while recording the transmittance through the fiber optic sensor.

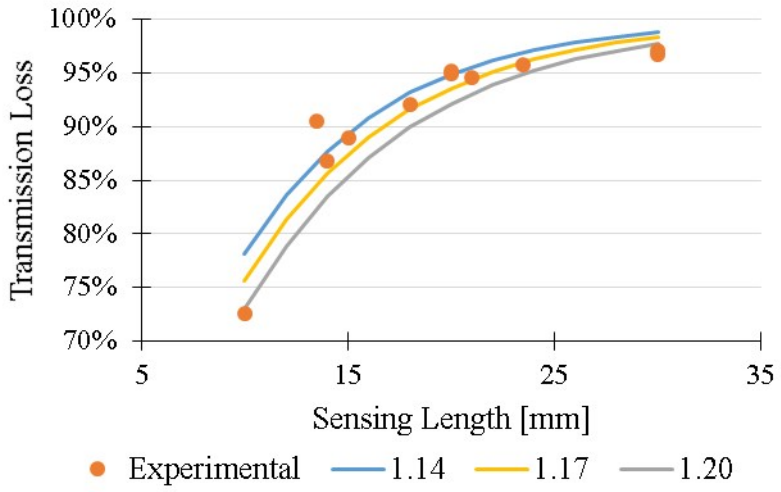

Figure 29: Comprehensive glycerol test results compared to fiber optic sensor transmittance results as the cladding was increased from 1.14 μm to 1.20 μm.

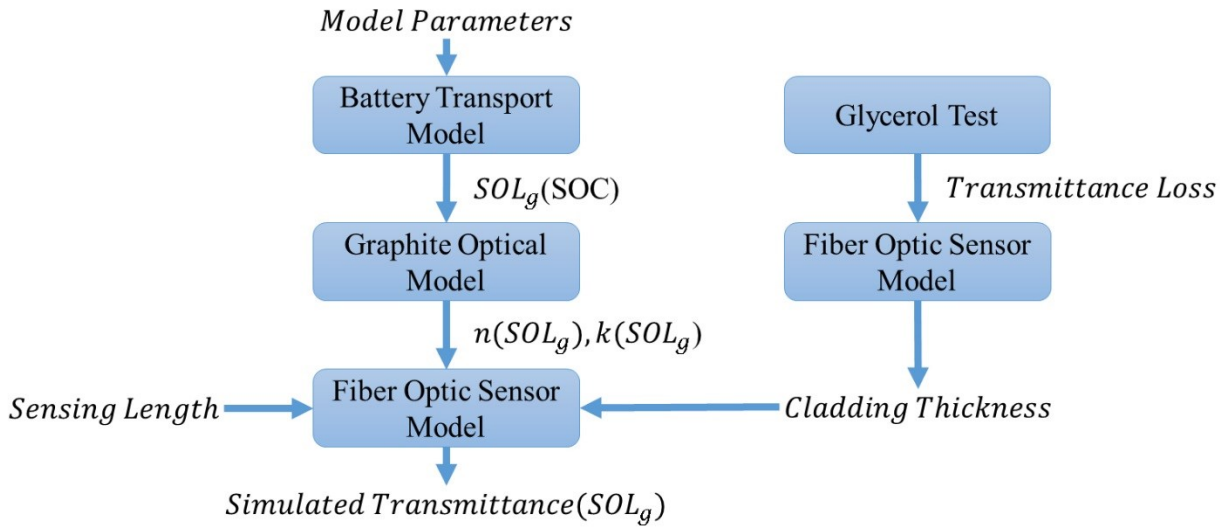

Figure 30: Flowchart outlining how the battery transport model, graphite optical model and fiber optic sensor model are coupled to obtain simulated transmittance as a function of graphite's state of lithiation

5.4 Results and Discussion

5.4.1 Lithiated Graphite Diffuse Reflectance Spectroscopy

The reflectance of the graphite electrodes used in the fabricated pouch cells with embedded fiber optic sensors was measured to evaluate the ability of the developed graphite optical model to estimate reflectance. A total of 11 graphite electrodes, lithiated to values ranging from 0 to 100 % SOL_g, were tested in two trials and compared with the calculated reflectance at 850 nm based on the developed graphite optical model (equations 15 – 19) as seen in Figure 31. The two trials demonstrate the same general trend with a slight variation, which was caused by the random arrangement of the graphite particles (anisotropic material) on the electrode surface and alignment with the reflectance probe.

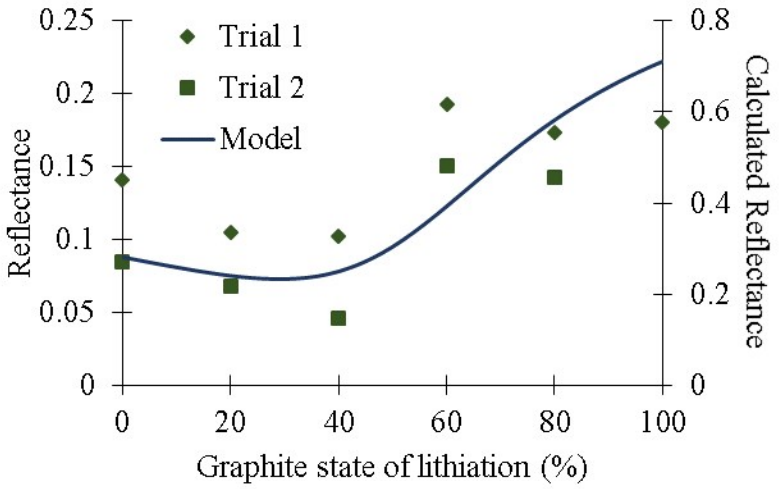

Figure 31: Comparison of the calculated reflectance of graphite based on the developed model with two trials of reflectance measurements (at 850 nm) of graphite electrodes extracted from 11 coin cells.

Comparing the experimental trials to the calculated reflectance indicates that the model was capable of producing the same general trend. A slight variation in the trend was observed at 80 and 100 % lithiation when comparing the experimental data to the model. The calculated reflectance at 100 % lithiation assumes a specular surface [99] and uses values derived from a measurement taken at a position normal to graphite layers [98]. Comparing the measured and calculated reflectance at 100 % SOL_g indicates that the graphite particles in the electrodes do not form a specular surface and were not perfectly aligned normal to the reflectance probe as expected, achieving only 25 % of the calculated reflectance. The downward shift in the data between trials 1 and 2 corresponds to a decrease in the intensity of the reflectance, which may indicate a small shift in the positioning of the reflectance probe away from the sample.

5.4.2 Coupled Model vs. Embedded Fiber Optic Sensor

A pouch cell with an embedded fiber optic sensor with a cladding thickness of 1.28 μm (94.9 % transmittance loss in 100 % glycerol and a sensing length of 28.5 mm) was cycled from 0 to 100 % SOC, based on the voltage limits of 2.5 to 3.7 V as described in section 5.2.4. The battery capacity was determined based on the applied current and time (i.e., coulomb counting) and then compared with the observed optical transmittance through the embedded fiber optic sensor as seen in Figure 32.

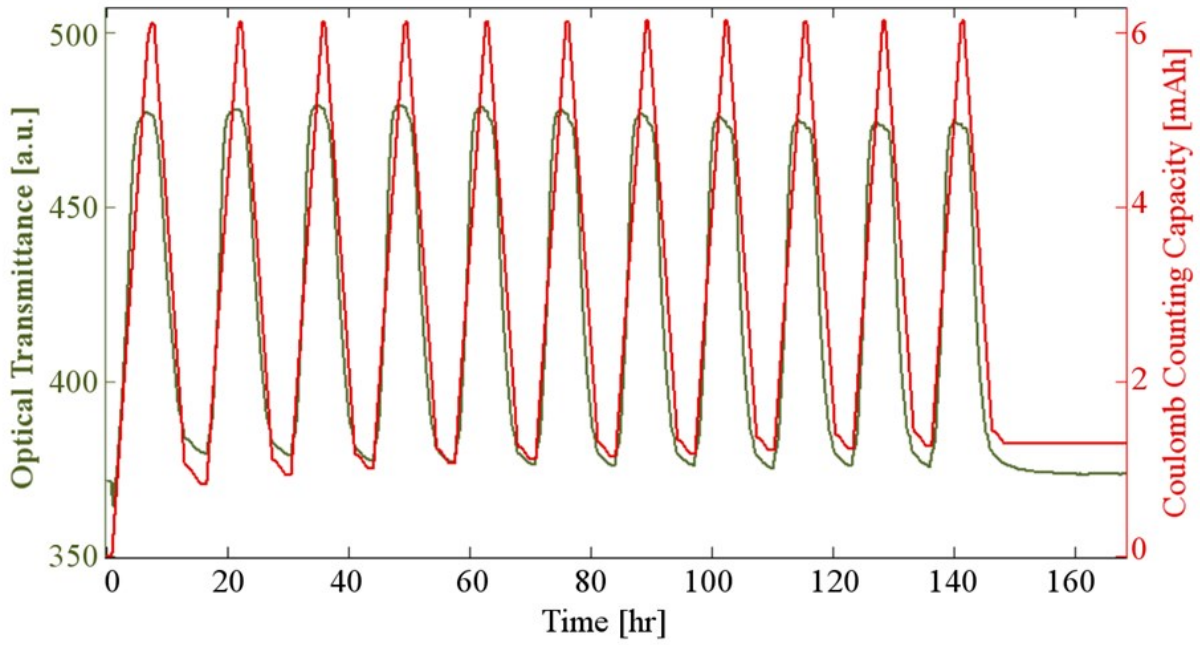

Figure 32: The optical transmittance of an embedded fiber optic evanescent wave sensor (green) during the first 11 cycles (0 to 100 % SOC) of a pouch cell and the coulomb counting capacity (red) based on the applied current required to cycle between 2.5 and 3.7 V.

The optical change in the battery was observed to follow the capacity changes closely. The irreversible capacity loss during the first cycle seems to affect the extent that the transmittance drops during the first discharge (i.e. it does not drop down to the initial value). The charging process of the battery is a two-step process. A constant current is initially applied until the battery reaches 3.7 V and then a constant voltage is applied until the current reaches a tenth of the initial applied current. During the first step, the transmittance undergoes a steady increase with varying slopes; the slope of the transmittance during a charge exhibits 3 distinct peaks (see Figure 33).

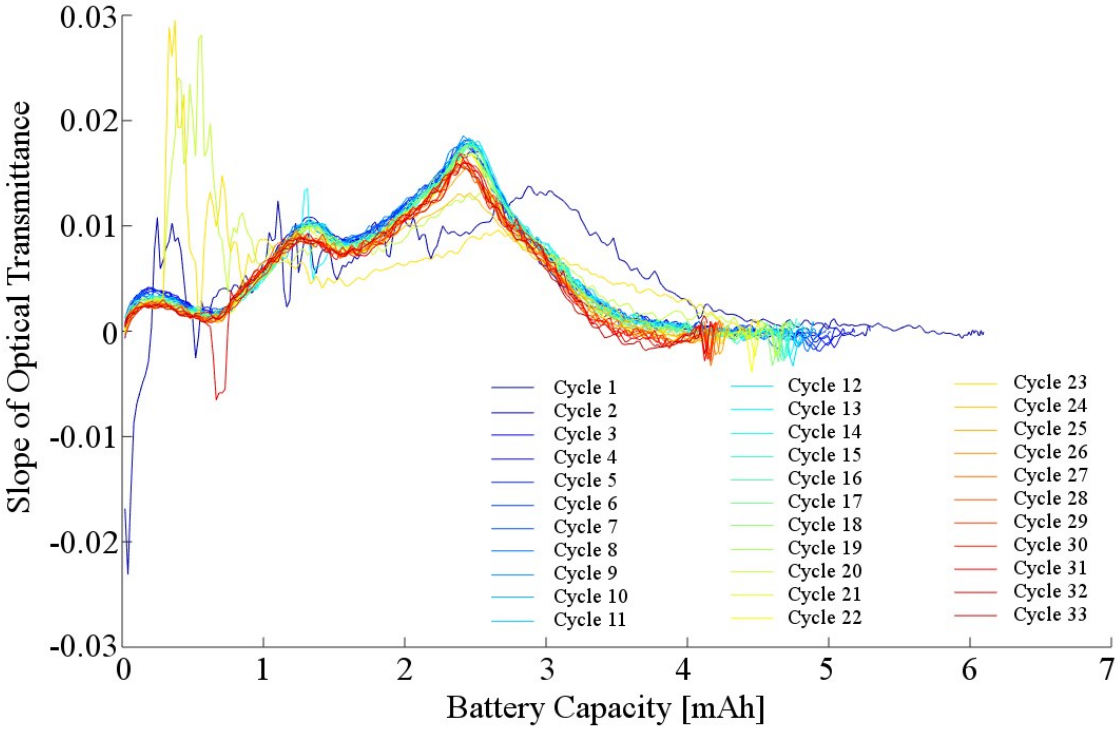

Figure 33: The slope of the optical transmittance of an embedded fiber optic evanescent wave sensor during the first 33 charges (0 to 100 % SOC) of a pouch cell overlapped for comparison by plotting them against the battery's capacity.

Based on the capacity in the second cycle, the highest repeated slope peak occurs when the battery reaches about 45 % SOC. Considering the graphite state of lithiation (SOL_g) as a point of reference, the highest slope occurs at about 19 % SOL_g. The first and second peaks occur at about 1.6 and 10 % SOL_g, respectively. Based on potential-capacity curves for graphite vs. Li/Li^+ (see Figure 5), all three peaks seem to occur near the transition zones of the graphite lithiation stages IV, III and II. Hence, analyzing the slope of transmittance during cycling can be used in an algorithm to determine the SOL_g. Three of the cycles in the first 33 cycles did not

follow the three consecutive peak trend, cycles 1, 20 and 23, which have been found to be cycles in which capacity fade occurred. This demonstrates the ability of the FOEWS to predict capacity fade prior to its occurrence as seen in Figure 34. The capacity fade in the first cycle is linked to the formation of the SEI layer. While the cause of capacity fade in cycles 20 and 23 are not identified. Comparing the change in experimental transmittance (i.e. amplitude) during the first 33 cycles, a relationship between amplitude and achievable capacity is observed. A decrease in amplitude is correlated to a decrease in lithiation activity; this indicates that the amplitude can be used to determine the battery's state of health (SOH) over full cycles. In terms of determining SOH prior to completing a full cycle, the slope peaks plotted in Figure 33 do decrease in magnitude as capacity fades. This change in the slope can be further analyzed and used in an algorithm to determine the SOH of a LIB.

In the second charging step (i.e., when the charging voltage is constant) the optical transmittance was observed to generally stop increasing and instead, it decreases slightly. A decrease in the applied current causes a decrease in the lithiation process. This allows for lithium ion diffusion within the graphite particles to dominate, which could be the cause of a slight decrease in the optical transmittance during constant voltage charging.

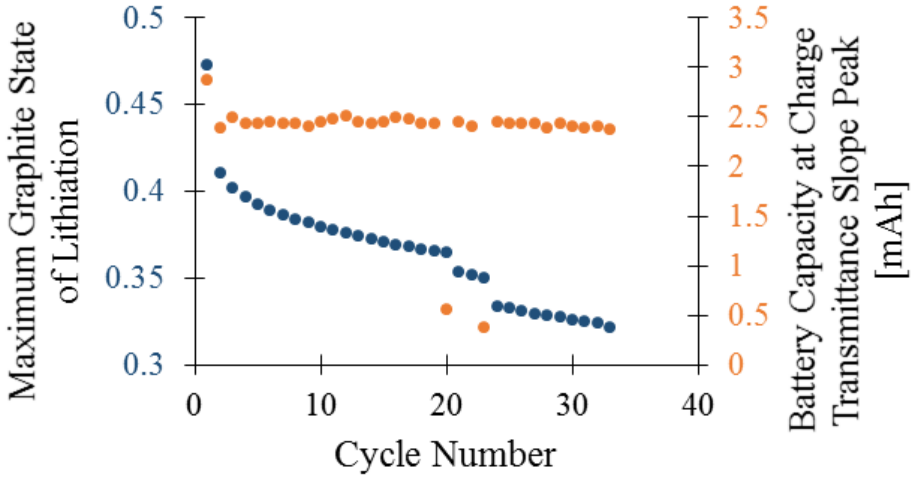

Figure 34: Experimental results demonstrating the ability of the fiber optic sensor to predict significant capacity fade in the cycle before the capacity fade occurs. The maximum graphite state of lithiation (SOL_g) achieved during a full charge (0 to 100 % SOC) of a pouch cell is plotted (blue) over 33 cycles and the corresponding recorded capacity at the maximum peak in the slope of the transmittance from Figure 33.

To demonstrate this further, a full cycle was completed with 1 hr interval charges using an applied current of C/16 and 2 hour rests between every step as seen in Figure 35. During the charging process a slight drop in transmittance is observed during the start of every rest period, which was more prominent as SOC increased. At lower capacities this effect seems to be minor, which can be explained by the lower concentration gradient within the graphite particles causing slower or minor diffusion of the lithium ions. During the discharging process, the optical transmittance increased at the beginning of every rest period. The magnitude that the optical transmittance increased during the rest periods decreased significantly as the SOC decreased.

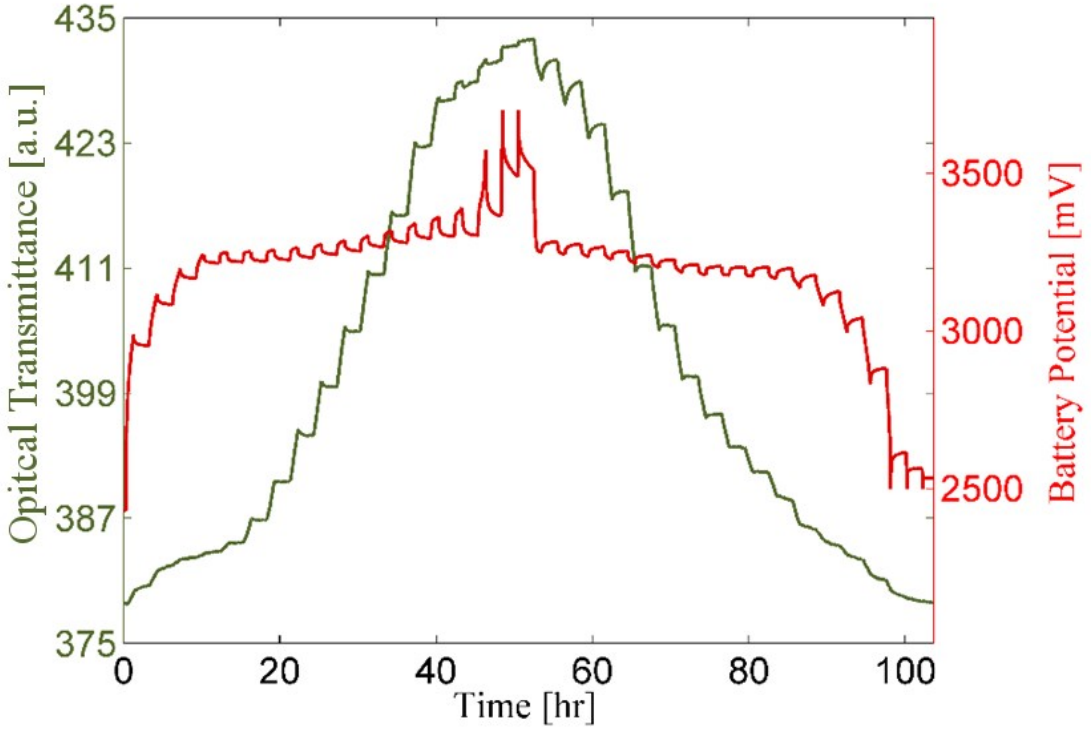

Figure 35: Fiber optic sensor transmittance and battery potential during a full cycle. Current was applied over 1hr intervals with 2hrs rests between every interval and the voltage limits were set to 3.7 V during charging and 2.5 V during discharging. Current of C/16 was used.

In addition, the magnitudes of change in the optical transmittance during the discharging rest periods were observed to be much larger than during the rests in the charging process. This supports the notion that the concentration of lithium ions at the graphite particle surface significantly affects the optical transmittance [1]. The FOEWS has a specific penetration depth dependent on the wavelength of the transmitting light. As the distance from the fiber increases, the intensity of the penetrated wave decreases exponentially [102]. For this reason, the

concentrations of intercalated lithium ions at the surface of the graphite particles obtained using the transport model were used in the developed linear graphite optical model.

The optical transmittance during the first, second, fifteenth, twentieth and twenty-fifth charge were plotted for comparison with the simulated transmittance as they represented the general trends observed during the first 33 charges (see Figure 36).

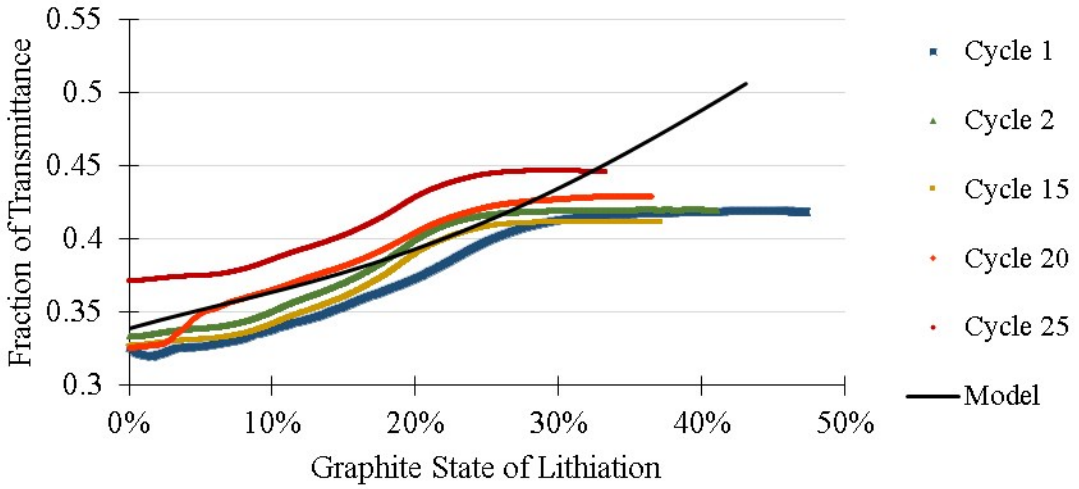

Figure 36: Comparison of the fiber optic sensor transmittance model output to the measured transmittance from a pouch cell during the 1st, 2nd, 15th, 20th and 25th charge; where variation can be observed as capacity fade increases.

The initial transmittance at 0 % SOL_g is about 3 % lower in the experimental data (i.e., cycle 1) compared with the model results. This discrepancy may be caused by two environmental factors, i) the coupling of the light source to the optical fiber and ii) the external applied pressure on the pouch cell. The optical transmittance obtained during cycling is divided by the transmittance of the FOEWS when tested in air, prior to pouch cell assembly. This may cause an

offset since the coupling of the light into the fiber during the test in air may not be equivalent to the coupling after pouch cell assembly. The second factor (i.e., applied pressure) affects the contact between the graphite particles and the optical fiber [18], which could decrease the overall transmittance. The 3% deviation in the experimental signal compared to the simulated signal remains until the battery reaches a SOL_g of about 30 %, where the experimental signal increases at a lower rate, while the simulated transmittance continues to increase causing a large deviation.

The general trend of increasing transmittance as SOL_g increases is evident in both the experimental and modeling results. The significant variation occurs at higher SOL_g, where the rate of increase in the actual transmittance decreases significantly, while the simulated transmittance continues to increase with minor slope changes. This variation indicates that the diffusion of lithium ions in the simulations is much smoother than the actual graphite around the FOEWS. Reducing the current, increases the achievable capacity; by changing the lithiation dynamics, allowing more time for lithium ion diffusion within the solid graphite particles. In other words, changing the applied current directly affects the optical transmittance as seen in Figure 37, which shows the normalized transmittance of a FOEWS with a cladding thickness of 1.28 μm embedded in a pouch cell that was charged from 0 to 100 % SOC using three different rates, C/5, C/8 and C/16. It can be observed that a reduction in the applied current causes a generally smoother increase in transmittance. When an applied current of C/5 was used, a peak in the optical transmittance was observed as the pouch cell approached 100 % SOC, which may indicate the saturation point at the surface of the graphite particles around the FOEWS. To observe these phenomena in the simulated data, the current was also increased in the transport

model from 0.1 C to 1C and 2C and the results are plotted in Figure 38. To allow for comparison between the three currents, the simulated transmittance was plotted against the fraction of the full cycle, since the time periods for each cycle differed significantly. Each cycle included a full charge followed by a resting period and then a full discharge followed by a second resting period. As the current increased, the resting periods exhibited larger drops in transmittance after the full charge step. This aligns with the experimental results and demonstrates how the concentration of lithium at the surface of the particles decreases during its diffusion as the battery rests. Similarly, during the rest period after the full discharge the simulated transmittance increases due to an increase in the lithium ions at surface of the particles as they diffuse outwards (this is more visible in the 2C simulation). Experimentally this was only observed at higher SOC, since only lower currents were used to cycle the pouch cell.

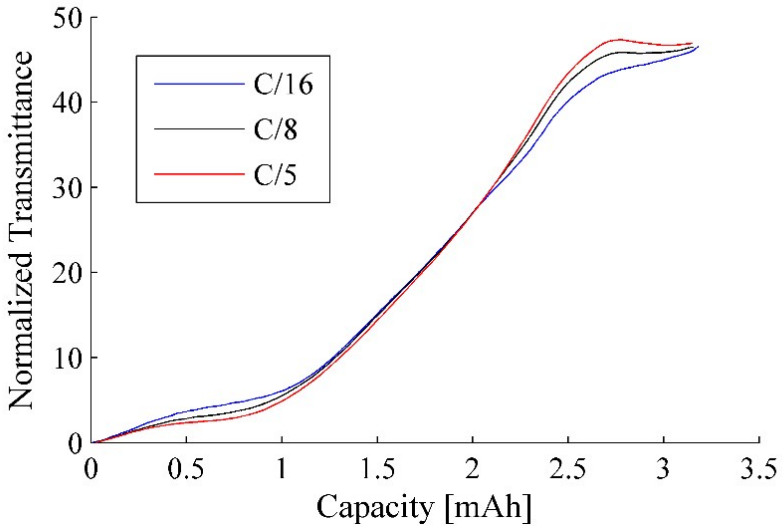

Figure 37: Normalized transmittance of a fiber optic sensor with a cladding thickness of 1.28 μm embedded in a pouch cell charged at three different rates, C/5, C/8 and C/16 from 0 to 100 % SOC.

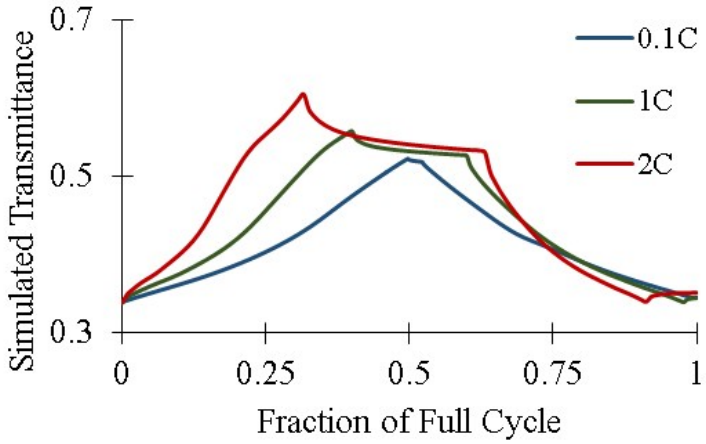

Figure 38: Simulated fiber optic sensor transmittance in a pouch cell with three different applied currents; 0.1C, 1C and 2C. The full cycle included a charging step followed by a resting period and then a discharging step followed by a second rest.

The simulated optical transmittance (see Figure 38) also demonstrated a “three” slope trend during the battery charge when a current of 2 C was used, similar to the experimental results shown in Figure 37. These results suggest that the diffusion dynamics in the graphite particles around the FOEWS may differ from the surrounding region. The observed transmittance trend is similar to simulations with higher applied current, suggesting that lithiation around the fiber may occur at a higher rate. However, this observation would require verification by other in-situ characterization methods such as neutron imaging [103], [104] to observe regions with and without a FOEWS simultaneously. In addition, elevated pressure due to the presence of the FOEWS may also compact the graphite particles beneath it, thus increasing the conductivity in the region due to the improved contact, which may cause an increase in the lithiation rate. Nevertheless, it is clear that the FOEWS signal can be correlated to the SOC of a battery but additional studies on SOC determination algorithms are needed, and optimization of the FOEWS location would further support the use of the developed sensor in commercial applications.

5.5 Conclusions

An optical model for lithiated graphite has been developed based on the normal dielectric constants of graphite and fully lithiated graphite, with the ability to approximate the reflectance, refractive index and extinction coefficient of electrochemically lithiated graphite. The optical model has been coupled with a transport model for a lithium ion battery (LIB) and an analytical optical model for fiber optic evanescent wave sensors (FOEWS) to simulate the transmittance of a FOEWS, fabricated using a multimode optical fiber with a diameter of about 105 μm and an estimated cladding thickness of 1.28 μm, embedded in a graphite electrode within a pouch LIB.

Simulations produced trends comparable with the experimental results and suggested that the lithiation rate around the FOEWS may occur at a higher rate than the rest of the graphite electrode; Additional in-situ characterization techniques may further verify this conclusion. The effect of lithium diffusion at the surface of graphite particles on the FOEWS transmittance has been observed by implementing two hours of rest at one hour intervals during the charging and discharging process of a LIB. Lithium diffusion at the surface during relaxation (i.e. rest) was observed to be most significant during the initial discharge of a fully charged LIB. Changing the applied current was found to affect the FOEWS transmittance at the extremities (i.e., near 0 and 100 % SOC) as diffusion dynamics changed. The transmittance of the FOEWS was observed over thirty three cycles and a trend with three distinct slope peaks was found during a charge from 0 to 100 % SOC. During a charge with significant capacity fade the slope of the transmittance was observed to deviate from the three distinct peaks, demonstrating an ability to predict significant capacity fade prior to its observation through a voltage limited discharge. A method to estimate the cladding thickness of the FOEWS was also developed utilizing a "comprehensive glycerol test" developed in-house and the FOEWS analytical model. Further studies on an SOC and SOH estimation algorithm for the developed FOEWS will support its commercialization and verify its ability to support management of LIBs.

6. Conclusions and Future Work

6.1 Summary and conclusions

The overall objective of this thesis is to optimize the implementation of a previously developed fiber optic evanescent wave sensor (FOEWS) inside lithium ion batteries (LIBs) to support its commercialization. In addition to developing a coupled model to simulate and enhance our understanding of the FOEWS output signal as graphite undergoes optical changes during lithiation/delithiation within LIBs to support the development of state of charge and state of health estimation algorithms.

After an introduction in Chapter 1 and background information described in Chapter 2, Chapter 3 studied the reflectance of commercial graphite electrodes composed of graphite particles, a binding agent, carbon particles, and solid electrolyte interphase, at 30, 35, 40, 45, 50, 60, 65, 70, 75 and 80 % SOC to demonstrate the dominance of graphite particles in governing the colour of commercial graphite electrodes in the studied spectra. This study was also used to determine that the maximum lithiation stage achieved in A123 commercial LIBs was stage 2 (LiC_{12}). The observed reflectance trends in the visible and infrared spectra (500 – 900 nm) were compared to pure-phase lithiated graphite materials demonstrating that graphite dominates the reflectance of graphite electrodes. It was also determined that lithiation of graphite had a more significant affect on the reflectance of photons with wavelengths ranging from 750 – 900 nm (near-infrared band) within the investigated range. Chapter 3 also presented the first in-situ fiber optic evanescent wave spectroscopy (FEWS) measurements, with wavelengths ranging from 500 – 900 nm using a modified Swagelok cell. The trend observed in the FEWS study was found to

closely follow the reflectance of commercial graphite electrodes. The FEWS results also demonstrated a direct correlation between the transmittance through the fiber optic sensor and the SOC of the LIB. In this Chapter, it was also demonstrated that electrolyte solutions with varying salt ($LiPF_6$) concentrations had no effect on the transmittance of the fabricated FOEWS.

Chapter 4 presented the optimization of the fiber optic evanescent wave sensing system for the ultimate purpose of commercialization by focusing on three aspects. The first aspect was the cladding etching of the fiber optic evanescent wave sensor (FOEWS). Experimental results demonstrated that a buffered hydrofluoric solution of 6:1, 40 wt % ammonium fluoride (NH_4F) and 49 wt % hydrofluoric solution, was superior to a solution of 49 wt % hydrofluoric acid in producing durable sensors. Maximum sensitivity of the FOEWS within a LIB was achieved when the etched sensor produced about 92 % transmittance loss in 100 % glycerol. The second aspect of optimization was aimed at reducing capacity fade and maximizing contact between the sensor and the graphite electrode. This was achieved by designing a pouch cell that allowed an optical fiber to be embedded in the graphite electrode while maintaining a hermetic seal. The final pouch cell configuration appears to be a commercially viable with reduced weight and increased capacity. Finally, the third major development was the use of an in-house narrow band optical sensor interrogator, replacing the spectrometer, which reduced the cost of the sensing system significantly and made it more commercially viable.

Chapter 5 focused on the theoretical basis for the developed LIB sensing system to allow for deeper understanding of its performance. An optical model for graphite was presented, which assumed a linear trend between the normal dielectric constants of graphite and fully lithiated

graphite (LiC_6). The graphite model was used to estimate the reflectance, refractive index and extinction coefficient of graphite as a function of the concentration of intercalated lithium ions. Reflectance measurements of graphite electrodes used with the FOEWS were examined and found to follow a similar trend as the trend obtained using the developed graphite optical model. The optical model was then coupled with a lithium ion battery transport model and an analytical optical model for the FOEWS to simulate the transmittance signal of the fiber optic sensor. A method to estimate the cladding thickness of the FOEWS was presented, which utilized a "comprehensive glycerol test" and the FOEWS analytical optical model. Simulation results were presented for a FOEWS with an estimated cladding thickness of 1.28 μm. Trends comparable to experimental results were observed and suggested that the lithiation rate around the FOEWS may occur at a higher rate than the rest of the graphite electrode. The effect of lithium diffusion at the surface of graphite particles on the FOEWS transmittance was observed by implementing two hours of rest at one hour intervals during the charging and discharging process of a LIB. The effect of lithium diffusion on the FOEWS was observed to be most significant during the initial discharge of a fully charged LIB, which is when the lithium concentration within the graphite particles is the greatest. The FOEWS was then tested using three distinct applied currents C/5, C/8 and C/16 and found to deviate near 0 and 100 % SOC. The slope of the FOEWS transmittance over thirty three cycles was observed to have three distinct peaks during a charge from 0 to 100 % SOC. Deviation from the "three peak" trend in the slope during a charge was found to be correlated to capacity fade. This demonstrated the ability to predict significant

capacity fade during a charge prior to its observation through the capacity attained in a full discharge.

The presented work provides a direction for future work that would further promote the commercialization of the developed sensing system. Using the deeper understanding of the optical signal presented in this thesis, a battery state-of-charge and-health estimation algorithm can be developed and tested for its accuracy. Comparing the cost of this sensing system to conventional methods would demonstrate its competitiveness and support its use in various applications.

6.1 Proposed future work

The commercialization of the developed sensing system will rely heavily on its ability to estimate state of charge (SOC) and state of health (SOH). This will require rigorous testing with the sensor embedded in commercial batteries in parallel with the development of algorithms that minimize computational power and maximize accuracy in estimating SOC and SOH. A comprehensive study to compare the use of the optical sensor signal only to using voltage and current measurements with the optical signal in estimating the SOC and SOH is required to demonstrate the best possible methods for utilizing the sensing system.

In terms of further understanding the effects that the sensor may have on the current distribution within the whole LIB, an in-situ neutron imaging study of a battery equipped with a FOEWS would demonstrate the distribution of current within the graphite electrode. It is important to understand the sensor signal in relation to the rest of the graphite electrode, to allow for an optimized design. The optical fiber sensor is considered a local measurement but this

should not reduce from its value since the graphite electrode is a network of particles connected electrically. If a disturbance occurs in any part of the network, the distribution of current is also disturbed, thus altering the local lithiation process around the optical fiber sensor.

To broaden the range of applications for the FOEWS, a method to embed optical fibers within cylindrical cells is required. As in the pouch cell or any type of cell, maintaining a hermitic seal is the main challenge. This may require the design of a new cap that allows an optical fiber to pass through, ideally with minimal alterations to the standard fabrication process.

7. Letter of Copyright Permission

PERMISSION/LICENSE IS GRANTED FOR YOUR ORDER AT NO CHARGE

This type of permission/license, instead of the standard Terms & Conditions, is sent to you because no fee is being charged for your order. Please note the following:

- Permission is granted for your request in both print and electronic formats, and translations.
- If figures and/or tables were requested, they may be adapted or used in part.
- Please print this page for your records and send a copy of it to your publisher/graduate school.
- Appropriate credit for the requested material should be given as follows: "Reprinted (adapted) with permission from (COMPLETE REFERENCE CITATION). Copyright (YEAR) American Chemical Society." Insert appropriate information in place of the capitalized words.
- One-time permission is granted only for the use specified in your request. No additional uses are granted (such as derivative works or other editions). For any other uses, please submit a new request.

8. References

[1] A. Ghannoum, R. C. Norris, K. Iyer, L. Zdravkova, A. Yu, and P. Nieva, "Optical Characterization of Commercial Lithiated Graphite Battery Electrodes and in Situ Fiber Optic Evanescent Wave Spectroscopy," *ACS Appl. Mater. Interfaces*, vol. 8, no. 29, pp. 18763–18769, Jul. 2016.

[2] J. Bauman and M. Kazerani, "A Comparative Study of Fuel-Cell-Battery, Fuel-Cell-Ultracapacitor, and Fuel-Cell-Battery-Ultracapacitor Vehicles," *IEEE Trans. Veh. Technol.*, vol. 57, no. 2, pp. 760–769, Mar. 2008.

[3] Y.-J. Gu *et al.*, "Enhanced Cycling Performance and High Energy Density of LiFePO4 Based Lithium Ion Batteries," *Mater. Lett.*, vol. 61, no. 25, pp. 4700–4702, Oct. 2007.

[4] M. J. Armstrong, C. O'Dwyer, W. J. Macklin, and J. D. Holmes, "Evaluating the Performance of Nanostructured Materials as Lithium-Ion Battery Electrodes," *Nano Res.*, vol. 7, no. 1, pp. 1–62, Jan. 2014.

[5] "Tesla's Gigafactory and the Junior Miners." [Online]. Available: http://www.theenergyreport.com/pub/na/teslas-gigafactory-and-the-junior-miners. [Accessed: 15-Jan-2015].

[6] L. Lu, X. Han, J. Li, J. Hua, and M. Ouyang, "A review on the key issues for lithium-ion battery management in electric vehicles," *J. Power Sources*, vol. 226, pp. 272–288, Mar. 2013.

[7] Z. Li, J. Huang, B. Y. Liaw, and J. Zhang, "On state-of-charge determination for lithium-ion batteries," *J. Power Sources*, vol. 348, pp. 281–301, Apr. 2017.

[8] W.-Y. Chang, "The State of Charge Estimating Methods for Battery: A Review," *ISRN Appl. Math.*, vol. 2013, pp. 1–7, 2013.

[9] A. G. Hsieh *et al.*, "Electrochemical-acoustic Time of Flight: In Operando Correlation of Physical Dynamics with Battery Charge and Health," *Energy Environ. Sci.*, vol. 8, no. 5, pp. 1569–1577, 2015.

[10] G. Davies *et al.*, "State of Charge and State of Health Estimation Using Electrochemical Acoustic Time of Flight Analysis," *J. Electrochem. Soc.*, vol. 164, no. 12, pp. A2746–A2755, Jan. 2017.

[11] L. W. Sommer *et al.*, "Monitoring of Intercalation Stages in Lithium-Ion Cells over Charge-Discharge Cycles with Fiber Optic Sensors," *J. Electrochem. Soc.*, vol. 162, no. 14, pp. A2664–A2669, Jan. 2015.

[12] C.-J. Bae, A. Manandhar, P. Kiesel, and A. Raghavan, "Monitoring the Strain Evolution of Lithium-Ion Battery Electrodes using an Optical Fiber Bragg Grating Sensor," *Energy Technol.*, vol. 4, no. 7, pp. 851–855, Jul. 2016.

[13] A. Raghavan *et al.*, "Embedded Fiber-optic Sensing for Accurate Internal Monitoring of Cell State in Advanced Battery Management Systems Part 1: Cell Embedding Method and Performance," *J. Power Sources*, vol. 341, pp. 466–473, Feb. 2017.

[14] A. Ganguli *et al.*, "Embedded Fiber-optic Sensing for Accurate Internal Monitoring of Cell State in Advanced Battery Management Systems Part 2: Internal Cell Signals and Utility for State Estimation," *J. Power Sources*, vol. 341, pp. 474–482, Feb. 2017.
[15] A. Ghannoum, "Development of a Method to Characterize Optical Properties of Lithiated Graphite," presented at the 64th Canadian Chemical Engineering Conference, Niagara Falls, ON, Canada, 19-Oct-2014.
[16] L. Zdravkova, "Fiber Optic Sensor for In-Situ State-of-Charge Monitoring for Lithium-Ion Batteries," 2015.
[17] A. Ghannoum, K. Iyer, P. Nieva, and A. Khajepour, "Fiber Optic Monitoring of Lithium-Ion Batteries," in *IEEE SENSORS 2016 Proceedings*, Orlando, FL, USA, 2016, pp. 868–870.
[18] A. Ghannoum, P. Nieva, A. Yu, and A. Khajepour, "Development of Embedded Fiber-Optic Evanescent Wave Sensors for Optical Characterization of Graphite Anodes in Lithium-Ion Batteries," *ACS Appl. Mater. Interfaces*, vol. 9, no. 47, pp. 41284–41290, Nov. 2017.
[19] T. B. Reddy, *Linden's Handbook of Batteries*, 4th ed. The McGraw-Hill Companies, 2011.
[20] D. Aurbach, M. D. Levi, E. Levi, and A. Schechter, "Failure and Stabilization Mechanisms of Graphite Electrodes," *J. Phys. Chem. B*, vol. 101, no. 12, pp. 2195–2206, 1997.
[21] K. Xu, "Nonaqueous Liquid Electrolytes for Lithium-Based Rechargeable Batteries," *Chem. Rev.*, vol. 104, no. 10, pp. 4303–4418, Oct. 2004.
[22] T. Ohzuku, Y. Iwakoshi, and K. Sawai, "Formation of Lithium-Graphite Intercalation Compounds in Nonaqueous Electrolytes and Their Application as a Negative Electrode for a Lithium Ion (Shuttlecock) Cell," *J. Electrochem. Soc.*, vol. 140, no. 9, pp. 2490–2498, 1993.
[23] T. Zheng, J. N. Reimers, and J. R. Dahn, "Effect of turbostratic disorder in graphitic carbon hosts on the intercalation of lithium," *Phys. Rev. B*, vol. 51, no. 2, p. 734, 1995.
[24] S. J. Harris, A. Timmons, D. R. Baker, and C. Monroe, "Direct in situ measurements of Li transport in Li-ion battery negative electrodes," *Chem. Phys. Lett.*, vol. 485, no. 4–6, pp. 265–274, Jan. 2010.
[25] P. Maire, A. Evans, H. Kaiser, W. Scheifele, and P. Novák, "Colorimetric Determination of Lithium Content in Electrodes of Lithium-Ion Batteries," *J. Electrochem. Soc.*, vol. 155, no. 11, pp. A862–A865, 2008.
[26] W. Rudorff, "Crystal structure of acid compounds of graphite," *Z Phys Chem*, vol. B45, 1939.
[27] J. R. Dahn, "Phase diagram of LixC6," *Phys. Rev. B*, vol. 44, no. 17, pp. 9170–9177, Nov. 1991.
[28] M. Koltypin, Y. S. Cohen, B. Markovsky, Y. Cohen, and D. Aurbach, "The study of lithium insertion–deinsertion processes into composite graphite electrodes by in situ atomic force microscopy (AFM)," *Electrochem. Commun.*, vol. 4, no. 1, pp. 17–23, 2002.
[29] P. Bai, D. A. Cogswell, and M. Z. Bazant, "Suppression of phase separation in LiFePO4 nanoparticles during battery discharge," *Nano Lett.*, vol. 11, no. 11, pp. 4890–4896, 2011.
[30] R. Fong, U. von Sacken, and J. R. Dahn, "Studies of lithium intercalation into carbons using nonaqueous electrochemical cells," *J. Electrochem. Soc.*, vol. 137, no. 7, pp. 2009–2013, 1990.

[31] G. H. NAZRI and R. H. MULLER, “STABILITY OF NONAQUEOUS ELECTROLYTES FOR AMBIENT TEMPERATURE RECHARGEABLE LITHIUM CELLS,” *Chem. Eng. Commun.*, vol. 38, no. 3–6, pp. 383–391, Nov. 1985.
[32] K. Xu, “Nonaqueous Liquid Electrolytes for Lithium-Based Rechargeable Batteries,” *Chem. Rev.*, vol. 104, no. 10, pp. 4303–4418, Oct. 2004.
[33] H. Zhao *et al.*, “Propylene Carbonate (PC)-Based Electrolytes with High Coulombic Efficiency for Lithium-Ion Batteries,” *J. Electrochem. Soc.*, vol. 161, no. 1, pp. A194–A200, 2014.
[34] Y. Saito, M. Okano, K. Kubota, T. Sakai, J. Fujioka, and T. Kawakami, “Evaluation of Interactive Effects on the Ionic Conduction Properties of Polymer Gel Electrolytes,” *J. Phys. Chem. B*, vol. 116, no. 33, pp. 10089–10097, Aug. 2012.
[35] A. M. Andersson, A. Henningson, H. Siegbahn, U. Jansson, and K. Edström, “Electrochemically Lithiated Graphite Characterised by Photoelectron Spectroscopy,” *J. Power Sources*, vol. 119–121, pp. 522–527, Jun. 2003.
[36] P. Verma, P. Maire, and P. Novák, “A Review of the Features and Analyses of the Solid Electrolyte Interphase in Li-ion Batteries,” *Electrochim Acta*, vol. 55, no. 22, pp. 6332–6341, Sep. 2010.
[37] K. Edström, M. Herstedt, and D. P. Abraham, “A New Look at the Solid Electrolyte Interphase on Graphite Anodes in Li-Ion Batteries,” *J. Power Sources*, vol. 153, no. 2, pp. 380–384, Feb. 2006.
[38] H. Bryngelsson, M. Stjerndahl, T. Gustafsson, and K. Edström, “How Dynamic is the SEI?,” *J. Power Sources*, vol. 174, no. 2, pp. 970–975, Dec. 2007.
[39] S. Basu, C. Zeller, P. J. Flanders, C. D. Fuerst, W. D. Johnson, and J. E. Fischer, “Synthesis and properties of lithium-graphite intercalation compounds,” *Mater. Sci. Eng.*, vol. 38, no. 3, pp. 275–283, 1979.
[40] F. Wooten, *Optical properties of solids*. Academic Press, 1972.
[41] M. S. Dresselhaus and G. Dresselhaus, “Intercalation Compounds of Graphite,” *Adv. Phys.*, vol. 51, no. 1, pp. 1–186, 2002.
[42] I. P. Batra and L. Samuelson, “A Theoretical Study of the Electronic Properties of Intercalated Graphite,” *Synth. Met.*, vol. 1, no. 3, pp. 233–247, Apr. 1980.
[43] M. Zanini, S. Basu, and J. E. Fischer, “Alternate Synthesis and Reflectivity Spectrum of Stage 1 Lithium—Graphite Intercalation Compound,” *Carbon*, vol. 16, no. 3, pp. 211–212, 1978.
[44] L. Xie and J. Lu, “In Situ UV–Vis Diffuse Reflectance Studies on Lithium-Intercalated Carbons,” *J. Electroanal. Chem.*, vol. 497, no. 1, pp. 159–162, 2001.
[45] J. Newman and K. E. Thomas-Alyea, *Electrochemical Systems*. John Wiley & Sons, 2012.
[46] J. Newman and W. Tiedemann, “Porous-electrode theory with battery applications,” *AIChE J.*, vol. 21, no. 1, pp. 25–41, Jan. 1975.
[47] K. West, T. Jacobsen, and S. Atlung, “Modeling of Porous Insertion Electrodes with Liquid Electrolyte,” *J. Electrochem. Soc.*, vol. 129, no. 7, pp. 1480–1485, Jul. 1982.
[48] S. Atlung, “The kinetics of porous insertion electrodes,” *J. Power Sources*, vol. 26, no. 1–2, pp. 139–159, May 1989.

[49] D. R. Baker, “A transformation for the treatment of diffusion and migration. Application to stationary disk and hemisphere electrodes,” *J. Electroanal. Chem.*, vol. 314, no. 1–2, pp. 23–44, Sep. 1991.
[50] M. Doyle, T. F. Fuller, and J. Newman, “Modeling of Galvanostatic Charge and Discharge of the Lithium/Polymer/Insertion Cell,” *J. Electrochem. Soc.*, vol. 140, no. 6, pp. 1526–1533, Jun. 1993.
[51] T. F. Fuller, M. Doyle, and J. Newman, “Simulation and optimization of the dual lithium ion insertion cell,” *J. Electrochem. Soc.*, vol. 141, no. 1, pp. 1–10, 1994.
[52] M. Doyle, J. P. Meyers, and J. Newman, “Computer simulations of the impedance response of lithium rechargeable batteries,” *J. Electrochem. Soc.*, vol. 147, no. 1, pp. 99–110, 2000.
[53] M. Doyle, J. Newman, A. S. Gozdz, C. N. Schmutz, and J.-M. Tarascon, “Comparison of Modeling Predictions with Experimental Data from Plastic Lithium Ion Cells,” *J. Electrochem. Soc.*, vol. 143, no. 6, pp. 1890–1903, Jun. 1996.
[54] L. Cai and R. E. White, “Mathematical modeling of a lithium ion battery with thermal effects in COMSOL Inc. Multiphysics (MP) software,” *J. Power Sources*, vol. 196, no. 14, pp. 5985–5989, Jul. 2011.
[55] A. Burke and M. Miller, “Performance Characteristics of Lithium-ion Batteries of Various Chemistries for Plug-in Hybrid Vehicles,” *Inst. Transp. Stud.*, Jun. 2009.
[56] M. Takahashi, S. Tobishima, K. Takei, and Y. Sakurai, “Reaction Behavior of LiFePO4 as a Cathode Material for Rechargeable Lithium Batteries,” *Solid State Ion.*, vol. 148, no. 3–4, pp. 283–289, 2002.
[57] L. Y. Wang, M. P. Polis, G. G. Yin, W. Chen, Y. Fu, and C. C. Mi, “Battery Cell Identification and SOC Estimation Using String Terminal Voltage Measurements,” *IEEE Trans. Veh. Technol.*, vol. 61, no. 7, pp. 2925–2935, Sep. 2012.
[58] T. A. Stuart and W. Zhu, “Modularized Battery Management for Large Lithium Ion Cells,” *J. Power Sources*, vol. 196, no. 1, pp. 458–464, Jan. 2011.
[59] R. Xiong, H. He, F. Sun, X. Liu, and Z. Liu, “Model-Based State of Charge and Peak Power Capability Joint Estimation of Lithium-Ion Battery in Plug-In Hybrid Electric Vehicles,” *J. Power Sources*, vol. 229, pp. 159–169, May 2013.
[60] Y. Ein-Eli, B. Markovsky, D. Aurbach, Y. Carmeli, H. Yamin, and S. Luski, “The Dependence of The Performance of Li-C Intercalation Anodes for Li-ion Secondary Batteries on The Electrolyte Solution Composition,” *Electrochim Acta*, vol. 39, no. 17, pp. 2559–2569, 1994.
[61] R. L. Sacci *et al.*, “Structure of Spontaneously Formed Solid-Electrolyte Interphase on Lithiated Graphite Determined Using Small-Angle Neutron Scattering,” *J. Phys. Chem. C*, vol. 119, no. 18, pp. 9816–9823, May 2015.
[62] R. Norris *et al.*, “Multi-band Reflectance Spectroscopy of Carbonaceous Lithium Iron Phosphate Battery Electrodes versus State of Charge,” 2014, vol. 8982, pp. 898214-1–8.
[63] V. Ruddy, B. D. MacCraith, and J. A. Murphy, “Evanescent Wave Absorption Spectroscopy Using Multimode Fibers,” *J. Appl. Phys.*, vol. 67, no. 10, pp. 6070–6074, 1990.

[64] P. Pfluger *et al.*, "Concentration Dependence of Optical Reflectivity and 2γ-Angular Correlation Distribution of Positron Annihilation in Donor- and Acceptor-Intercalated Graphite," *Synth. Met.*, vol. 2, pp. 285–293, 1980.
[65] J. E. Fischer, J. M. Bloch, C. C. Shieh, M. E. Preil, and K. Jelley, "Reflectivity Spectra and Dielectric Function of Stage-1 Donor Intercalation Compounds of Graphite," *Phys. Rev. B*, vol. 31, no. 8, pp. 4773–4783, Apr. 1985.
[66] P. Pfluger, V. Geiser, S. Stolz, and H.-J. Güntherodt, "Aspects of Alkali Metal Interclation and Deintercalation in Highly Oriented Pyrolytic Graphites," *Synth. Met.*, vol. 3, pp. 27–39, 1981.
[67] P. Arora, R. E. White, and M. Doyle, "Capacity Fade Mechanisms and Side Reactions in Lithium-Ion Batteries," *J. Electrochem. Soc.*, vol. 145, no. 10, pp. 3647–3667, Oct. 1998.
[68] D. Aurbach, E. Zinigrad, Y. Cohen, and H. Teller, "A short review of failure mechanisms of lithium metal and lithiated graphite anodes in liquid electrolyte solutions," *Solid State Ion.*, vol. 148, no. 3, pp. 405–416, 2002.
[69] Y. Qi and S. J. Harris, "In Situ Observation of Strains during Lithiation of a Graphite Electrode," *J. Electrochem. Soc.*, vol. 157, no. 6, pp. A741–A747, Jun. 2010.
[70] C. Unger and W. Stocklein, "Investigation of the microbending sensitivity of fibers," *Light. Technol. J. Of*, vol. 12, no. 4, pp. 591–596, 1994.
[71] J. B. Goodenough and Y. Kim, "Challenges for Rechargeable Li Batteries †," *Chem. Mater.*, vol. 22, no. 3, pp. 587–603, Feb. 2010.
[72] J. S. Gnanaraj, Y. S. Cohen, M. D. Levi, and D. Aurbach, "The Effect of Pressure on the Electroanalytical Response of Graphite Anodes and LiCoO 2 Cathodes for Li-ion Batteries," *J. Electroanal. Chem.*, vol. 516, no. 1, pp. 89–102, 2001.
[73] J. Cannarella and C. B. Arnold, "Stress Evolution and Capacity Fade in Constrained Lithium-Ion Pouch Cells," *J. Power Sources*, vol. 245, pp. 745–751, Jan. 2014.
[74] H. Buqa, D. Goers, M. Holzapfel, M. E. Spahr, and P. Novák, "High Rate Capability of Graphite Negative Electrodes for Lithium-Ion Batteries," *J. Electrochem. Soc.*, vol. 152, no. 2, pp. A474–A481, Feb. 2005.
[75] P. Polynkin, A. Polynkin, N. Peyghambarian, and M. Mansuripur, "Evanescent Field-based Optical Fiber Sensing Device for Measuring The Refractive Index of Liquids in Microfluidic Channels," *Opt. Lett.*, vol. 30, no. 11, pp. 1273–1275, Jun. 2005.
[76] P. Nath, "Enhanced Sensitive Fiber-optic Sensor with Double Pass Evanescent Field Absorption," *Microw. Opt. Technol. Lett.*, vol. 51, no. 12, pp. 3004–3006, Dec. 2009.
[77] P. K. Choudhury, "On The pH Response of Fiber Optic Evanescent Field Absorption Sensor Having a U-shaped Probe: An Experimental Analysis," *Opt. - Int. J. Light Electron Opt.*, vol. 114, no. 1, pp. 13–18, 2003.
[78] P. K. Choudhury, "On The Fiber-optic Chlorine Sensor with Enhanced Sensitivity Based on The Study of Evanescent Field Absorption Spectroscopy," *Opt. - Int. J. Light Electron Opt.*, vol. 115, no. 7, pp. 329–333, 2004.
[79] E. Margalit, H. Dodiuk, E. M. Kosower, and A. Katzir, "Infrared Fiber Evanescent Wave Spectroscopy For In-Situ Monitoring Of Chemical Processes," presented at the Infrared Fiber Optics, Los Angeles, CA, United States, 1989, vol. 1048, pp. 145–153.

[80] A. Messica, A. Greenstein, and A. Katzir, "Theory of Fiber-optic, Evanescent-wave Spectroscopy and Sensors," *Appl. Opt.*, vol. 35, no. 13, pp. 2274–2284, 1996.
[81] C. Peabody and C. B. Arnold, "The Role of Mechanically Induced Separator Creep in Lithium-ion Battery Capacity Fade," *J. Power Sources*, vol. 196, no. 19, pp. 8147–8153, Oct. 2011.
[82] M. Lu, H. Cheng, and Y. Yang, "A Comparison of Solid Electrolyte Interphase (SEI) on The Artificial Graphite Anode of The Aged and Cycled Commercial Lithium Ion Cells," *Electrochimica Acta*, vol. 53, no. 9, pp. 3539–3546, Mar. 2008.
[83] E. R. Lyons and H. P. Lee, "Demonstration of an Etched Cladding Fiber Bragg Grating Filter with Reduced Tuning Force Requirement," *IEEE Photonics Technol. Lett.*, vol. 11, no. 12, pp. 1626–1628, Dec. 1999.
[84] G. a. C. M. Spierings, "Wet Chemical Etching of Silicate Glasses in Hydrofluoric Acid Based Solutions," *J. Mater. Sci.*, vol. 28, no. 23, pp. 6261–6273, Dec. 1993.
[85] H. Proksche, G. Nagorsen, and D. Ross, "The Influence of NH 4 F on the Etch Rates of Undoped SiO2 in Buffered Oxide Etch," *J. Electrochem. Soc.*, vol. 139, no. 2, pp. 521–524, Feb. 1992.
[86] B. S. Kawasaki, K. O. Hill, D. C. Johnson, and Y. Fujii, "Narrow-band Bragg Reflectors in Optical Fibers," *Opt. Lett.*, vol. 3, no. 2, pp. 66–68, Aug. 1978.
[87] J. Rheims, J. Köser, and T. Wriedt, "Refractive-index Measurements in The Near-IR Using an Abbe Refractometer," *Meas. Sci. Technol.*, vol. 8, no. 6, pp. 601–605, 1997.
[88] I. H. Malitson, "Interspecimen Comparison of the Refractive Index of Fused Silica*,†," *J. Opt. Soc. Am.*, vol. 55, no. 10, pp. 1205–1209, Oct. 1965.
[89] J. P. Golden, G. P. Anderson, S. Y. Rabbany, and F. S. Ligler, "An Evanescent Wave Biosensor. II. Fluorescent Signal Acquisition From Tapered Fiber Optic Probes," *Biomed. Eng. IEEE Trans. On*, vol. 41, no. 6, pp. 585–591, Jun. 1994.
[90] E. Prada, D. Di Domenico, Y. Creff, J. Bernard, V. Sauvant-Moynot, and F. Huet, "Simplified electrochemical and thermal model of LiFePO4-graphite Li-ion batteries for fast charge applications," *J. Electrochem. Soc.*, vol. 159, no. 9, pp. A1508–A1519, 2012.
[91] M. Safari and C. Delacourt, "Modeling of a Commercial Graphite/LiFePO4 Cell," *J. Electrochem. Soc.*, vol. 158, no. 5, pp. A562–A571, May 2011.
[92] M. Doyle and Y. Fuentes, "Computer Simulations of a Lithium-Ion Polymer Battery and Implications for Higher Capacity Next-Generation Battery Designs," *J. Electrochem. Soc.*, vol. 150, no. 6, pp. A706–A713, Jun. 2003.
[93] S. Yu, S. Kim, T. Y. Kim, J. H. Nam, and W. I. Cho, "Model Prediction and Experiments for the Electrode Design Optimization of LiFePO $_4$ /Graphite Electrodes in High Capacity Lithium-ion Batteries," *Bull. Korean Chem. Soc.*, vol. 34, no. 1, pp. 79–88, Jan. 2013.
[94] S.-I. Lee, U.-H. Jung, Y.-S. Kim, M.-H. Kim, D.-J. Ahn, and H.-S. Chun, "A study of electrochemical kinetics of lithium ion in organic electrolytes," *Korean J. Chem. Eng.*, vol. 19, no. 4, pp. 638–644, 2002.
[95] C. Daniel and J. O. Besenhard, *Handbook of Battery Materials*. John Wiley & Sons, 2012.
[96] T. Nakajima and H. Groult, *Fluorinated Materials for Energy Conversion*. Elsevier, 2005.

[97] E. A. Taft and H. R. Philipp, “Optical Properties of Graphite,” *Phys. Rev.*, vol. 138, no. 1A, pp. A197–A202, Apr. 1965.
[98] L. A. Grunes *et al.*, “Valence and core electronic excitations in Li C 6,” *Phys. Rev. B*, vol. 28, no. 12, p. 6681, 1983.
[99] F. Wooten, *Optical properties of solids*. Academic Press, 1972.
[100] L. G. Johnson and G. Dresselhaus, “Optical Properies of Graphite,” *Phys. Rev. B*, vol. 7, no. 6, pp. 2275–2285, 1973.
[101] J. R. Godin, “Development of an Analytical Model for a Fiber Optic Evanescent Wave Sensor,” 2015.
[102] M. Ahmad and L. L. Hench, “Effect of taper geometries and launch angle on evanescent wave penetration depth in optical fibers,” *Biosens. Bioelectron.*, vol. 20, no. 7, pp. 1312–1319, Jan. 2005.
[103] J. B. Siegel, X. Lin, A. G. Stefanopoulou, and D. Gorsich, “Neutron imaging of lithium concentration for validation of li-ion battery state of charge estimation,” DTIC Document, 2010.
[104] J. B. Siegel, A. G. Stefanopoulou, P. Hagans, Y. Ding, and D. Gorsich, “Expansion of Lithium Ion Pouch Cell Batteries: Observations from Neutron Imaging,” *J. Electrochem. Soc.*, vol. 160, no. 8, pp. A1031–A1038, 2013.